

# POLITECNICO DI TORINO

Corso di Laurea Magistrale in Ingegneria Biomedica



Tesi di Laurea Magistrale

Definition of new hemodynamic descriptors based on wall  
shear stress divergence in carotid bifurcations

Relatori:

Prof. Umberto Morbiducci

Ing. Diego Gallo

Dott. Valentina Mazzi

Candidato:

Serena Esposito

A.A. 2017/2018



# Index

Abstract .....	6
Chapter 1. Cardiovascular system .....	8
1.1 Blood vessels .....	9
1.2 Structure of blood vessels walls.....	9
1.3 Vascular diseases .....	11
1.3.1 Arteriosclerosis .....	11
1.3.2 Monckeberg medial calcific sclerosis.....	11
1.3.3 Atherosclerosis.....	11
Chapter 2. Hemodynamics .....	13
2.1 Rheologic properties of blood .....	13
2.2 Reynolds number .....	16
2.3 Navier Stokes equations .....	17
2.4 Poiseuille's law.....	17
2.5 Wall Shear Stress .....	19
2.6 Hemodynamics role in atherosclerosis.....	20
2.7 Carotid bifurcation .....	22
Chapter 3. Hemodynamic wall descriptors .....	25
3.1 TAWSS: Time Averaged Wall Shear Stress.....	25
3.2 OSI: Oscillatory Shear Index.....	25
3.3 RRT: Relative Residence Time .....	26
3.4 transWSS: transverse Wall Shear Stress.....	26
3.5 CFI: Cross Flow Index .....	27
3.6 WSSax: Axial Wall Shear Stress .....	28
3.7 WSSG: Wall Shear Stress Spatial Gradient.....	28
3.8 WSSAG: Wall Shear Stress Angle Gradient .....	29
3.9 WSST: Wall Shear Stress Temporal gradient .....	29
3.10 DH: Dominant Harmonic.....	30
3.11 HI: Harmonic Index .....	30
Chapter 4. Methods.....	32
4.1 Computational fluid dynamics modelling.....	32
4.2 Wall shear stress divergence .....	32

4.3 Wall shear stress divergence computation .....	34
4.4 Normalized WSS vector field divergence.....	37
4.5 WSS divergence-based parameters .....	38
4.6 Co-localization analysis .....	40
4.7 Sensitivity analysis .....	43
Chapter 5. Results.....	46
Chapter 6. Conclusions .....	68
Appendix.....	71
A) Generation of the centerline and cut of bifurcation regions in VMTK software .....	71
B) Projection of the HWPs onto the bifurcation regions in VMTK software .....	71
C) Sensitivity Analysis.....	71
References .....	77
Figure references.....	79

## List of Figures and Tables

Figure 1. Circulatory system: Pulmonary and systemic circuits .....	8
Figure 2. Blood vessels: arteries, capillaries and veins .....	9
Figure 3. Structure of blood vessels walls .....	10
Figure 4. Atherosclerosis: A) Normal artery with a normal blood flow B) Narrowed artery with abnormal blood flow .....	12
Figure 5. Carotid artery disease.....	12
Figure 6. Fluid flowing between two parallel plates .....	13
Figure 7: Shear stress-shear rate relationship for Newtonian fluid and blood.....	14
Figure 8. Dependence of the human blood viscosity on haematocrit, for indicated shear rates.....	15
Figure 9. Dependence of the viscosity on the shear rate for three different red blood cells suspensions .....	15
Figure 10. Poiseuille flow: parabolic velocity profile.....	18
Figure 11. Development of boundary layer in fluid entering a pipe .....	19
Figure 12. Carotid arteries.....	22
Figure 13. Carotid bifurcation.....	23
Figure 14. Blood velocity pattern in a carotid bifurcation .....	24
Figure 15. Flow phenomena occurring in a human carotid bifurcation.....	24
Figure 16. Physical interpretation of the divergence of a vector field $v$ : A) Sink B) Source C) Point with zero divergence.....	33
Figure 17. Triangle of the mesh and linear basis function differentiation.....	35
Figure 18. Generic triangle of the mesh with auxiliary vectors for the computation of WSS gradient.....	36
Figure 19. Example of computation of $\text{divWSS}$ in a node of the mesh.....	37
Figure 20. WSS field configurations: A) and B) positive divergence C) and D) negative divergence .....	37
Figure 21. Probability density estimates of $\text{divWSS}$ values taken during the cardiac cycle in the nodes of one of the carotid bifurcation models. ....	39
Figure 22. Probability density estimates of the spatial averages of $\text{divWSS}$ values taken during the cardiac cycle for all the 46 carotid bifurcation models .....	40
Figure 23. Example of generation of the centerline of a vessel in VMTK .....	41
Figure 24. Example of cut of a bifurcation region along the sections CCA3, ICA5 and ECA2 ..	41
Table 1. Maximum and minimum dimensions of the elements of the grids realized in sensitivity analysis .....	43
Figure 25. CCA section in the 4 million elements mesh (left) and in the 8 million elements mesh (right). ....	44
Figure 26. Exposure to low TAWSS for the 46 carotid bifurcation models.....	46
Figure 27. Exposure to high OSI for the 46 carotid bifurcation models.....	47
Figure 28. Exposure to high RRT for the 46 carotid bifurcation models.....	48
Figure 29. Exposure to high TransWSS for the 46 carotid bifurcation models .....	49
Figure 30. Exposure to negative $\text{WSSax}$ for the 46 carotid bifurcation models. ....	50
Figure 31. Exposure to high CFI for the 46 carotid bifurcation models. ....	51

Figure 32. Exposure to high WSST values for the 46 carotid bifurcation models.....	52
Figure 33. Exposure to low DivN for the 46 carotid bifurcation models.....	53
Figure 34. Exposure to high DivP for the 46 carotid bifurcation models.....	54
Figure 35. Exposure to high ODI for the 46 carotid bifurcation models.....	55
Figure 36. Exposure to high Counter values for the 46 carotid bifurcation models.....	56
Figure 37. Distribution of SI values for the SA exposed to low DivN with the SA exposed to disturbed flow, as defined by the existing HWPs.....	57
Figure 38. Distribution of SI values for the SA exposed to high DivP with the SA exposed to disturbed flow, as defined by the existing HWPs.....	59
Figure 39. Distribution of SI values for the SA exposed to high ODI with the SA exposed to disturbed flow, as defined by the existing HWPs.....	60
Figure 40. Distribution of SI values for the SA exposed to high ODI with the SA exposed to low DivN (left) and with the SA exposed to high DivP (right). ....	61
Figure 41. Distribution of SI values for the SA exposed to high Counter values with the SA exposed to high ODI. ....	61
Figure 42. Distribution of SI values for the SA exposed to high Counter values with the SA exposed to disturbed flow, as defined by the existing HWPs.....	62
Figure 43. Exposure to high CounterSys values for the 46 carotid bifurcation models.....	63
Figure 44. Exposure to high CounterDia values for the 46 carotid bifurcation models.....	64
Figure 45. Distribution of SI values for the SA exposed to high CounterSys values with the SA exposed to high CounterDia values.....	65
Figure 46. Distribution of SI values for the SA exposed to high CounterSys values with the SA exposed to disturbed flow, as defined by the existing HWPs.....	66
Figure 47. Distribution of SI values for the SA exposed to high CounterDia values with the SA exposed to disturbed flow, as defined by the existing HWPs.....	67

## Abstract

Cardiovascular diseases are a major cause of health problems and death in developed countries. Atherosclerosis is the most predominant form of vascular disease and consists in lipid accumulation in the wall of large- and medium-sized arteries. It is associated with systemic risk factors, but disturbed haemodynamics and complex vessel geometry play a localizing role in atherosclerotic plaque formation. The prevailing theory recognizes low and oscillatory wall shear stress (WSS) acting on the endothelial layer as indices of disturbed flow that promote atherosclerosis progression. Contradictory findings and an unsatisfying co-localization of low/oscillatory WSS with atherosclerotic lesions however encouraged the investigation of different WSS features that correlate with disease initiation and progression. So, temporal multidirectionality of WSS has recently been proposed as a pro-atherogenic factor.

Aim of this thesis was to introduce new hemodynamic wall parameters (HWPs) able to distinguish among tensile, compressive and uniform shear stresses acting on the endothelial cells. The direction of WSS could influence the morphology and the biology of endothelial cells, increasing the permeability to atherogenic particles under the endothelium and altering the balance between pro- and anti-atherosclerotic signals. However, none of the existing HWPs can capture the spatial directionality of WSS.

For this purpose, HWPs based on WSS divergence were proposed: Positive WSS Divergence (DivP), Negative WSS Divergence (DivN) and Oscillatory WSS Divergence Index (ODI). The divergence of WSS can measure the tendency of WSS vector field to converge toward or diverge from a point. More in detail, a positive divergence identifies a source-arranged field, that results in an expansion of the vessel wall, whereas a negative divergence highlights a WSS field with a sink configuration, that causes a compression of the endothelium. So, the proposed divergence-based descriptors allow an evaluation of WSS vector field direction throughout the cardiac cycle. ODI was defined as an index that quantifies the oscillations of WSS direction between the source and sink configurations.

The divergence of WSS vector field takes into account both the magnitude and the direction of WSS. So, to evaluate the WSS directionality only, neglecting the variations in WSS magnitude, it was considered the divergence of the normalized WSS. It was computed as the sum of the spatial derivatives of the normalized WSS components in each triangle of the surface meshes.

The divergence-based HWPs were computed on the luminal surfaces of forty-six models of right carotid bifurcations acquired from healthy people. Then, a co-localization analysis of the divergence-based descriptors with the established HWPs was carried out through a visual examination of the critical surface areas and a systematic quantification, by means of similarity indices, of the spatial overlapping of surface areas exposed to disturbed flow, as defined by each HWP.

Surface areas mainly exposed to negative divergence resulted to be more concentrated around the bifurcation expansion. DivN pointed out regions characterized by sink-arranged WSS field, it moderately co-localized with HWPs that indicate blood stagnation, high near-wall residence time of particles and uniaxial oscillatory WSS. Regions predominantly exposed to positive divergence were mainly located at the bifurcation apex. DivP pointed out multidirectional source-arranged WSS vector field. ODI co-localized with HWPs that identify surface areas exposed to uniaxial highly oscillating WSS, flow reversal regions, high residence time regions and recirculation zones.

The potential correlation between the directional changes of WSS that the proposed divergence-based HWPs can identify and atherosclerotic lesion appearance needs to be checked.

## Chapter 1. Cardiovascular system

Cardiovascular system is a closed loop system, composed by two distinct circuits: the systemic and the pulmonary circuits. The circulatory system consists of heart, blood and a network of blood vessels (arteries, veins and capillaries). It delivers oxygen, nutrients and other substances to body tissues and carries waste products derived from cellular metabolism to the organs responsible for their elimination.

The blood is a suspension of cellular components in an aqueous solution. The suspending medium is called plasma, the suspended particles include red blood cells, white blood cells and platelets. The heart is the pump that propels the blood into the vessels. It is a muscular organ, whose contraction generates the pressure that is necessary to eject blood into the major vessels, from which blood is distributed to the body. The heart contains four chambers, two atria (the upper ones) and two ventricles (the lower ones). The left side chambers supply the systemic circulation, whereas the right side chambers supply the pulmonary circulation. The atrium and the ventricle of each side are separated by a valve, whose opening and closure are regulated by the pressure gradient to ensure the unidirectionality of blood flow, and to avoid blood regurgitation.

Systemic arteries provide oxygen-rich blood from the left ventricle of the heart to body tissues. The blood returned to the heart through systemic veins has less oxygen, since much of the oxygen carried by the blood has been delivered to the cells. So, arteries in the pulmonary circuit carry blood low in oxygen to the lungs for gas exchange. Then, pulmonary veins return freshly oxygenated blood from the lungs to the heart to be pumped into systemic circulation (Figure 1).

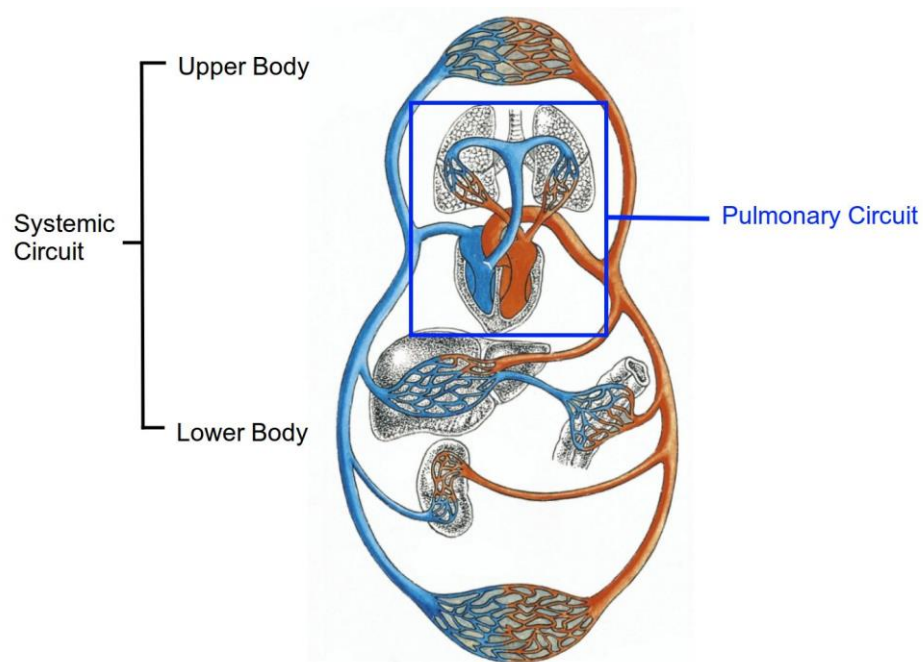


Figure 1. Circulatory system: Pulmonary and systemic circuits

## 1.1 Blood vessels

Blood circulates through the whole body via blood vessels. The vessels that carry blood away from the heart to peripheral organs are called arteries. They branch into smaller vessels known as arterioles, that further branch into tiny capillaries, where gas, ions, nutrients and wastes are exchanged between blood and body tissues. Blood drains from the capillaries into venules, small blood vessels that then unite to form veins, larger blood vessels that transport the blood back to the heart (Figure 2).

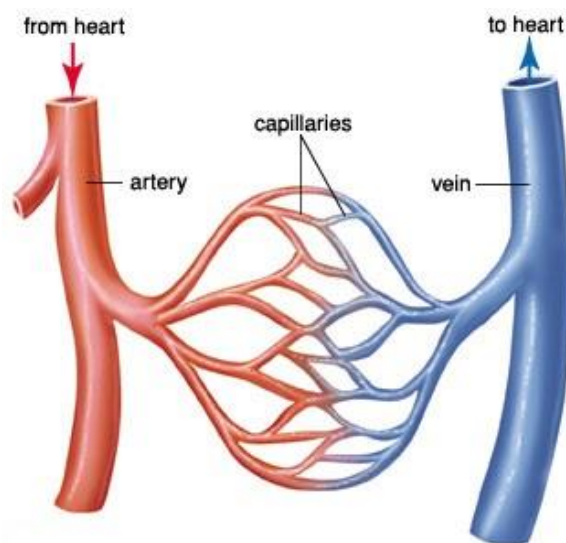


Figure 2. Blood vessels: arteries, capillaries and veins

Arteries and veins differ structurally and functionally. Arteries transport blood under high pressure, which is exerted by the pumping action of the heart. So, arteries possess thick, strong, elastic walls to ensure fast and efficient blood flow to body tissues, whereas veins withstand a much lower pressure, so they have thinner walls and larger lumens, i.e. the passageways through which the blood flows, allowing more blood to flow with less vessel resistance. In addition, many veins of the body contain valves that assist the unidirectional flow toward the heart, preventing the backflow of blood.

## 1.2 Structure of blood vessels walls

Both arteries and veins walls consist of three tissue layers (Figure 3), called tunics:

- Tunica intima: the innermost and thinnest layer composed of epithelial and connective tissue layers. The inner surface of the tunica intima is a thin layer called endothelium, that isolates the blood circulating into the lumen and his components from the underlying thrombogenic tissues. Damage to this

endothelial continuous lining and exposure of blood to the collagenous fibers beneath is one of the primary causes of clot formation. Next to the endothelium is the basal lamina, a subendothelial permeable layer containing type IV collagen with a structural function. In larger arteries, an internal elastic lamina also exists. It is a layer of longitudinally arranged elastic fibers permeated with small openings and it delimits the tunica intima from the

- Tunica media: a layer of alternated smooth muscle cells and elastic fibers arranged in circular sheets. In large and medium sized arteries, this is the thickest layer and it contains a large amount of elastin. Smooth muscle cells control the calibre of the vessel maintaining blood pressure and proper circulation. Contraction of the circular muscles decreases the vessel lumen, reducing blood flow and increasing blood pressure, whereas their vasodilation increases blood flow as the smooth muscle relaxes, allowing the lumen to widen and blood pressure to drop. Therefore, the tunica media is responsible for the pulsatility of blood flow. A second layer of fenestrated elastic fibers, called the external elastic lamina, separates the tunica media from the
- Tunica adventitia: the outermost layer, that consists mainly of connective tissue fibers that protect and reinforce the vessel. This is normally the thickest tunic in veins. In large vessels, it contains vasa vasorum, i.e. capillaries that supply nutrients to the vessel wall.

The layered structure of vessel walls gives rise to anisotropic mechanical properties, with different elastic moduli in the axial and circumferential directions.

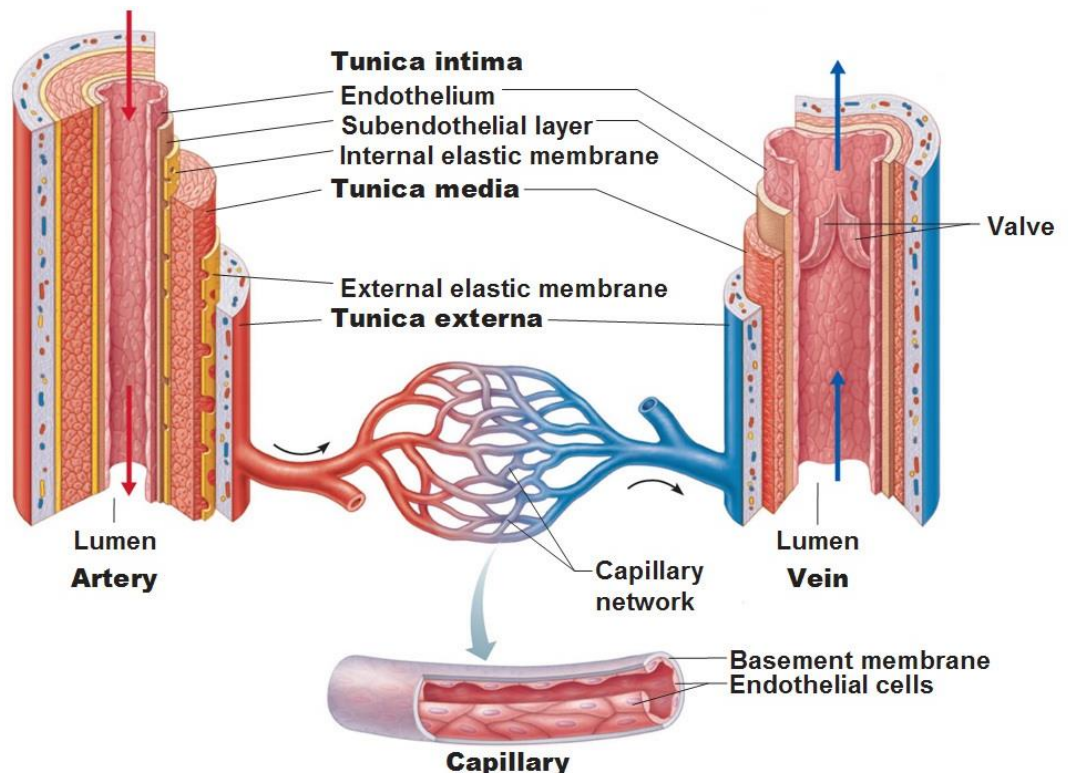


Figure 3. Structure of blood vessels walls

## 1.3 Vascular diseases

Cardiovascular diseases are a major cause of health problems and death in developed countries. In the more technologically developed countries of the world, such as the United States, the United Kingdom, and most other European countries, the most predominant form of cardiovascular disease is arteriosclerotic disease. There are three recognized types of arteriosclerosis: arteriolosclerosis, Monckeberg medial calcific sclerosis and atherosclerosis.

### 1.3.1 Arteriosclerosis

Arteriolosclerosis affects small arteries and arterioles. It is a chronic disease that involves an abnormal thickening and hardening of the vessel walls, with a resulting narrowing of the lumen and loss of elasticity.

### 1.3.2 Monckeberg medial calcific sclerosis

Monckeberg medial calcific sclerosis is a disease characterized by deposits of calcium in the tunica media of muscular arteries in people over age 50. These calcifications do not decrease the size of the arterial lumen.

### 1.3.3 Atherosclerosis

Atherosclerosis is a slow and progressive chronic, inflammatory, fibroproliferative vascular disease of large- and medium-sized arteries [Chatzizisis *et al.* 2007]. It consists in lipid accumulation in the artery wall, between the tunica media and the tunica intima, so that plaque builds up inside the arterial lumen (Figure 4, Panel B). Plaques are made up of fat, cholesterol, calcium and fibrin. Over time, these deposits in arteries cause the thickening of the vessels walls, and so their weakening and loss of flexibility. This narrows the opening [3], reducing or even totally blocking the blood flow and the supply of oxygen to cells and organs. Atherosclerosis typically does not produce symptoms until the luminal diameter of the vessel has been decreased by 70 to 80 percent.

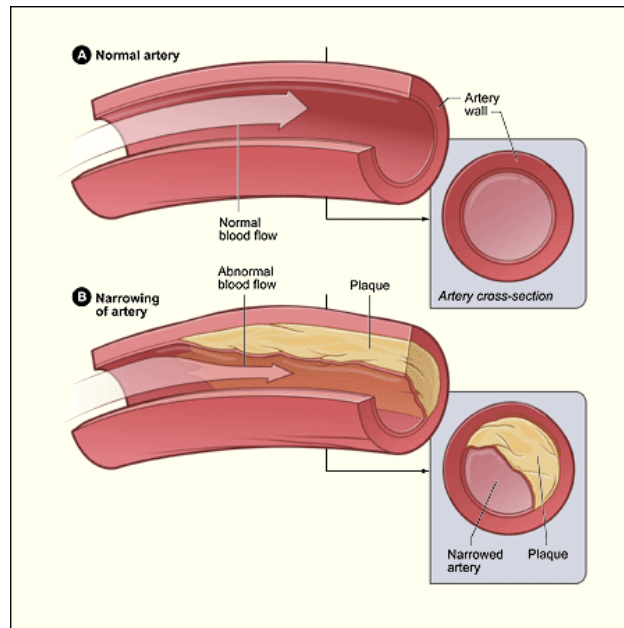


Figure 4. Atherosclerosis: A) Normal artery with a normal blood flow B) Narrowed artery with abnormal blood flow

Consequently, atherosclerosis can lead to serious diseases [3]:

- coronary heart disease, if the coronary arteries that supply oxygen-rich blood to the heart are blocked. In this case a heart attack or an angina can occur;
- carotid artery disease, when the plaque builds-up in the carotid arteries, that provide blood to the brain (Figure 5). So, a stroke can occur, and brain cells deprived of oxygen begin to die;
- peripheral artery disease, if an artery delivering oxygen to the extremities (legs, arms and pelvis) is blocked. This can result in gangrene;
- chronic kidney disease, if the plaque builds-up in the renal arteries causing a loss of kidney function.

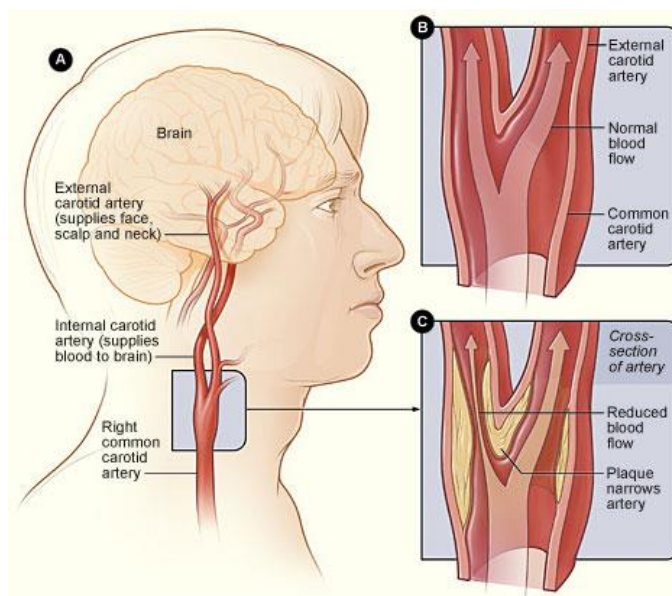


Figure 5. Carotid artery disease

## Chapter 2. Hemodynamics

Hemodynamics is the physical study of flowing blood and of all the solid structures through which it flows. It deals with the distribution of pressures and flows in the circulatory system. The heart pressurizes the blood, providing energy that drives it through the vascular network. Blood vessels may participate in the distribution of blood by active contraction or dilation [Secomb, 2017].

### 2.1 Rheologic properties of blood

The blood is subject to mechanical forces resulting from blood flow and blood pressure, that may be described using the concept of stress, i.e. the force per unit area acting on a surface within or on the boundary of the material. The stress is a second order tensor that allows the representation of the traction forces acting on the chosen surface. In the Euclidian space, the stress tensor has nine components  $\sigma_{ij}$ , where the subscripts can take the values 1, 2 or 3. Each component represents the force in the  $i$ -th coordinate direction acting on a surface whose normal vector is the  $j$ -th coordinate direction. So, stress tensor consists of three normal components and six tangential ones. If  $i=j$ , the component is defined normal stress, because it acts perpendicular to the surface, whereas if  $i \neq j$  the stress is referred to as a shear stress, that acts parallel to the surface.

Considering a fluid flowing between two parallel plates (Figure 6) placed at a distance  $h$ , with one plate (at  $y=0$ ) at rest and the other one (at  $y=h$ ) moving parallel to itself in the  $x$  direction with constant velocity  $v_x$ , according to the no-slip condition, the fluid adjacent to a surface moves at the same velocity as the solid surface does. This leads to the establishment of velocity gradient. Thus, as the fluid particles travel parallel to the wall, their velocity increases from zero to a maximum value at  $y=h$ . The velocity gradient (shear rate) is given by Eq. 1:

$$\dot{\gamma} = \frac{dv_x}{dy} \quad \text{Eq. 1}$$

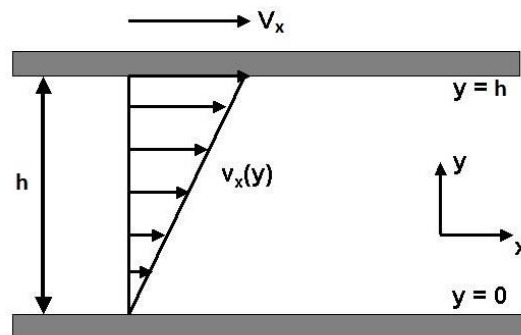


Figure 6. Fluid flowing between two parallel plates

Shear rate is defined as the rate at which adjacent layers of fluid move with respect to each other [Papaioannou and Stefanadis, 2005].

To resist the deformation of fluid resulting from the velocity gradient, a shear stress  $\tau_{xy}$  is generated in the fluid, owing to the dissipation of energy caused by the sliding of fluid molecules. The resistance of the fluid to deformation is described by a constant known as viscosity  $\mu$ , defined as the ratio of the shear stress to velocity gradient. So, the shear stress is:

$$\tau_{yx} = -\mu\dot{\gamma} = -\mu\frac{dv_x}{dy} \quad \text{Eq. 2}$$

This relation is valid only for Newtonian fluids (Figure 7), whose viscosity is an intrinsic property at a given temperature and pressure, independent of shear rate. The minus sign is needed because  $\tau$  is defined in the negative direction. On the other hand, the blood shows non-Newtonian properties, it is governed by a non-linear relationship between shear stress and shear rate (Figure 7).

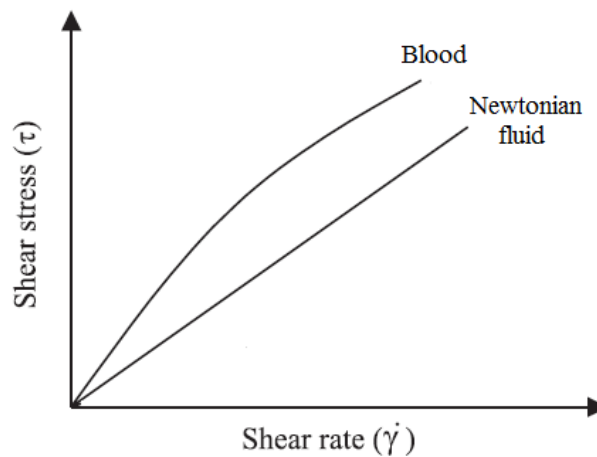


Figure 7: Shear stress-shear rate relationship for Newtonian fluid and blood

Blood viscosity depends on pressure, temperature and shear rate. At very low shear rates, blood viscosity increases (Figure 8). This phenomenon is known as shear-thinning and results almost entirely from red blood cells behaviour in suspension. In fact, under low-flow conditions, the erythrocytes can adhere to each other, leading to the formation of stacks of cells known as rouleaux, that create more interference with the flow. So, the aggregation contributes to the non-Newtonian behaviour of blood. High values of haematocrit i.e. the volume fraction of red blood cells, whose value in an adult is usually assumed to be equal to 45%, can promote red blood cells adhesion.

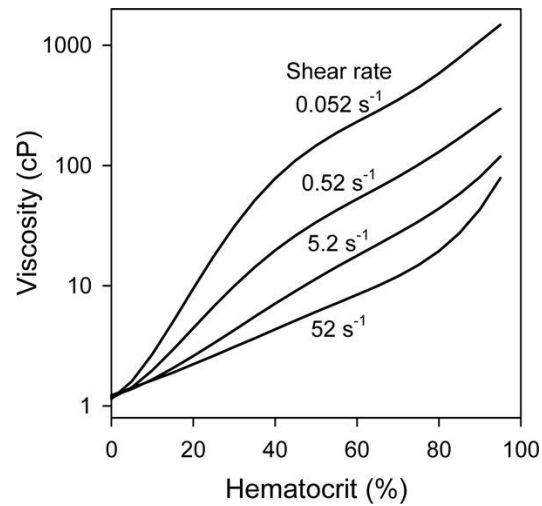


Figure 8. Dependence of the human blood viscosity on haematocrit, for indicated shear rates

This strong increase in viscosity due to the aggregation of red blood cells can be observed comparing normal blood with red blood cells in a Ringer solution, that has the same viscosity as plasma, but does not contain fibrinogen, which is responsible for the aggregation in rouleaux (Figure 9). Another phenomenon could be observed if erythrocytes are hardened. In this case, the viscosity results independent of shear rate and higher than the viscosity of normal red blood cells in the same medium (Figure 9). This result shows that at high shear rates the deformability of red blood cells is responsible for the reduction in blood viscosity. In fact, in this flow condition, the erythrocytes assume an ellipsoidal shape with the principal axis aligned with the direction of flow, and so they offer less resistance to the flow [Secomb, 2017].

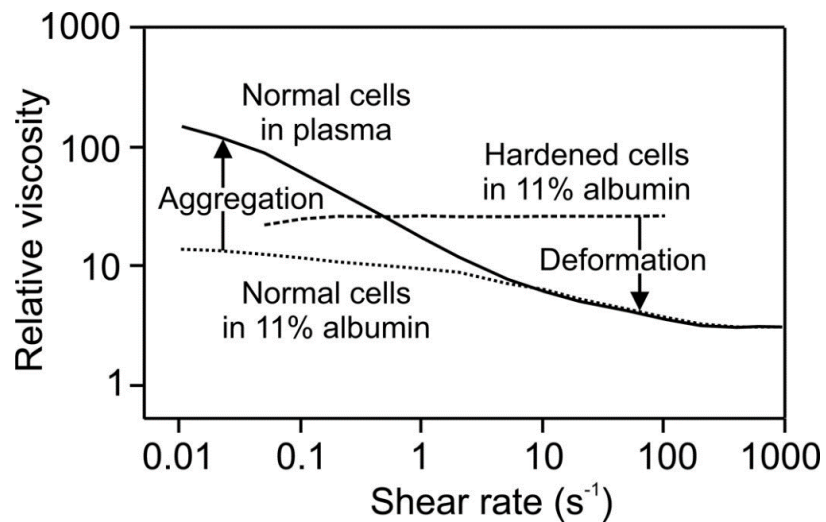


Figure 9. Dependence of the viscosity on the shear rate for three different red blood cells suspensions

In arteries with normal blood flow rates (in the range of hundreds or thousands), blood can be considered as a Newtonian fluid with good approximation [Secomb, 2017; Sousa et al. 2014], whose viscosity is approximately 3.5 cP (for 45% haematocrit) [Papaioannou and Stefanadis, 2005].

In addition, being a suspension of particles, the blood is not a homogeneous fluid. However, in vessels whose diameters are much larger than the suspended particles, it can be considered as a continuum [Secomb, 2017].

So, the blood can be characterized by both the viscosity and the density. These physical quantities are dependent on the temperature. The viscosity could depend also on the state of motion of the fluid. The density of the blood can be calculated as in Eq. 3:

$$\rho = (1 - Ht)\rho_p + Ht\rho_{rc} \quad \text{Eq. 3}$$

where Ht is the haematocrit,  $\rho_p$  is the plasma density ( $\rho_p=1035 \text{ kg/m}^3$ ) and  $\rho_{rc}$  is the particles density ( $\rho_{rc}=1090 \text{ kg/m}^3$ ). So, the blood density value is  $1060 \text{ kg/m}^3$ .

## 2.2 Reynolds number

The relationship between driving pressure and flow in a given vessel can be understood by considering the viscous and inertial forces acting on the blood.

The Reynolds number is defined as the ratio of the inertial term to the viscous term. So, if the fluid has density  $\rho$  and viscosity  $\mu$ , and the fluid flow is characterized by a typical velocity  $v$  and typical length  $L$  (for a tube  $L$  is the diameter), the Reynolds number (Re) is defined as follows:

$$\text{Re} = \frac{\rho v^2 / L}{\mu v / L^2} = \frac{\rho v L}{\mu} \quad \text{Eq. 4}$$

This dimensionless parameter allows to predict fluid flow conditions. When  $\text{Re} < 2000$  the inertial term is negligible and the flow is laminar, the fluid motion is smooth and orderly, fluid particles move in straight lines. If  $4000 < \text{Re} < 10000$  the flow is transitional, whereas when  $\text{Re} > 10000$  turbulent flow occurs, the flow is unstable and it involves unpredictable fluctuations of velocity.

The Reynolds numbers of arterial flow are in the range of hundreds to low thousands. So, in physiologic conditions, the blood flow is laminar or at most transitional, but flow fields can be sensitive to geometrical irregularities due to pathologic alterations or presence of vascular protheses in the vessel.

## 2.3 Navier Stokes equations

If  $\mathbf{v}=(v_x, v_y, v_z)$  is the velocity vector, then the conservation of mass implies that:

$$\frac{D\rho}{Dt} + \rho \left( \frac{\partial v_x}{\partial x} + \frac{\partial v_y}{\partial y} + \frac{\partial v_z}{\partial z} \right) = 0 \quad \text{Eq. 5}$$

where the material derivative  $\frac{D\rho}{Dt} = \frac{\partial \rho}{\partial t} + \mathbf{v}\nabla\rho$  has been introduced.

On the other hand, the conservation of momentum leads to:

$$\rho \frac{D\mathbf{v}}{Dt} = -\nabla p - \nabla \cdot \boldsymbol{\tau} + \rho \mathbf{g} \quad \text{Eq. 6}$$

where  $\frac{D\mathbf{v}}{Dt}$  is the material derivative of  $\mathbf{v}$ ,  $\nabla p$  is the pressure gradient,  $\mathbf{g}$  is the gravity force.

Continuity equation (Eq. 5) and momentum conservation equation (Eq. 6) are referred to as the Navier-Stokes equations.

Blood can be regarded as an incompressible fluid, so his density  $\rho=\rho(t,x,y,z)$  is constant. Therefore,  $\frac{D\rho}{Dt} = 0$  and continuity equation becomes:

$$\nabla \mathbf{v} = \mathbf{0} \quad \text{Eq. 7}$$

where  $\nabla \mathbf{v}$  is the velocity gradient.

In the case of incompressible Newtonian fluid, both  $\rho$  and  $\mu$  are constant, so momentum equation is the following:

$$\rho \frac{D\mathbf{v}}{Dt} = -\nabla p + \mu \nabla^2 \mathbf{v} + \rho \mathbf{g} \quad \text{Eq. 8}$$

where  $\nabla^2 \mathbf{v} = \nabla(\nabla \cdot \mathbf{v})$  is the Laplacian of  $\mathbf{v}$ .

Solving the Navier-Stokes equations, for a given geometry and a set of boundary conditions, predicts the fluid velocity and its pressure. Because of their complexity, these equations can be analytically solved only in a few simple cases. For complex geometries, Navier-Stokes equations have to be numerically solved.

## 2.4 Poiseuille's law

Assuming that blood is an ideal Newtonian fluid with constant viscosity, the vessel is straight, cylindrical and inelastic, the blood flow is steady (constant in time) and laminar and the flow is not subject to entrance effects (non-uniformities associated with the entrance of fluid into the vessel), then the velocity profile in the duct is parabolic (Figure 10) and it can be described by the Eq. 9.

$$v(r) = -\frac{\Delta P(R^2 - r^2)}{4\mu L} \quad \text{Eq. 9}$$

Where  $L$  is the length and  $R$  is the radius of the vessel,  $\Delta P$  is the pressure drop over the tube that supplies the driving force to the fluid, whose viscosity is  $\mu$ , to flow. The maximum velocity occurs at the centre of the pipe ( $r=0$ ), whereas at the wall ( $r=R$ ) the velocity is null. Integrating the velocity across the circular cross-section of the tube, it is possible to calculate the volume flow rate  $Q$  in the vessel as:

$$Q = \int_0^R 2\pi r v(r) dr = \frac{\pi R^4 \Delta P}{8\mu L} \quad \text{Eq. 10}$$

This equation is known as the Poiseuille's law. The mean velocity of flow in the tube is then given by Eq. 11:

$$v_{mean} = \frac{Q}{\pi R^2} = \frac{R^4 \Delta P}{8\mu L} \quad \text{Eq. 11}$$

The mean velocity of flow equals one half of the peak velocity at the center-line.

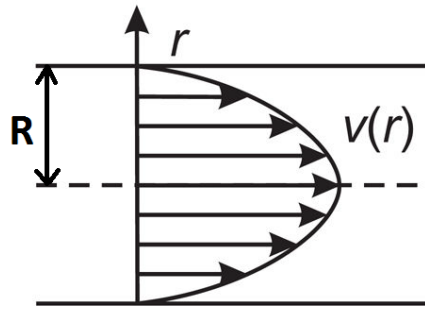


Figure 10. Poiseuille flow: parabolic velocity profile

One of the assumptions behind Poiseuille's law is that there are no entrance effects. When a fluid enters a tube, for the flow to be fully developed and the velocity profile to be parabolic, the fluid must travel a distance known as entrance length. The boundary layer is the region in which the combined effects of fluid viscosity and the no-slip condition produce a region of velocity transition adjacent to the wall. The thickness of the boundary layer increases until it equals the vessel radius (Figure 11). The entrance length  $L_e$  increases with the Reynolds number. For laminar flows,  $L_e$  is given approximately by:

$$L_e \sim 0.03 Re D \quad \text{Eq. 12}$$

where  $D$  is the diameter [Secomb, 2017].

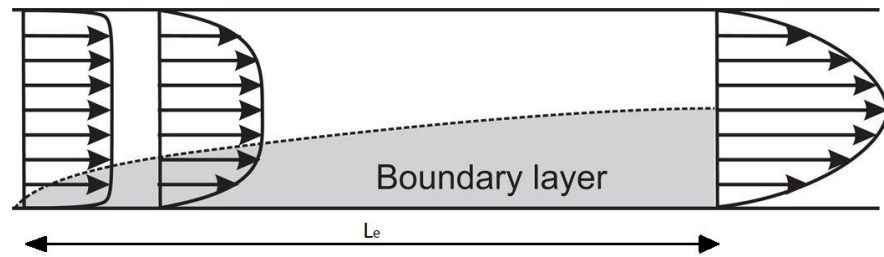


Figure 11. Development of boundary layer in fluid entering a pipe

The assumptions mentioned above are violated in the circulatory system because blood is not a Newtonian fluid, arteries are curved, non-uniform and deformable, the flow is pulsatile and the velocity profile is rarely fully parabolic because of pulsatility, branching and decrease of the radius of the arteries approaching the extremities. Nevertheless, the use of Poiseuille's law is widespread because it allows to obtain significant clinical results.

## 2.5 Wall Shear Stress

Considering Poiseuille flow in a pipe, the equilibrium of forces acting on a generic cylindrical volume of fluid with radius  $r$ , concentric with the pipe, subject to a pressure drop  $\Delta P$ , can be expressed as follows:

$$\tau 2\pi r L = \Delta P \pi r^2 \quad \text{Eq. 13}$$

So, the shear stress  $\tau$  is given by:

$$\tau = \frac{\Delta P r}{2L} \quad \text{Eq. 14}$$

The shear stress in the tube varies linearly with radial position, from zero at the center-line to a maximum value at the wall of the pipe, known as Wall Shear Stress (WSS). In the case under examination, the WSS is given by:

$$\text{WSS} = \frac{\Delta P R}{2L} \quad \text{Eq. 15}$$

In the circulatory system, the wall shear stress is the tangential force per unit area the flowing blood exerts on the endothelial cells lining the vessel lumen and it is computed as the shear stress at the wall. The magnitude of WSS depends on how fast the fluid velocity increases when moving from the vessel wall toward the centre of the vessel. In fact, according to Poiseuille's law, WSS can be expressed

as a function of the volume flow rate  $Q$  [Glagov *et al.*, 1988; Secomb, 2017], as indicated in Eq. 16.

$$WSS = \frac{4\mu Q}{\pi R^3} \quad \text{Eq. 16}$$

The spatial and temporal distribution of wall shear stress in arteries is sensitive to the geometry of the vessels as well as the pulsatile nature of the flow.

The WSS is mainly applied to the inner layer of the arterial wall in contact with the blood, the vascular endothelium, whereas normal stresses due to blood pressure are transferred to all vessel wall layers (intima, media and adventitia) [Papaioannou and Stefanidis, 2005].

## 2.6 Hemodynamics role in atherosclerosis

Atherosclerosis is associated with systemic risk factors including hypertension, smoking, hyperlipidemia, obesity and diabetes mellitus, that change the stiffness of arterial wall and lead to reduced artery compliance. Despite this, it is a focal disease, arterial atherosclerotic lesions are restricted to specific regions of the arterial tree, e.g. in the vicinity of branch points, the outer wall of bifurcations and the inner wall of curvatures, where disturbed flow occurs [Chatzizisis *et al.* 2007]. This suggests that hemodynamics and vessel geometry play a localizing role in the cause of plaque formation [Shaaban and Duerinckx, 2000]. In particular, atherosclerotic phenomena occur in vessels characterized by complex geometry and complex blood flow patterns [Gallo *et al.* 2014, Caruso *et al.* 2017].

The magnitude and rate of blood flow close to a vessel wall, which can be expressed using the concept of WSS, have been linked to the pathogenesis of atherosclerosis [Shaaban and Duerinckx, 2000]. Several investigations suggested that low and oscillating wall shear stress and the presence of recirculation and flow separation regions, where wall shear stress is near zero, but shear stress gradient is high, promote atherosclerosis progression [Glagov *et al.* 1988, Giddens *et al.* 1993, Zarins *et al.* 1983, Friedman *et al.* 1987, Wasilewski *et al.* 2013]. By contrast, high unidirectional wall shear stress may exert a protective effect against the induction of atheromatous lesions [Glagov *et al.* 1988, Moore *et al.* 1994].

Endothelial cells that line arterial walls are equipped with numerous mechanoreceptors capable of detecting and responding to mechanical signals, such as the shear stress resulting from blood flow, generating biochemical signals that modify signalling pathways, and gene and protein expression through a mechanism known as mechanotransduction. Laminar, axially symmetric and fully developed flow velocity profiles activate atheroprotective genes, maintaining

normal endothelial function, whereas low and oscillatory shear stresses trigger unfavourable gene expression, leading to endothelial dysfunction. Shear flow without a defined direction causes molecular signalling of pro-inflammatory and proliferative pathways. So, the variations in shear stress patterns makes branched points and curved regions prone to atherogenesis, whereas the straight part of arterial tree, where the flow has relatively straight streamlines with well-defined direction, is generally protected against atherosclerosis [Wasilewski et al. 2013, Chatzizisis et al. 2007].

Both low and oscillatory wall shear stress contribute to an increased fluid residence time, that may result in unfavourable alterations in endothelial cell metabolism and in mass transport of atherogenic substances [Glagov et al. 1988]. In fact, the prolonged residence time corresponds to a longer contact time of blood-borne particles that play a role in atherogenesis, such as platelets, macrophages and low density lipoproteins, with the artery wall [Pinto and Campos, 2016]. Consequently, the probability of retention and penetration of these flowing agents into the arterial wall increases [Chatzizisis et al. 2007].

Moreover, since the endothelial cells are normally aligned and elongated in the direction of blood flow, marked oscillations in the direction of wall shear stress may cause a variation in the shape of endothelial cells, that become more polygonal without a preferred alignment pattern, a loss of stress fiber orientation and a lack of organization of the cytoskeleton. These morphological changes may be responsible for the widening of the junctions between endothelial cells. These gaps, in combination with the prolongation of the residence time of circulating particles, cause an increase in permeability to macromolecules such as lipoproteins, that lead to focal lipid accumulation under the endothelium [Ku et al. 1985, Glagov et al. 1988, Chien S. 2008, Chatzizisis et al. 2007], and lead to vascular dysfunction including intimal hyperplasia, platelet activation, inflammatory reaction and reduced vasodilation [Hoi et al. 2011].

Furthermore, low wall shear stress reduces the bioavailability of nitric oxide, that possesses anti-inflammatory, anti-apoptotic, anti-mitogenic and anti-thrombotic properties, exposing the endothelium to the atherogenic effect of local and systemic risk factors [Chatzizisis et al. 2007].

The low-oscillatory shear theory has recently been debated because the co-localization of atherosclerotic lesions with areas of low wall shear stress is far from perfect as well as several articles, that were assumed to assess the validity of these theory, showed discrepancies in methods and results. Peiffer et al. [Peiffer et al. 2013a] made a systematic review of papers that investigated the correlation between atherosclerotic lesions prevalence and areas of low/oscillating wall shear stress and they concluded that the majority of the selected papers supported the consensus theory, but some contradicted it. Therefore, they stated that 'the evidence for the low-oscillatory shear theory is less robust than commonly assumed'.

More recently, temporal multidirectionality of haemodynamic stresses has been proposed as an important factor determining disturbed flow in arteries [Peiffer et al. 2013b]. The WSS does not remain parallel to a single axis throughout the cardiac cycle and the direction of WSS could influence the biology of endothelial cells, altering the balance between pro- and anti-atherosclerotic signals. So, the multidirectionality of near-wall flow is thought to be highly pro-atherogenic [Mohamied et al. 2015].

## 2.7 Carotid bifurcation

Carotid arteries are two main blood vessels that carry oxygenated blood to the brain and facial areas. Right and left carotid arteries are paired arteries running up along either side of the front of the neck that branches into two divisions. The right common carotid artery originates in the neck from the brachiocephalic trunk, while the left one arises from the aortic arch in the thorax (Figure 12) [8]. Each common carotid artery (CCA) divides itself into external carotid artery (ECA), that provides blood to the face and neck, and internal carotid artery (ICA), which takes a deeper path to supply blood to the brain, (Figure 12, Figure 13) [9].

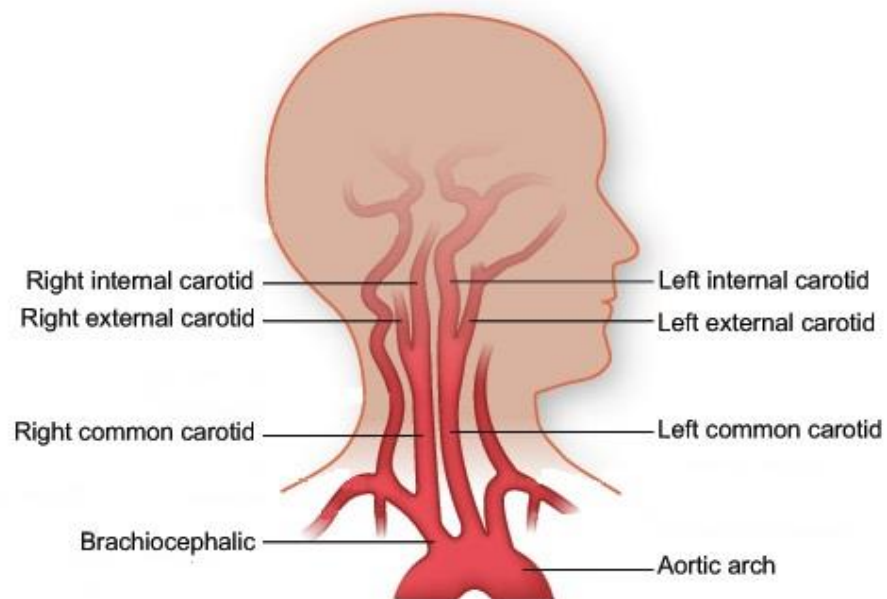


Figure 12. Carotid arteries

The carotid sinus, also known as carotid bulb, is a widening of a carotid artery at its branch point. This dilation involves the proximal portion of the ICA or the distal region of the CCA (Figure 13).

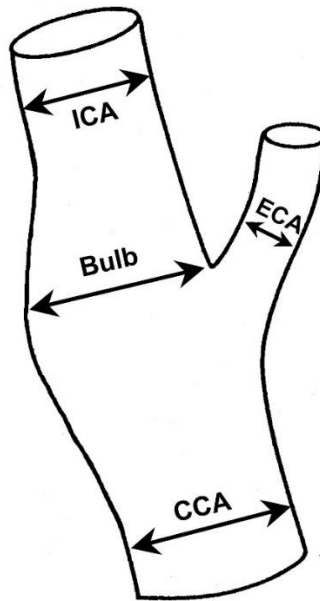


Figure 13. Carotid bifurcation

As previously mentioned, vessel morphology plays a fundamental role in determining complicated patterns of fluid velocities and wall shear stresses in blood vessels. So, the complex geometry of human carotid bifurcation makes the velocity profiles markedly asymmetric.

When a vessel curves, the change in flow direction involves a change in momentum, which is driven by a pressure gradient across the vessel cross-section, with higher pressure at the outside of the curve. The fluid near the centerline is driven outwards in the curve, whereas slower-moving fluid near the wall is driven toward the inside of the curve. As a consequence, blood velocity and wall shear stress are greater close to the outer wall than along the inner wall of the curvature. This sets up a secondary motion in the vessel cross-section, consisting of a pair of counter-rotating vortices called Dean vortices (Figure 15).

Moreover, depending on the flow and the geometry, flow separation may occur in bifurcation areas, so, the streamlines of fluid moving adjacent to the wall separate from the wall and reattach at downstream points, leading to a region of recirculating flow, with reversed shear stress at the wall (Figure 14). Swirling flows may also occur in major arteries (Figure 14), leading to more uniform shear stress acting on arterial walls [Secomb, 2017] and suppressing disturbed flow. So, helical flow can modify near-wall transport topology, reducing the accumulation of atherogenic substances on the vessel wall and therefore protecting against atherosclerosis [Arzani and Shadden, 2016].

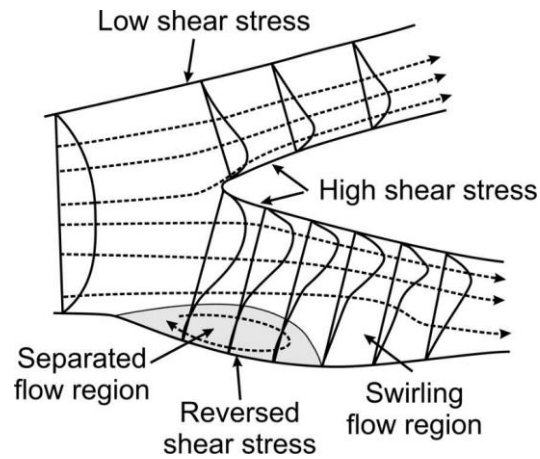


Figure 14. Blood velocity pattern in a carotid bifurcation

All the above-mentioned phenomena determine disturbed flow conditions in the carotid bifurcation and especially in the carotid bulb (Figure 15), making it a common site of atherosclerosis appearance. The regions close to the flow divider are characterized by with higher blood velocities and shear stresses (Figure 15). On the opposite sides of the vessel, the velocities and wall shear stresses are much lower (Figure 15). Furthermore, the flow is typically unidirectional and laminar throughout the cardiac cycle at the inner wall on the flow divider side, whereas lateral wall is a region of flow separation, formation of complex flow patterns and vortices. So, the outer wall of the proximal segment and sinus of the ICA are preferential sites for atherosclerotic plaque formation [Glagov et al. 1988].

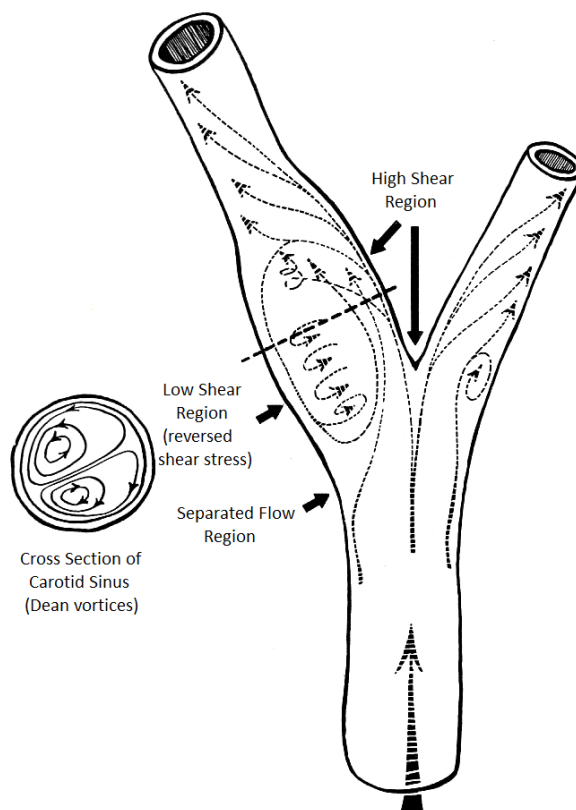


Figure 15. Flow phenomena occurring in a human carotid bifurcation

## Chapter 3. Hemodynamic wall descriptors

A variety of hemodynamic wall parameters (HWPs) has been proposed over the years to quantify haemodynamic disturbances as potential predictors or indicators of vascular wall dysfunction [Lee *et al.* 2009]. These descriptors reduce the complexity of the four-dimensional blood flow field, aid the prediction of disturbed flow conditions in the vessels and play a significant role in the detection of potential zones of atherosclerosis development.

For the aforementioned reasons, the majority of haemodynamic parameters are based on the wall shear stress. The most used HWPs are the followings:

### 3.1 TAWSS: Time Averaged Wall Shear Stress

$$TAWSS = \frac{1}{T} \int_0^T |\mathbf{WSS}| dt \quad \text{Eq. 17}$$

where T is the cardiac cycle period, during which the WSS vector is measured, and t is the time.

The Time Averaged Wall Shear Stress evaluates the total shear stress exerted on the wall throughout a cardiac cycle. Low TAWSS values (lower than 0.4 Pa), which are typically associated with disturbed flow regions, where the flow is slow and changes direction within the cardiac cycle, stimulate atherogenic phenotype, moderate TAWSS values (between 1.5 Pa and 10 Pa) induce endothelial quiescence and an atheroprotective gene expression profile [Malek *et al.* 1999, Dolan *et al.* 2013], high TAWSS values (greater than 10-15 Pa) can lead to endothelial trauma and haemolysis [Gallo *et al.* 2014] and to plaque destabilization and ulceration in stenosed vessels [Sousa *et al.* 2014; Dolan *et al.* 2013].

### 3.2 OSI: Oscillatory Shear Index

$$OSI = 0.5 \left[ 1 - \left( \frac{\left| \int_0^T \mathbf{WSS} dt \right|}{\int_0^T |\mathbf{WSS}| dt} \right) \right] \quad \text{Eq. 18}$$

The Oscillatory Shear Index is a dimensionless metric that accounts for the deviation of the WSS from its average direction, identifying regions on the vessel wall subjected to highly oscillating WSS, that may induce perturbed endothelial cells alignment and consequently plaque formation. In fact, during the cardiac cycle the WSS vector transiently alternates between the positive and negative axial directions.

This descriptor ranges from a minimum of zero, indicating a unidirectional WSS, to a maximum of 0.5, highlighting a purely oscillatory WSS. However, the OSI does not distinguish between uniaxial reversing flow from multidirectional flow [Mohamied *et al.* 2015]. Moreover, OSI is insensitive to shear magnitude, so it might be better employed in combination with other shear measures.

### 3.3 RRT: Relative Residence Time

$$RRT = \frac{1}{\left| \int_0^T \mathbf{wss} dt \right|} \sim \frac{1}{(1-2OSI)TAWSS} \quad \text{Eq. 19}$$

The Relative Residence Time is proportional to a combination of TAWSS and OSI, so it provides a single measure of low and oscillatory WSS [Lee *et al.* 2009]. RRT measures how long the particles stay near the vessel wall, it should take a value between 0 and infinite, so elevated RRT value (higher than 8 Pa<sup>-1</sup>), that corresponds to low TAWSS and high OSI, indicates a potential zone of atherosclerosis appearance [Pinto and Campos, 2016].

The descriptors quantifying low and oscillatory wall shear stress are significant, but moderately weak predictors of vascular wall dysfunction [Gallo *et al.*, 2016]. As said above, some studies showed that multidirectionality of WSS during the cardiac cycle may be a more significant factor, well correlated with the biological response of endothelial cells. TAWSS, OSI and RRT indices are unable to distinguish between uniaxial pulsatile flow and multidirectional flow. So, to capture the temporal multidirectionality of the near-wall blood flow field, Peiffer *et al.* [Peiffer *et al.* 2013b] proposed a new metric, the transverse Wall Shear Stress, whereas Morbiducci *et al.* [Morbiducci *et al.* 2015] introduced the axial Wall Shear Stress.

### 3.4 transWSS: transverse Wall Shear Stress

$$transWSS = \frac{1}{T} \int_0^T \left| \mathbf{WSS} \left( \mathbf{n} \times \frac{\int_0^T \mathbf{wss} dt}{\left| \int_0^T \mathbf{wss} dt \right|} \right) \right| dt \quad \text{Eq. 20}$$

where  $\mathbf{n}$  represents the normal to the arterial surface.

The transverse Wall Shear Stress is the time-average of the components of the instantaneous WSS vector that are perpendicular to the mean flow direction, with which endothelial cells are assumed to align. The definition of this parameter is supported by the hypothesis that endothelial cells may be adversely affected by cross-flow [Mohamied *et al.* 2017]. TransWSS can take any value between zero and the TAWSS. A low transWSS indicates that the flow remains approximately parallel to a single axis throughout the cardiac cycle, while a high transWSS indicates large changes in flow direction, or smaller

changes in direction over a large portion of the cardiac cycle, or small changes in the direction of high-speed near wall flow. TransWSS distinguishes between uniaxial and multidirectional flows, but it does not differentiate between purely forward flow and reversing unidirectional flow, both of which have a transWSS of zero, so it can only complement TAWSS, OSI and RRT, rather than replace them [Peiffer et al. 2013b]. Moreover, transWSS cannot be defined if there is not a dominant flow direction, as in the theoretical case of purely oscillatory flow.

Mohamied et al. [Mohamied et al. 2015] demonstrated that transWSS changes with age, in agreement to the variation of stresses and the evolution of the pattern of atherosclerotic lesion prevalence that occur from immature to mature age around branch ostia of rabbit aortas.

### 3.5 CFI: Cross Flow Index

The instantaneous cross flow index (CFI<sub>i</sub>), defined at the i-th time point, was introduced by Mohamied et al. [Mohamied et al. 2017] as the ratio between instantaneous transWSS and WSS, as specified below:

$$CFI_i = \frac{transWSS_i}{WSS} = \frac{WSS}{|WSS|} \cdot \left( \mathbf{n} \times \frac{\int_0^T WSS dt}{\left| \int_0^T WSS dt \right|} \right) \quad \text{Eq.21}$$

It represents the directionality of WSS, being the sine of the angle between the cycle-averaged WSS vector and the instantaneous WSS vector. Time-averaging these instantaneous values over the cardiac cycle, the Cross Flow Index can be obtained as:

$$CFI = \frac{1}{T} \int_0^T \frac{WSS}{|WSS|} \cdot \left( \mathbf{n} \times \frac{\int_0^T WSS dt}{\left| \int_0^T WSS dt \right|} \right) dt \quad \text{Eq. 22}$$

Mohamied et al. [Mohamied et al. 2017] used two geometries of immature rabbit thoracic aortas and demonstrated that CFI<sub>i</sub> is high when the flow is nearly stagnant, for example during diastole, it reaches its maximum value in case of flow reversal, whereas CFI is at its lowest at peak systole, when the WSS is maximal. Indeed, portions of the cardiac cycle where the WSS is highest influence mostly the cycle-averaged WSS, so in these parts of the cycle the instantaneous WSS vector deviates least from the temporal mean WSS vector, and consequently CFI is low.

### 3.6 WSS<sub>ax</sub>: Axial Wall Shear Stress

The Axial Wall Shear Stress [Morbiducci et al. 2015] is a metric for the analysis of WSS temporal multidirectionality that defines a different preferential flow direction with respect to that proposed by Peiffer et al. [Peiffer et al. 2013b]. Morbiducci et al. used the streamwise axis of the vessel, instead of the cycle-averaged WSS vector direction. This choice could be helpful in regions of complex flow, where there is no predominant WSS direction.

More in detail, Morbiducci et al. [Morbiducci et al. 2015] defined the Axial Wall Shear Stress at every point on the vascular surface as the projection of WSS vector along the direction  $C'$  of the tangent to the centerline (i.e. the set of the points computed as the centres of maximal spheres inscribed in the vessel lumen) of the vessel, as illustrated by the following equation:

$$WSS_{ax} = \frac{WSS \cdot C'}{|C'|} \frac{C'}{|C'|} \quad \text{Eq. 23}$$

$WSS_{ax}$  is a signed quantity, that assumes a positive value when the axial WSS projection is aligned with the centerline and directed with forward flow, while it is negative when the flow is reversed. A null  $WSS_{ax}$  identifies regions with no predominant direction of axial WSS, where flow separation occurs.

### 3.7 WSSG: Wall Shear Stress Spatial Gradient

$$WSSG = \frac{1}{T} \int_0^T \sqrt{\left(\frac{\partial WSS_p}{\partial p}\right)^2 + \left(\frac{\partial WSS_n}{\partial n}\right)^2} dt \quad \text{Eq. 24}$$

where  $p$  and  $n$  are respectively the directions parallel and normal to the direction of the time-average WSS vector.

The Wall Shear Stress Spatial Gradient is the spatial derivative of WSS along the flow direction with respect to the streamwise distance and it may be considered a marker of endothelial cell tension. [Lee et al. 2009]. The WSSG of fully-developed flow in a straight uniform pipe is zero. Positive WSSG (increasing WSS along the flow direction) inhibits while negative WSSG promotes flow-induced endothelial cells alignment [Dolan et al. 2013]. Large endothelial spatial gradients produce an increase in wall permeability [Arzani and Shadden, 2016] and endothelium dysfunction due to spatially changing hemodynamic forces [Gallo et al. 2014].

### 3.8 WSSAG: Wall Shear Stress Angle Gradient

$$WSSAG = \frac{1}{T} \frac{D}{\pi} \int_0^T |\nabla \Phi_n| dt \quad \text{Eq. 25}$$

where  $D$  is the vessel diameter and

$$\Phi_n = \arccos\left(\frac{WSS_i WSS_j}{|WSS_i| |WSS_j|}\right) \quad \text{Eq. 26}$$

is the scalar field of the WSS angle deviation, where  $WSS_i$  is the vector at the location of interest and  $WSS_j$  represents the surrounding stress vectors (shear and normal stress).

The Wall Shear Stress Angle Gradient is a mesh-independent measure of the angle between adjacent wall shear vectors, it highlights regions exposed to large spatial variations in the mean WSS direction, irrespective of magnitude [Lee et al. 2009], as regions of flow separation and flow reattachment, so it has been proposed as a marker for sites of possible dysfunctional endothelial cells [Augst et al. 2007]. Elevated WSSAG values may lead to changes in endothelial cell architecture, increase in cell turnover linked to enhanced wall permeability, and development of arterial disease at particular sites [Hyun et al. 2002].

### 3.9 WSST: Wall Shear Stress Temporal gradient

$$WSST = \max\left(\left|\frac{\partial |WSS|}{\partial t}\right|\right) \quad \text{Eq. 27}$$

The Wall Shear Stress Temporal gradient is the maximum absolute rate of change in WSS magnitude over the cardiac cycle [Lee et al. 2009] at each spatial position in the domain.

White et al. demonstrated that temporal gradients in shear stress stimulate endothelial cell proliferation [White et al. 2001]. Intimal thickening caused by the mitogenic effect of high focal WSST, combined with cell-disorientation and widening of junctions in the endothelium are regarded as possible initiators to atherogenesis in regions of recirculation. The combination of high WSST with elevated RRT values could enhance the diffusion of atherogenic substances in combination with high residence times. So, peak temporal WSS gradient has been proposed as a complementary parameter for the detection of plaque prone regions in complex geometries [Van Wick et al. 2014].

According to the study carried out by Lee et al. on carotid bifurcations, [Lee et al. 2009] elevated values of WSS temporal gradient are concentrated around the bifurcation apex, that is usually not subject to atherosclerosis.

The frequency content of shear variations that occur over a cardiac cycle may also be a contributing factor in lesion development. So, some hemodynamic parameters based on the harmonic content of the shear stress waveform have been proposed recently.

### 3.10 DH: Dominant Harmonic

$$DH = \max\left(F_{|WSS|}\left(n\frac{2\pi}{T}\right)\right), n \in N^+ \quad \text{Eq. 28}$$

where  $F_{|WSS|}$  is the Fourier transform of the time-varying waveform of the WSS magnitude and  $n$  is a positive integer.

The Dominant Harmonic is thus defined as the highest harmonic obtained through the Fourier decomposition of the WSS along the cardiac cycle [Gallo *et al.* 2014].

Himburg and Friedman demonstrated that, while most of the arteries experienced shear forces predominantly at the frequency of the heart rate (that is the first harmonic), the frequency spectra at certain regions were dominated by shear forces at higher frequencies. More in detail, they found in porcine iliac artery an inverse relationship between TAWSS and DH, suggesting that complex vascular regions, where the WSS is low, are dominated by higher harmonics [Himburg and Friedman, 2006].

### 3.11 HI: Harmonic Index

$$HI = \frac{\sum_{n=1}^{\infty} F_{|WSS|}\left(n\frac{2\pi}{T}\right)}{\sum_{n=0}^{\infty} F_{|WSS|}\left(n\frac{2\pi}{T}\right)}, n \in N^+ \quad \text{Eq. 29}$$

The Harmonic Index is a measure of the relative fraction of the harmonic amplitude spectrum arising from the pulsatile flow component. It ranges from zero, in the case of a steady nonzero shear stress signal, to 1, in the case of purely oscillatory signal with a time average of zero. The harmonic index colocalizes with OSI, confirming a relationship between specific frequency components and atherosclerosis development [Gelfand *et al.* 2006].

Lee *et al.* made an evaluation of correlations among HWPs at the normal carotid bifurcation, demonstrating that some of these parameters may be considered redundant. More in detail, the three magnitude-based HWPs (TAWSS, OSI and RRT) were strongly correlated, suggesting RRT as a single marker of low and oscillatory WSS, with a tangible connection to the biological mechanisms underlying atherosclerosis. WSSG and WSST showed a moderate positive

correlation with TAWSS, which suggests that TAWSS could be used instead of gradient-based HWPs, that are more susceptible to measurement uncertainty. The harmonic-based parameter HI was moderately correlated with the three magnitude-based parameters, while DH was only weakly correlated with other HWPs, showing to be essentially independent of the others HWPs [Lee et al. 2009]. Lastly, Gallo et al. demonstrated that the multidirectionality descriptor transWSS is not colocalized with OSI. It may represent different hemodynamic disturbances at the carotid bifurcation, with a different impact on endothelial cells [Gallo et al. 2016], so it could complement the information given by magnitude-based HWPs.

## Chapter 4. Methods

In this work, new haemodynamic descriptors based on the wall shear stress divergence have been investigated. The analysis was performed on forty-six image-based carotid bifurcation models. Aim of this study was to verify if these parameters could be useful to atherosclerosis prediction and if they are correlated with the existing well-established HWPs. To do it, an analysis of the co-localization of these parameters was carried out.

### 4.1 Computational fluid dynamics modelling

Data used in this study are a subset selected from the “Vascular Aging - The Link That Bridges Age to Atherosclerosis” validate study. The right carotid artery geometries of seemingly healthy participants were acquired from contrast-enhanced angiography (CEMRA). In a study by [Gallo *et al.* 2015] lumen geometries were reconstructed from their brachiocephalic origin to well above the bifurcation using the open-source Vascular Modelling Toolkit VMTK. To ensure fully developed velocity profiles at the CCA inlet and to minimize the influence from outlet boundary conditions, flow extensions were added to the inlet and outlet faces of all models. Computational fluid dynamics simulations were carried out by Gallo *et al.* [Gallo *et al.* 2016] following the methods described in [Hoi *et al.* 2010]. The finite volume method was adopted to solve the governing equations of the fluid motion. More in detail, tetrahedral element meshes were generated by ANSYS ICEM-CFD software with a node spacing of 0.1-0.2 mm, which was previously shown to successfully resolve wall shear stresses at normal carotid bifurcation geometries. Inlet and outlet velocities were acquired from phase contrast magnetic resonance (PCMRI) sequences. So, fully developed, pulsatile, patient-specific velocity profile boundary conditions were imposed at the CCA inlet and ICA outlet. Traction-free boundary conditions were imposed at the ECA outlet. Rigid walls and Newtonian rheology with constant blood viscosity of 0.00371 kg/m\*s were assumed for all models. The CFD simulations were carried out using 4800 time steps per cardiac cycle.

### 4.2 Wall shear stress divergence

The divergence ( $\nabla \cdot$ ) is a vector operator which takes as input a vector-valued function defining a vector field and outputs a scalar-valued function [5] measuring the overall tendency of the field to converge toward or diverge from a point [Saenz, 2013]. The divergence measures the flux of a tangent vector field throughout an infinitesimal region of space around each point [De Goes *et al.*

2015]. If the vector field points outward from a point, its divergence would have a positive value in that region (Figure 16, Panel B). In contrast, if the vector field moves toward a point, then the divergence has a negative value (Figure 16, Panel A) [6]. This physical interpretation allows to use divergence to identify sources (points of positive divergence) and sinks (points of negative divergence) of a vector field [5]. The net flow outwards from a region is given by the sum of all sources minus the sum of all sinks. So, if the divergence at a point is zero (Figure 16, Panel C), then any infinitesimal closed surface around that point has no net flow across it [7]. If a vector field has zero divergence everywhere, it is called incompressible or solenoidal.

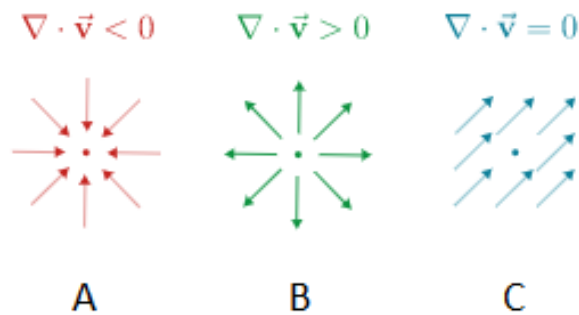


Figure 16. Physical interpretation of the divergence of a vector field  $\vec{v}$ : A) Sink B) Source C) Point with zero divergence

Given the three-dimensional tangent vector field representing the wall shear stress written in cartesian coordinates ( $\mathbf{WSS} = WSS_x \mathbf{i} + WSS_y \mathbf{j} + WSS_z \mathbf{k}$ ), the Wall Shear Stress divergence is a scalar-valued function defined as described by Eq. 30:

$$\nabla \cdot \mathbf{WSS} = \frac{\partial WSS_x}{\partial x} + \frac{\partial WSS_y}{\partial y} + \frac{\partial WSS_z}{\partial z} \quad \text{Eq. 30}$$

Where  $\nabla \cdot \mathbf{WSS} = \left( \frac{\partial}{\partial x}, \frac{\partial}{\partial y}, \frac{\partial}{\partial z} \right) \cdot (WSS_x, WSS_y, WSS_z)$  is the “dot product” between the gradient operator  $\nabla$  and the component functions of WSS.

As previously said, the endothelial cells lining blood vessels respond to both magnitude and directional changes of WSS. The above-mentioned haemodynamic wall parameter called OSI is able to identify regions subjected to oscillating WSS, but it cannot distinguish tensile from compressive force. So, to consider both the magnitude and the directionality of WSS, Zhang et al. proposed the use of wall shear stress divergence as a parameter to predict the aneurysm rupture. Wall shear stress divergence takes into account the gradient and the direction of WSS

and can be used to identify tensile and compressive regions on the aneurysm surface [Zhang et al. 2013].

According to this view, WSS divergence could also be helpful to highlight WSS directionality and the oscillatory behaviour of wall shear stress in vascular regions that could be affected by atherosclerotic plaque formation.

A positive value of WSS divergence at a point identifies an expansion at that region, and in this case the net effect of WSS is to stretch the vascular surface, otherwise WSS compresses the endothelial layer. The magnitude of WSS divergence represents the intensity of stretching or compression [Zhang et al. 2013].

### 4.3 Wall shear stress divergence computation

The available forty-six carotid bifurcation surfaces were discretized with triangle meshes made-up of about 4,000,000 elements. To obtain a discrete representation of the wall shear stress vector field on the vascular surfaces, a vertex-based representation was chosen. The wall shear stress tangent vector field was described through three values  $WSS_x$ ,  $WSS_y$ ,  $WSS_z$  (one for each coordinate) on each vertex of the triangles. Given the coordinates of the vertices at which the vector field was sampled, the values of the three components of WSS were defined on the nodes of every grid storing a scalar field for each coordinate.

The WSS vector field components were defined over each triangle utilizing a piecewise-linear interpolation. The three values associated to each mesh vertex were interpolated linearly inside each triangle:

$$WSS(x) = (WSS_x)_i B_i(x) + (WSS_x)_j B_j(x) + (WSS_x)_k B_k(x) \quad \text{Eq. 31}$$

$$WSS(y) = (WSS_y)_i B_i(y) + (WSS_y)_j B_j(y) + (WSS_y)_k B_k(y) \quad \text{Eq.32}$$

$$WSS(z) = (WSS_z)_i B_i(z) + (WSS_z)_j B_j(z) + (WSS_z)_k B_k(z) \quad \text{Eq. 33}$$

The vertices of each triangle are indicated with the letters  $i$ ,  $j$  and  $k$  respectively.  $B_i$ ,  $B_j$  and  $B_k$  are linear basis functions, whose linear combination allows to interpolate every continuous function.

It follows that the gradients of the components of WSS can be obtained by differentiating these vertex-based basis functions, as described by Equations 34, 35 and 36.

$$\nabla WSS(x) = (WSS_x)_i \nabla B_i(x) + (WSS_x)_j \nabla B_j(x) + (WSS_x)_k \nabla B_k(x) \quad \text{Eq. 34}$$

$$\nabla WSS(y) = (WSS_y)_i \nabla B_i(y) + (WSS_y)_j \nabla B_j(y) + (WSS_y)_k \nabla B_k(y) \quad \text{Eq. 35}$$

$$\nabla WSS(z) = (WSS_z)_i \nabla B_i(z) + (WSS_z)_j \nabla B_j(z) + (WSS_z)_k \nabla B_k(z) \quad \text{Eq. 36}$$

More in detail, referring to Figure 17,  $\nabla B_i(x)$  is given by:

$$\nabla B_i(x) = \frac{1}{h(t)} = \frac{(x_k - x_j)^\perp}{2A_T} \quad \text{Eq. 37}$$

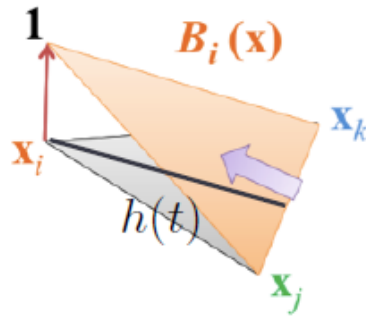


Figure 17. Triangle of the mesh and linear basis function differentiation.

Analogous calculi allow the differentiation of the other linear basis functions.

So, the gradients of WSS were computed in each triangle, along the directions of the cartesian space, according to the following equations, in Matlab (The MathWorks Inc.) software:

$$\nabla WSS(x) = \frac{(WSS_x)_i}{2A_T} (x_k - x_j)^\perp + \frac{(WSS_x)_j}{2A_T} (x_i - x_k)^\perp + \frac{(WSS_x)_k}{2A_T} (x_j - x_i)^\perp \quad \text{Eq. 38}$$

$$\nabla WSS(y) = \frac{(WSS_y)_i}{2A_T} (y_k - y_j)^\perp + \frac{(WSS_y)_j}{2A_T} (y_i - y_k)^\perp + \frac{(WSS_y)_k}{2A_T} (y_j - y_i)^\perp \quad \text{Eq. 39}$$

$$\nabla WSS(z) = \frac{(WSS_z)_i}{2A_T} (z_k - z_j)^\perp + \frac{(WSS_z)_j}{2A_T} (z_i - z_k)^\perp + \frac{(WSS_z)_k}{2A_T} (z_j - z_i)^\perp \quad \text{Eq. 40}$$

Where the single triangle  $ijk$  has an area  $A_T$  and three vertices with coordinates  $(x_i, y_i, z_i)$ ,  $(x_j, y_j, z_j)$  and  $(x_k, y_k, z_k)$ , respectively. So,  $(WSS_x)_i$  represents the x-component of the WSS in the node  $i$ ,  $(x_k - x_j)^\perp$  indicates the vector having length equal to

the edge connecting nodes  $k$  and  $j$ , and direction perpendicular to it, and so on, as depicted in Figure 18.

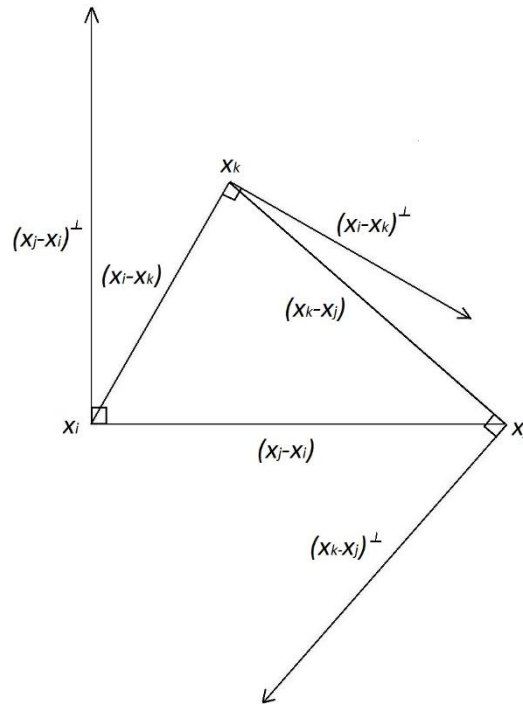


Figure 18. Generic triangle of the mesh with auxiliary vectors for the computation of WSS gradient.

Then, the divergence of wall shear stress was computed inside every triangle as the sum of the WSS gradients along the three spatial directions, as specified below:

$$\nabla \cdot \mathbf{WSS} = \nabla WSS(x) + \nabla WSS(y) + \nabla WSS(z) \quad \text{Eq. 41}$$

Lastly, the divergence of the wall shear stress was evaluated at the nodes of the triangle mesh. Specifically, at the  $n$ -th node of the grid,  $\nabla \cdot \mathbf{WSS}$  was computed as the weighted average of the wall shear stress divergence values in all the  $t$  triangles that shared that node, as analytically described in the following equation:

$$\nabla \cdot \mathbf{WSS}(n) = \frac{\sum_{m=1}^t \nabla \cdot \mathbf{WSS}(m)}{t} \quad \text{Eq. 42}$$

For example,  $\nabla \cdot \mathbf{WSS}$  in the node  $n$  in Figure 19 is given by

$$\nabla \cdot \mathbf{WSS}(n) = \frac{\sum_{m=1}^5 \nabla \cdot \mathbf{WSS}(m)}{5}.$$

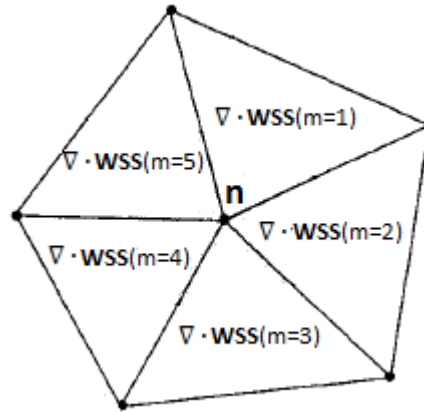


Figure 19. Example of computation of  $\text{divWSS}$  in a node of the mesh.

The wall shear stress divergence scalar field was thus specified at the mesh nodes.

#### 4.4 Normalized WSS vector field divergence

The divergence of WSS vector field takes into account both the magnitude and the direction of WSS. So, considering the value of the divergence of WSS vector field, it is not possible to distinguish if a positive value of  $\nabla \cdot \mathbf{WSS}$  is due to the source arrangement of WSS field (Figure 20, panel A) or to an increase in WSS magnitude (Figure 20, panel B), and analogously if a negative  $\nabla \cdot \mathbf{WSS}$  value is owed to a WSS field with sink configuration (Figure 20, panel C) or to a decrease in WSS magnitude (Figure 20, panel D). Moreover, a WSS vector field that has a uniform direction but variable magnitude of WSS vectors (Figure 20, panels B and D), is characterized by a nonzero  $\nabla \cdot \mathbf{WSS}$  value.

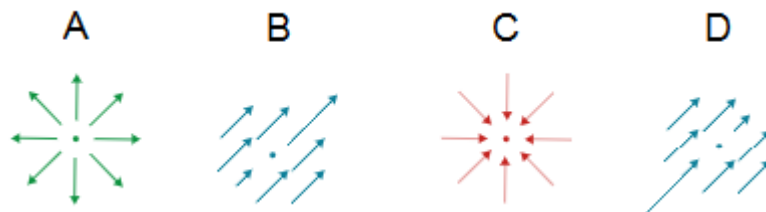


Figure 20. WSS field configurations: A) and B) positive divergence; C) and D) negative divergence

So, in this work, the values of WSS components were divided by their moduli, with the aim to obtain unit vectors over the entire surface. Then, it was computed the divergence of the normalized WSS vector field (Eq. 43) at the nodes of each carotid bifurcation surface, with the methods described in the previous paragraph. This choice allows to make an evaluation of the WSS directionality, neglecting the variations in WSS magnitude.

$$divWSS = \nabla \cdot \left( \frac{WSS}{|WSS|} \right) \quad \text{Eq. 43}$$

#### 4.5 WSS divergence-based parameters

In this work, the cardiac cycle was divided into 120 time steps and they were computed the values that the divergence of the normalized wall shear stress takes at these instants. To synthesize the temporal information, it was considered the temporal average of the WSS divergence over the cardiac cycle, as described by the following equation:

$$\overline{divWSS} = \frac{1}{T} \int_0^T \nabla \cdot \left( \frac{WSS}{|WSS|} \right) dt \quad \text{Eq. 44}$$

where T is the cardiac period.

Three novel parameters based on wall shear stress divergence were then considered:

- Positive WSS Divergence (DivP);
- Negative WSS Divergence (DivN);
- Oscillatory WSS Divergence Index (ODI).

DivP was defined as an array containing the values of  $\overline{divWSS}$  in correspondence of the nodes in which the temporal average of the divergence of the normalized WSS is positive, otherwise zero. Analogously, DivN is an array containing the values of  $\overline{divWSS}$  in correspondence of the nodes of the model characterized by a negative mean value of  $divWSS$ , zero values in correspondence of the other nodes. To account for the temporal changes of WSS divergence, ODI was computed in each node as the standard deviation of  $divWSS$  over the cardiac cycle (Eq. 45).

$$ODI = \sqrt{\frac{\sum_{i=1}^N \left( \left( \nabla \cdot \frac{WSS}{|WSS|} \right)_i - \overline{divWSS} \right)^2}{N-1}} \quad \text{Eq. 45}$$

DivP is capable of capturing regions of the vessel that are stretched by a shear stress with a source configuration, whereas DivN can highlight areas where the wall shear stress assumes a sink arrangement, compressing the vessel wall. On the other hand, ODI identifies vessel regions that are exposed to a wall shear stress that alternatively diverges and converges.

The definition of ODI is clarified by the observation that a high value of the standard deviation corresponds to large fluctuations of *divWSS* value during the cardiac cycle. Analysing the values taken by the divergence during the cardiac cycle in every node, it was observed that *divWSS* exhibit nearly-normal probability density distributions for all the forty-six carotid bifurcation models. An example of the probability density estimates of *divWSS* values taken during the cardiac cycle in all the nodes of a specific model is shown in Figure 21, whereas in Figure 22 are reported the probability density estimates of the spatial averages of *divWSS* values taken during the cardiac cycle for all the 46 carotid models.

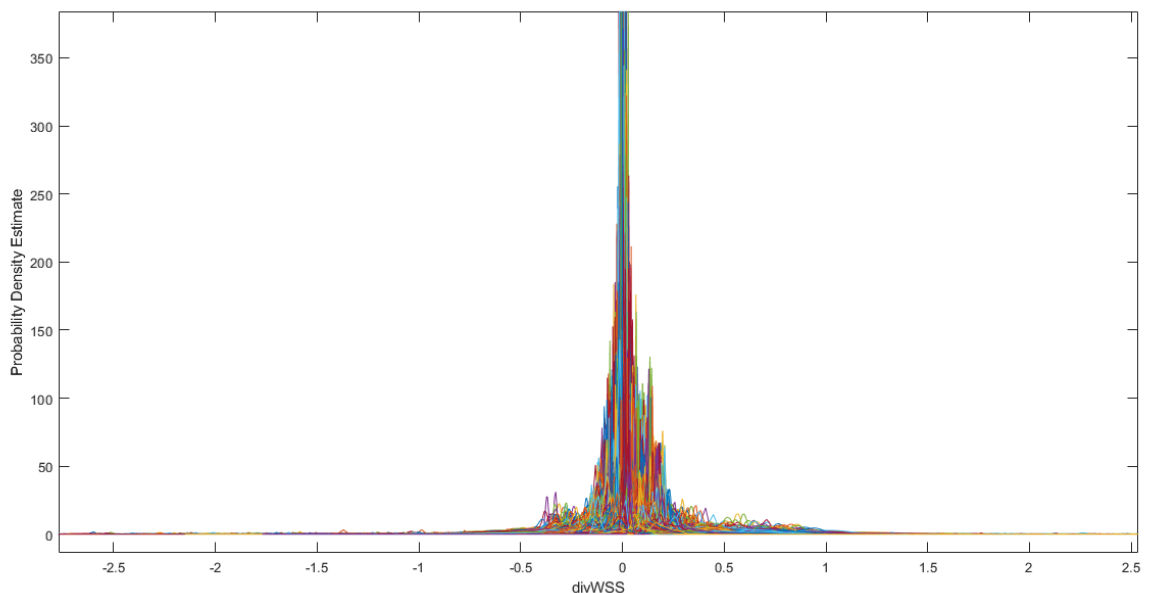


Figure 21. Probability density estimates of *divWSS* values taken during the cardiac cycle in the nodes of one of the carotid bifurcation models.

The values of the divergence of the normalized WSS are roughly symmetrically-distributed around the mean value, that is close to zero for all the considered carotid bifurcations (Figure 22). So, if a region is exposed to a large *divWSS* standard deviation, it can be subject to sign variations of *divWSS* during the cardiac cycle. Then, high ODI values can describe alternating directional changes of the WSS. That is to say, the tangential stress acting on the regions of the luminal surface where ODI takes high values may switch repeatedly between tensile and compressive throughout the whole cardiac cycle.

To verify that the information given by the ODI was actually related to the oscillations between positive and negative values of the divergence of the normalized wall shear stress, a counter was introduced. It counts the number of consecutive sign changes of the *divWSS* over the 120 time steps in which the cardiac cycle was divided, and it was computed at all the nodes of every model.

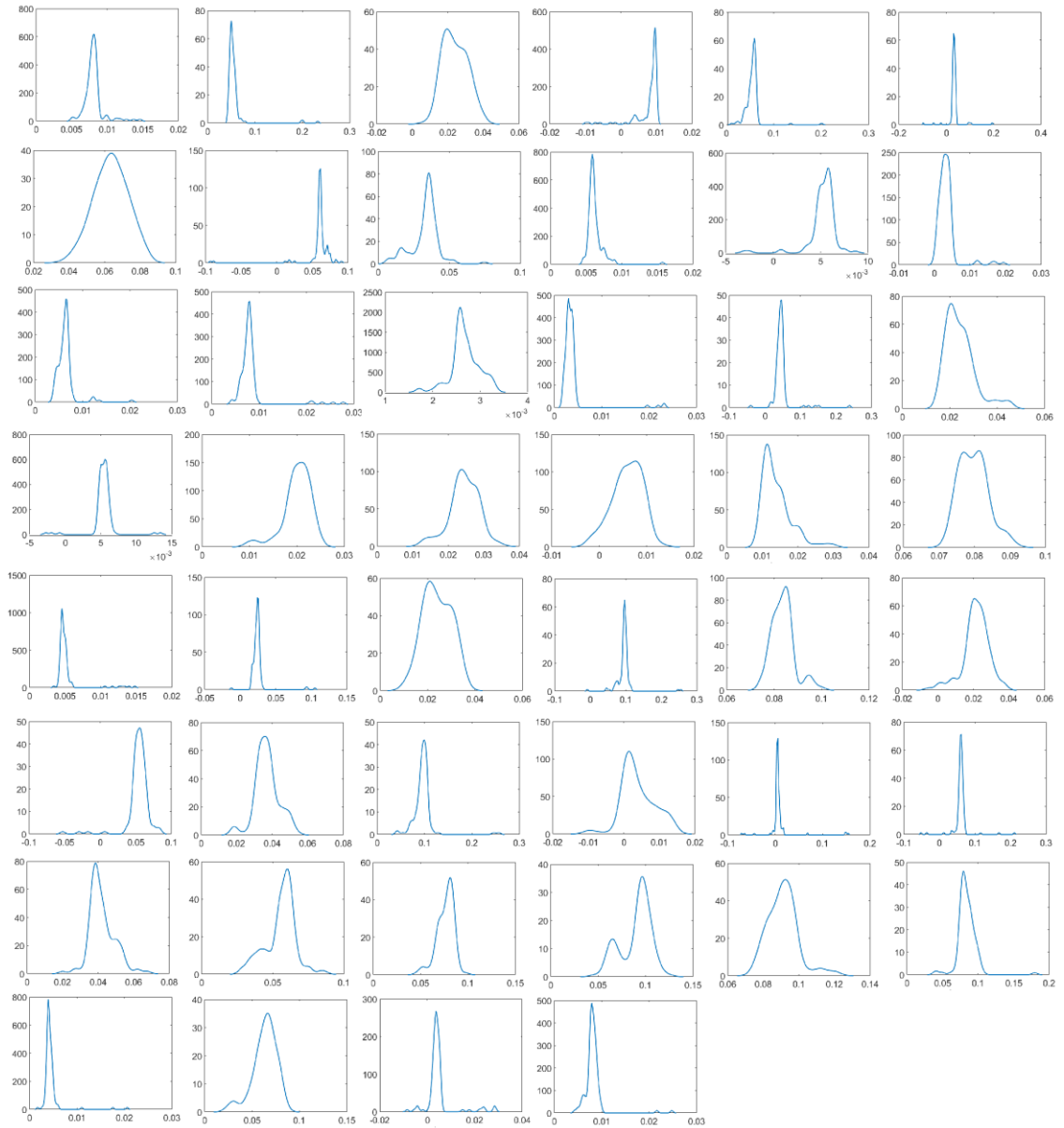


Figure 22. Probability density estimates of the spatial averages of *divWSS* values taken during the cardiac cycle for all the 46 carotid bifurcation models

#### 4.6 Co-localization analysis

To compare the distributions of the new haemodynamic descriptors based on wall shear stress divergence to the arrangements of established haemodynamic wall parameters on the luminal surface of the carotid bifurcation models, in this work

it was used a methodology that is analogous to the procedure employed in [Gallo *et al.* 2016]. More in detail, starting from the lumen geometries of the forty-six carotid bifurcations reconstructed in VMTK by [Gallo *et al.* 2015], the centerlines of the vessels were generated in VMTK (Figure 23).

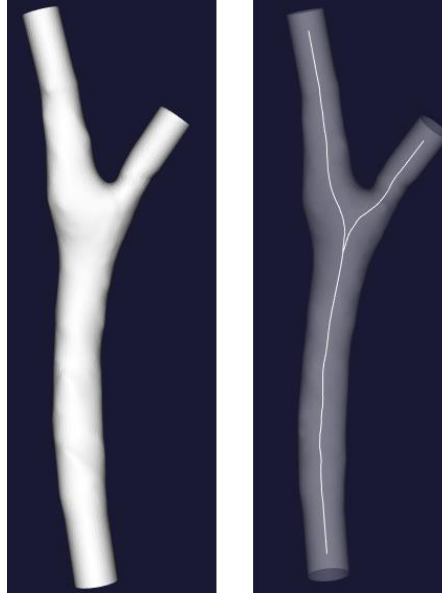


Figure 23. Example of generation of the centerline of a vessel in VMTK

Then, to delimit the bifurcation regions, that are the areas of interest with regard to atherosclerosis appearance, and to remove the flow extensions, each model was cut at sections located at 3, 5 and 2 maximally inscribed spheres radii from the bifurcation along the Common Carotid Artery, Internal Carotid Artery and External Carotid Artery, respectively (Sections CCA3, ICA5 and ECA2, Figure 24).

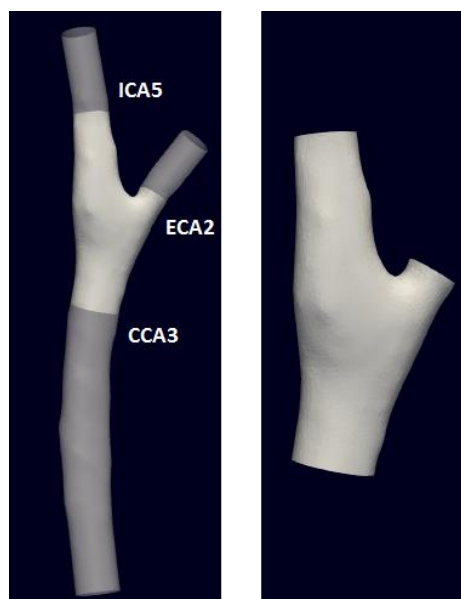


Figure 24. Example of cut of a bifurcation region along the sections CCA3, ICA5 and ECA2

The distributions of seven established haemodynamic wall parameters (TAWSS, OSI, RRT, CFI,  $WSS_{ax}$  and transWSS computed in a work by [Gallo et al. 2016] and WSST computed in this work hypothesizing a cardiac frequency of 75 beats per minute), of three new divergence-based parameters (DivP, DivN and ODI) and of the values taken by the counter were projected onto the luminal surfaces of the bifurcation regions that were isolated from the entire vessels as described above. For all the listed descriptors, threshold values were computed. Specifically, being disturbed flow regions associated with low TAWSS values, high OSI, RRT, transWSS, WSST and CFI values, and negative  $WSS_{ax}$  values, the threshold for TAWSS was the 20<sup>th</sup> percentile value, computed as the value of TAWSS under which the 20% of the merged surfaces of all the cut models was exposed to, whereas the 80<sup>th</sup> percentile values, under which the 80% of the overall cut surfaces were exposed to, were computed for OSI, RRT, CFI, transWSS and WSST, the zero value was taken as the  $WSS_{ax}$  threshold value instead. As regards the divergence-based haemodynamic wall parameters, for DivN and DivP the 20<sup>th</sup> and the 80<sup>th</sup> percentile values of  $\overline{divWSS}$  were considered as the threshold values respectively, whereas the 80<sup>th</sup> percentile value was taken as ODI threshold value. Lastly, for the counter it was computed the 80<sup>th</sup> percentile value.

To each node  $n$  of the models was associated an area  $A_n$  that was computed as one third of the summation of surface areas of all the  $t$  triangles that converged at that node:

$$A_n = \frac{1}{3} \sum_{m=1}^t A(m) \quad \text{Eq. 46}$$

The total area of the luminal surface of the bifurcation was calculated as the sum of the areas assigned to all the nodes of the model. Then, in order to quantify the disturbed flow, the relative surface areas, denoted respectively with the names TAWSS20,  $WSS_{ax\_0}$ , OSI80, RRT80, CFI80, transWSS80, WSST80, DivP80, DivN20, ODI80 and Counter80 were computed for every carotid bifurcation. These relative surface areas were obtained as the ratios between the surface areas that were exposed to TAWSS,  $WSS_{ax}$  and DivN below, OSI, RRT, CFI, transWSS, WSST, DivP, ODI and Counter above their respective threshold values and the total area of the bifurcation.

The analysis of the co-localization of new divergence-based parameters with the established haemodynamic descriptors in the carotid bifurcations was performed through the evaluation of the similarity indices, as described in [Gallo et al. 2016]. The Similarity Index (SI) quantifies the spatial overlapping of the surface areas (SAs) exposed to DivP and ODI above and DivN below their threshold values respectively with the surface areas that are subject to TAWSS and  $WSS_{ax}$  below, OSI, RRT, CFI and transWSS above the respective threshold values.

The Similarity Index is computed among two haemodynamic parameters  $i$  and  $j$ , as described by the following equation:

$$SI_{ij} = \frac{2(SA_i \cap SA_j)}{SA_i + SA_j} \quad \text{Eq. 47}$$

where  $A_i$  and  $A_j$  are the relative surface areas exposed to the  $i$ -th and the  $j$ -th descriptors above or below their threshold values, respectively.

$SI_{ij}$  can take any value between zero and one.  $SI_{ij}$  is equal to zero when the two surface areas are not spatially overlapped, whereas it takes a value of one if the surface areas  $A_i$  and  $A_j$  are perfectly overlapped and the respective descriptors are equivalent.

The distribution of the similarity indices was characterized in terms of median (Me) and median absolute deviation (Mad).

#### 4.7 Sensitivity analysis

A sensitivity analysis was performed on a carotid bifurcation model to verify if there was advisable to refine the grid to reduce the uncertainty in the evaluation of the wall shear stress divergence, seeing that it is a second order derivative of velocity. Utilizing the ANSYS ICEM CFD software, two tetrahedral meshes containing about 4,000,000 and 8,000,000 elements respectively were obtained (the CCA sections for both the meshes are depicted in Figure 25). The maximum dimension of the tetrahedral elements was controlled in order to realize the grids. The maximum and minimum dimensions of the elements of the obtained meshes are listed in Table 1.

Mesh	4,013,986 elements	8,059,166 elements
Maximum dimension (m)	$2.253 * 10^{-4}$	$1.782 * 10^{-4}$
Minimum dimension (m)	$2.2 * 10^{-5}$	$1.74 * 10^{-5}$

Table 1. Maximum and minimum dimensions of the elements of the grids realized in sensitivity analysis

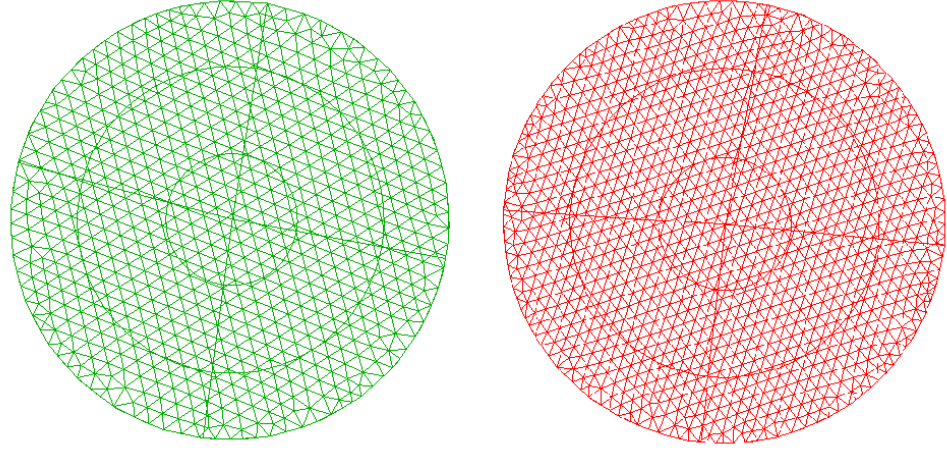


Figure 25. CCA section in the 4 million elements mesh (left) and in the 8 million elements mesh (right).

The 4 and 8 million elements grids were used to perform two identical steady state fluid dynamics simulations in ANSYS FLUENT. In the Computational Fluid Dynamics simulation, the blood was considered a Newtonian fluid characterized by a density value of  $1060 \text{ kg/m}^3$  and a constant viscosity of  $0.0035 \text{ kg/m}\cdot\text{s}$ . At the inlet (Common Carotid Artery CCA) it was imposed a constant velocity of magnitude  $0.26 \text{ m/s}$ , obtained as the ratio between the time-averaged mean flow rate in the CCA measured by Marshall et al. in healthy volunteers ( $6.16 \times 10^{-6} \text{ m}^3/\text{s}$ ) [Marshall et al. 2004] and the cross-sectional area of the CCA of the considered carotid ( $2.3742 \times 10^{-5} \text{ m}^2$ ). Meanwhile, at the outlets (External Carotid Artery and Internal Carotid Artery) it was imposed a reference pressure of  $0 \text{ Pa}$ . Lastly, it was considered a stationary wall.

Then, the percentage difference between WSS values obtained with the previously described meshes (Eq. 48) and the percentage difference between  $divWSS$  values extracted by using the 4 and 8 million elements grids (Eq. 49) were computed as shown below:

$$\frac{\left| \left\| \frac{WSS_{4m \text{ interp}}}{\max(WSS_{4m \text{ interp}})} \right\|_2 - \left\| \frac{WSS_{8m}}{\max(WSS_{8m})} \right\|_2 \right|}{\left\| \frac{WSS_{8m}}{\max(WSS_{8m})} \right\|_2} = 0.164 = 16.4\% \quad \text{Eq. 48}$$

$$\frac{\left| \left\| \frac{divWSS_{4m \text{ interp}}}{\max(divWSS_{4m \text{ interp}})} \right\|_2 - \left\| \frac{divWSS_{8m}}{\max(divWSS_{8m})} \right\|_2 \right|}{\left\| \frac{divWSS_{8m}}{\max(divWSS_{8m})} \right\|_2} = 0.178 = 17.8\% \quad \text{Eq. 49}$$

Where  $WSS_{4m}$  and  $WSS_{8m}$  are the WSS values obtained with the 4 and 8 million elements grid, respectively. Analogously,  $divWSS_{4m}$  and  $divWSS_{8m}$  are the WSS

divergence values for the above-mentioned grids. The subscript “*interp*” indicates that  $WSS_{4m}$  was interpolated at the nodes of the 8 million mesh.

Therefore, the employ of a 4 million elements mesh entails a percentage error of 16.4% in the computation of the WSS and 17.8% in the calculation of the *divWSS*, compared to the values obtained with a mesh containing 8 million elements.

The sensitivity analysis showed that the number of the elements constituting the mesh doesn’t strongly influence the output. Moreover, the employ of a more refined mesh adds complexity to the computational analysis. So, the 4 million elements grid was considered accurate enough for the aims of the present study.

## Chapter 5. Results

The distributions of the considered haemodynamic wall parameters on the bifurcation regions of the forty-six carotid models are reported in Figures from 26 to 35. As expected, low TAWSS, high OSI and high RRT values are predominantly located around the outer walls of the bifurcation, and especially at the carotid bulb (as shown in Figures 26, 27 and 28, respectively), where flow separation and blood recirculation occur.

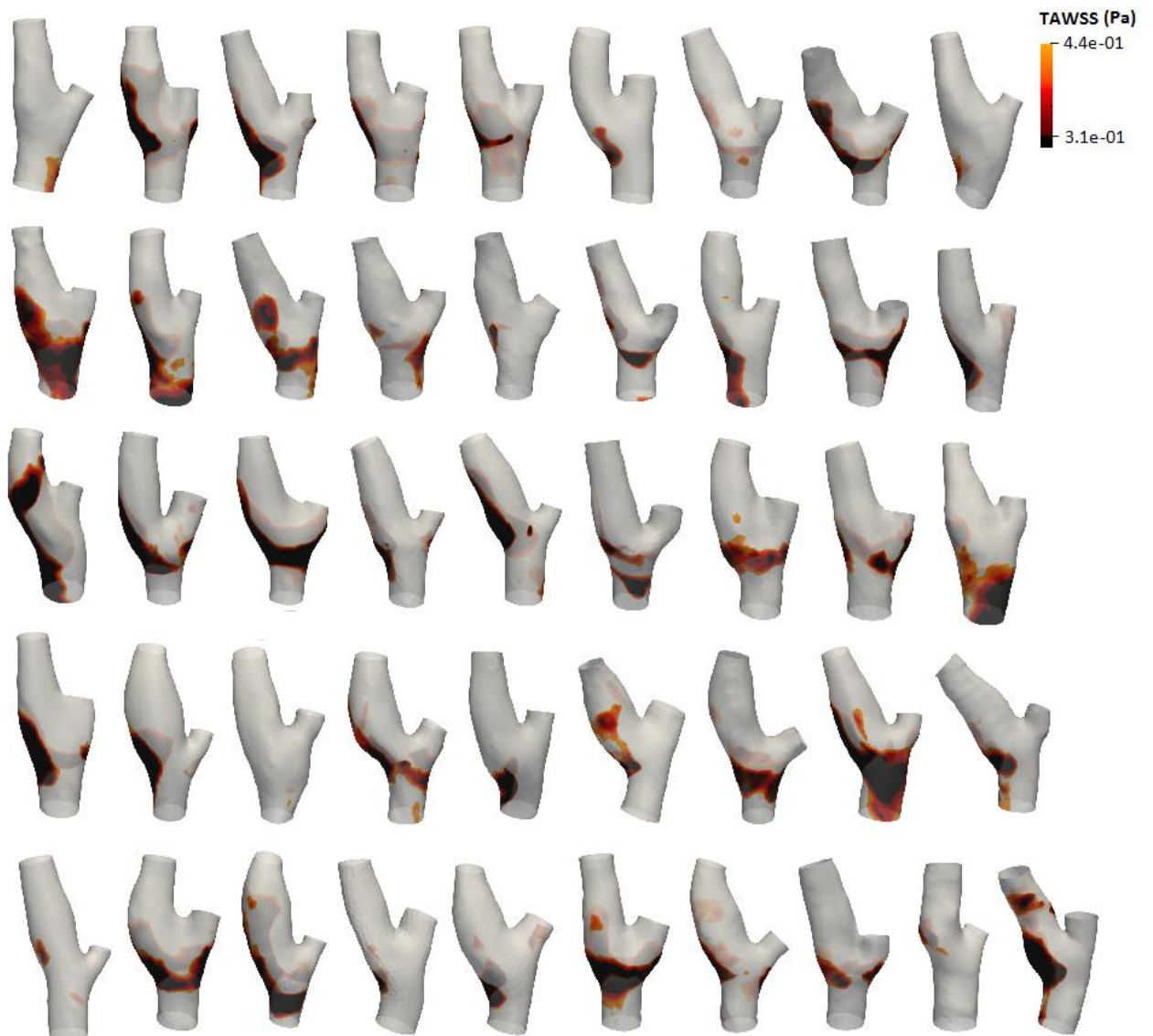


Figure 26. Exposure to low TAWSS for the 46 carotid bifurcation models. The values reported in the legend correspond to 20<sup>th</sup> and 10<sup>th</sup> percentile values.

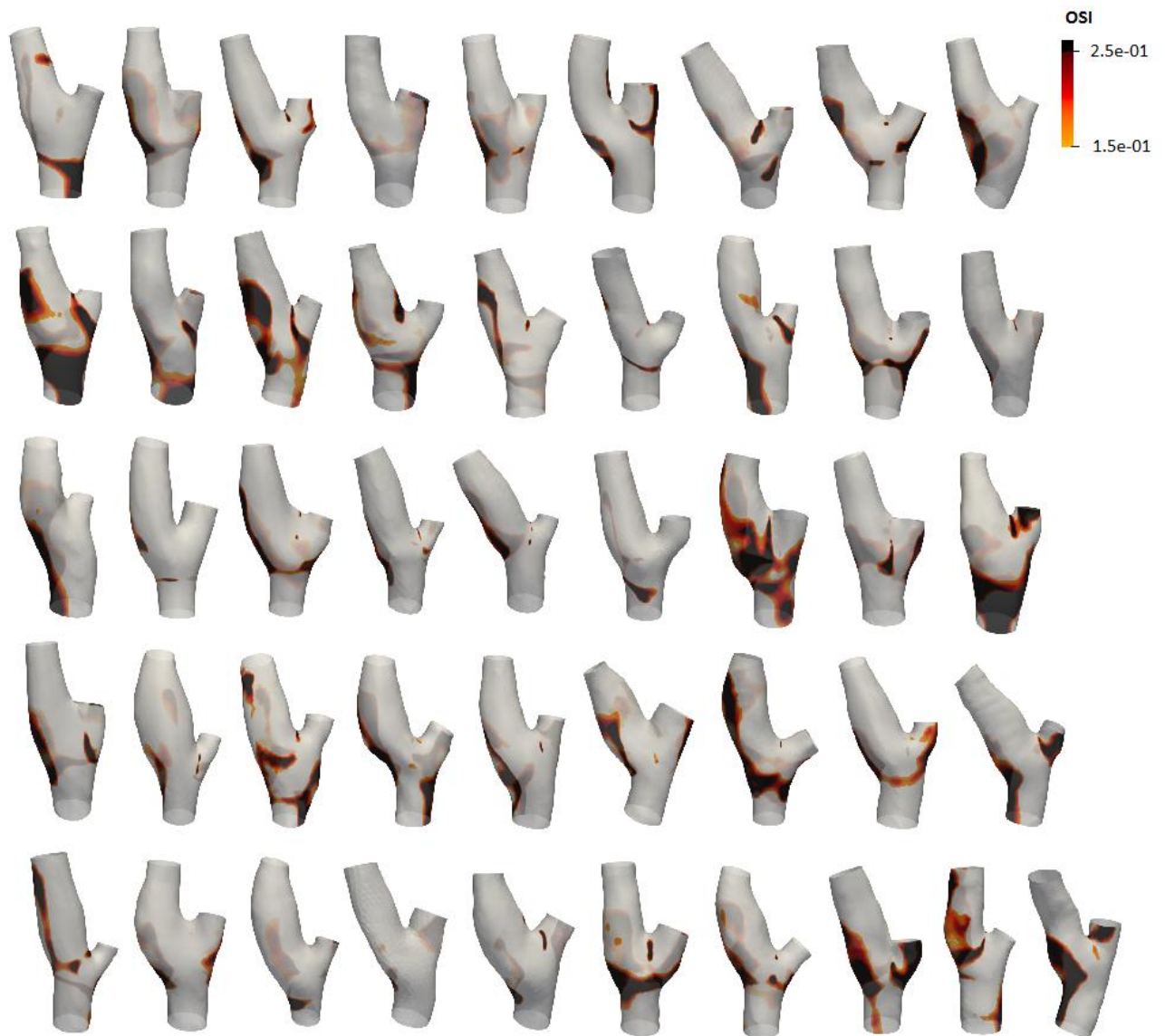


Figure 27. Exposure to high OSI for the 46 carotid bifurcation models. The values reported in the legend correspond to 90<sup>th</sup> and 80<sup>th</sup> percentile values.

Regions on the luminal surface where TAWSS values are low (Figure 26) are characterized by slow blood flow, whereas high OSI values (Figure 27) are localized at regions where the WSS oscillates. RRT combines this information in a single parameter, so the distribution of high RRT (Figure 28) is similar to those that refer to SAs exposed to low TAWSS and high OSI values, and it highlights regions of high near-wall atherogenic particles residence time.

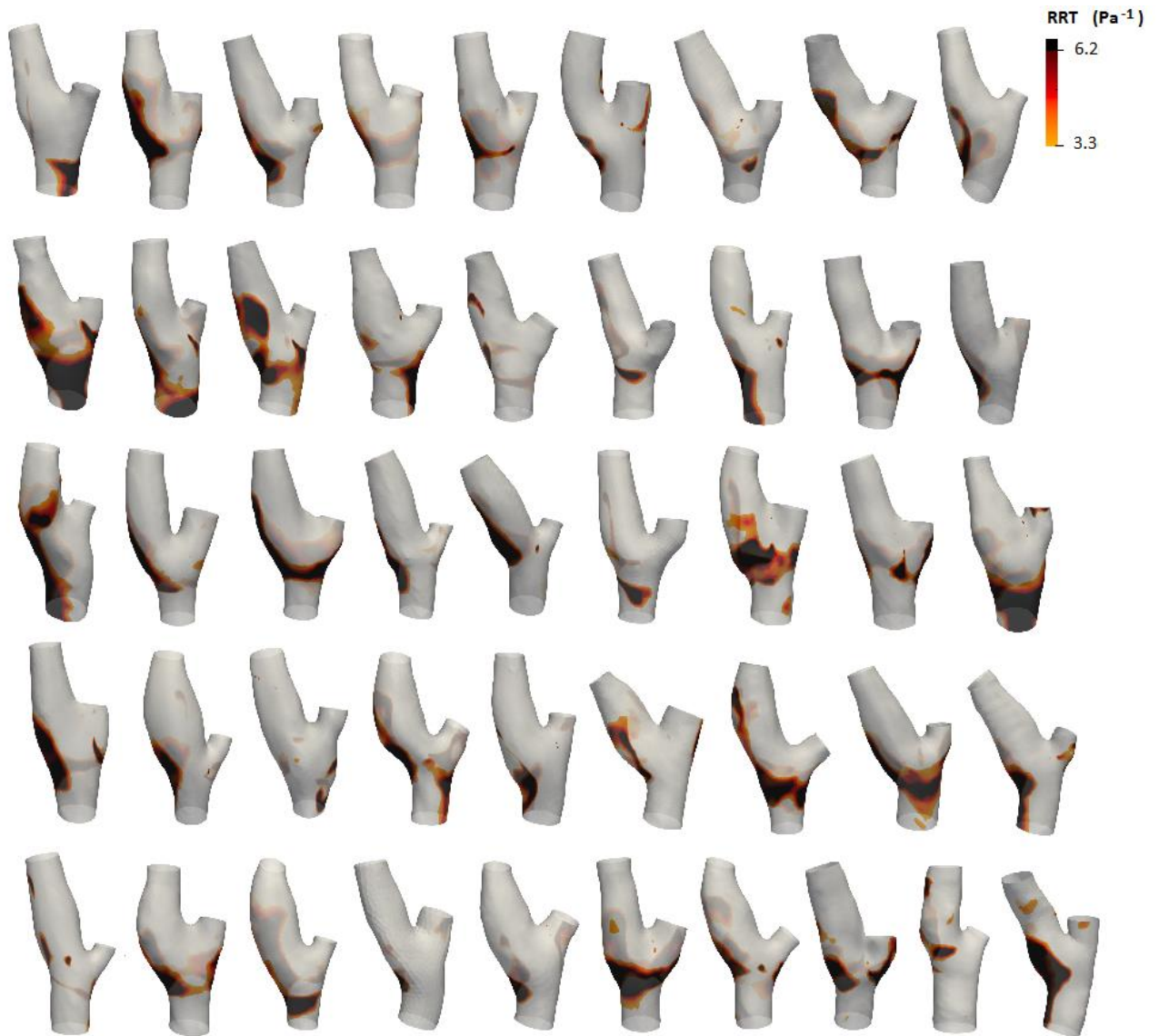


Figure 28. Exposure to high RRT for the 46 carotid bifurcation models. The values reported in the legend correspond to 90<sup>th</sup> and 80<sup>th</sup> percentile values.

The regions exposed to low TAWSS, high OSI and consequently to high RRT values are generally recognized as the most common sites for atherosclerotic plaque development in carotid bifurcation. By contrast, high transWSS values are localized at the flow divider, as shown in Figure 29, that is normally a plaque-free site. The extent of the region subject to high transWSS values is strongly dependent on vessel geometry, that influence the amount of flow that is orthogonal to the mean WSS direction.

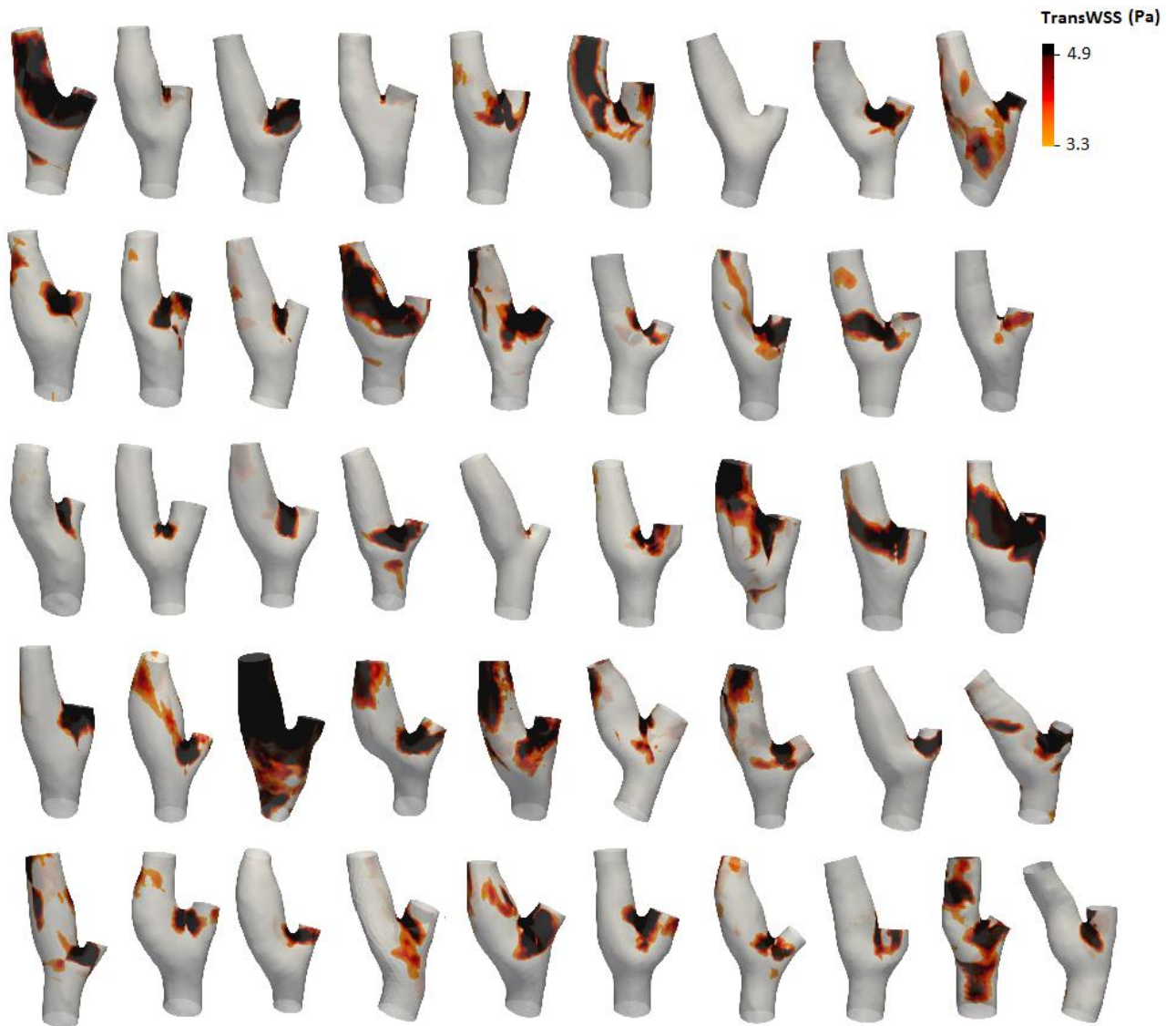


Figure 29. Exposure to high TransWSS for the 46 carotid bifurcation models. The values reported in the legend correspond to 90<sup>th</sup> and 80<sup>th</sup> percentile values.

The distributions of SAs exposed to negative  $WSS_{ax}$  are reported in Figure 30. Negative values of this parameter point out regions of flow reversal, that are localized both at the carotid bulb and at the ECA entrance.

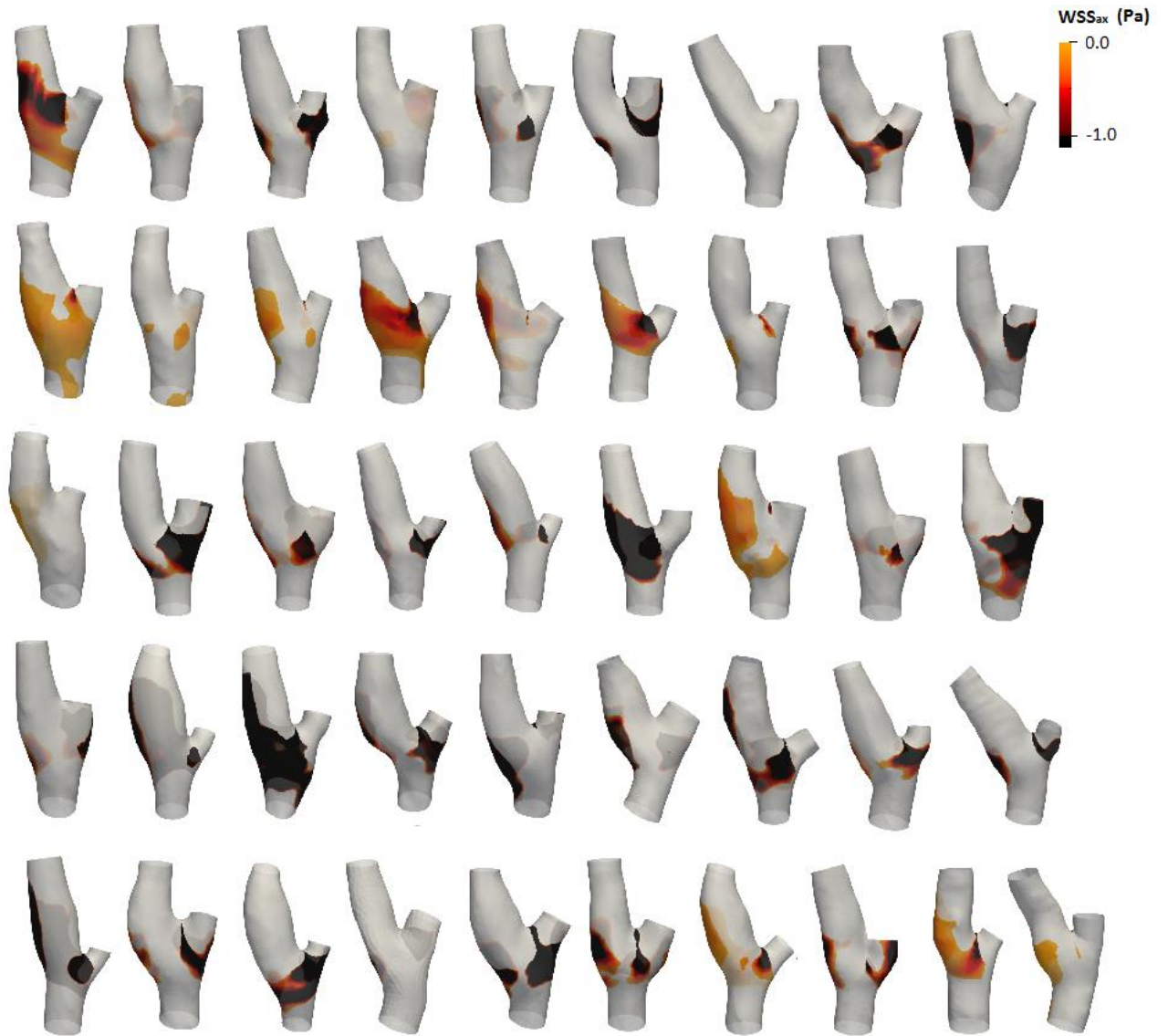


Figure 30. Exposure to negative  $WSS_{ax}$  for the 46 carotid bifurcation models.

In accordance with its definition, CFI assumes high values where both TAWSS and transWSS are low, turning out low TAWSS and high transWSS values to be never co-localized on the surface of the models that were examined in this work. High CFI values indicate regions where blood stagnation occur (Figure 31).

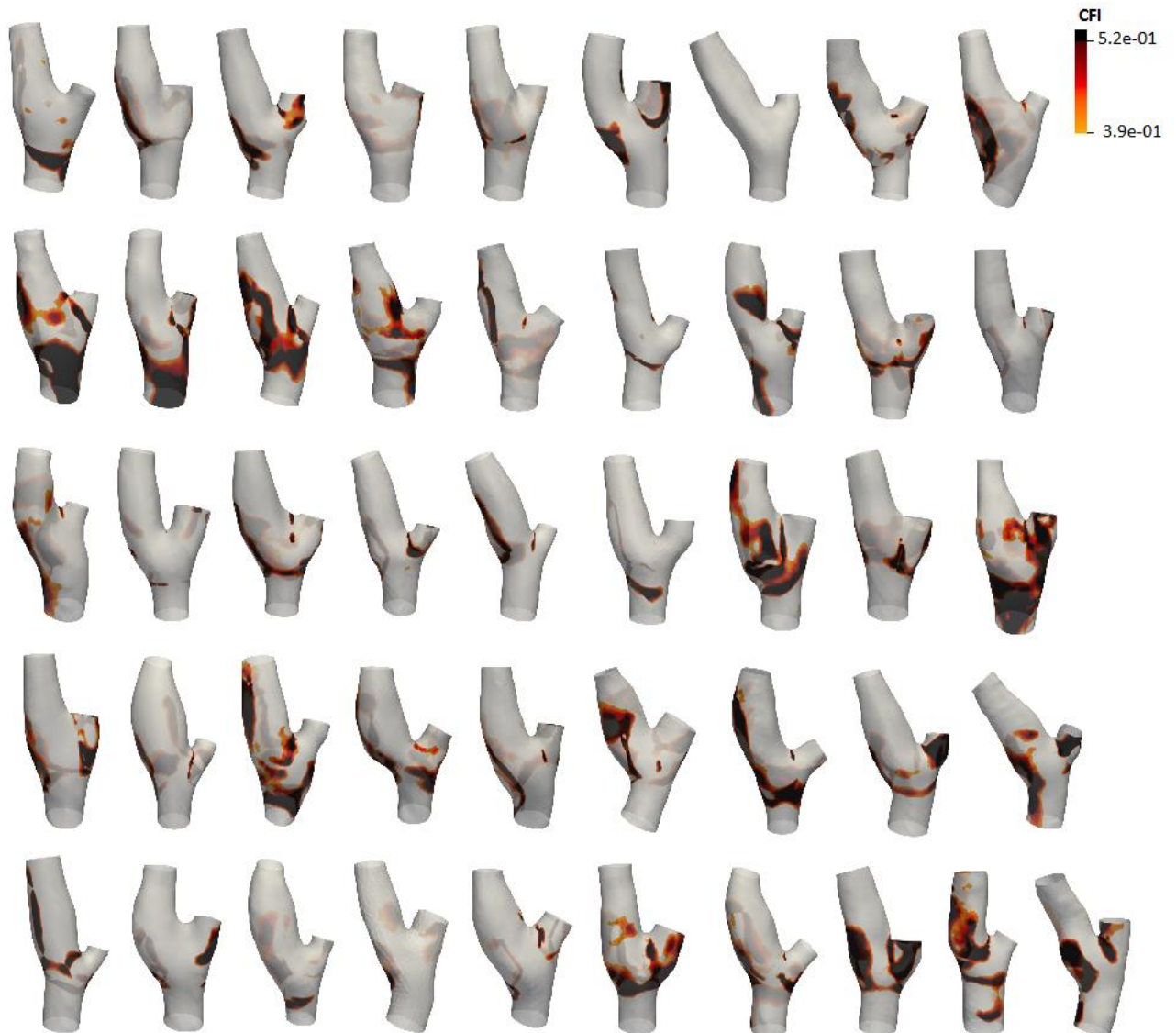


Figure 31. Exposure to high CFI for the 46 carotid bifurcation models. The values reported in the legend correspond to 90<sup>th</sup> and 80<sup>th</sup> percentile values.

The distribution of high WSS temporal gradient values on the bifurcation regions is shown in Figure 32. High WSST values are concentrated, though with variable extent, around the carotid apex, conforming to the results obtained in a work on anatomic realistic carotid bifurcation geometries by [Lee et al. 2009], and at the inner walls of ICA and ECA.

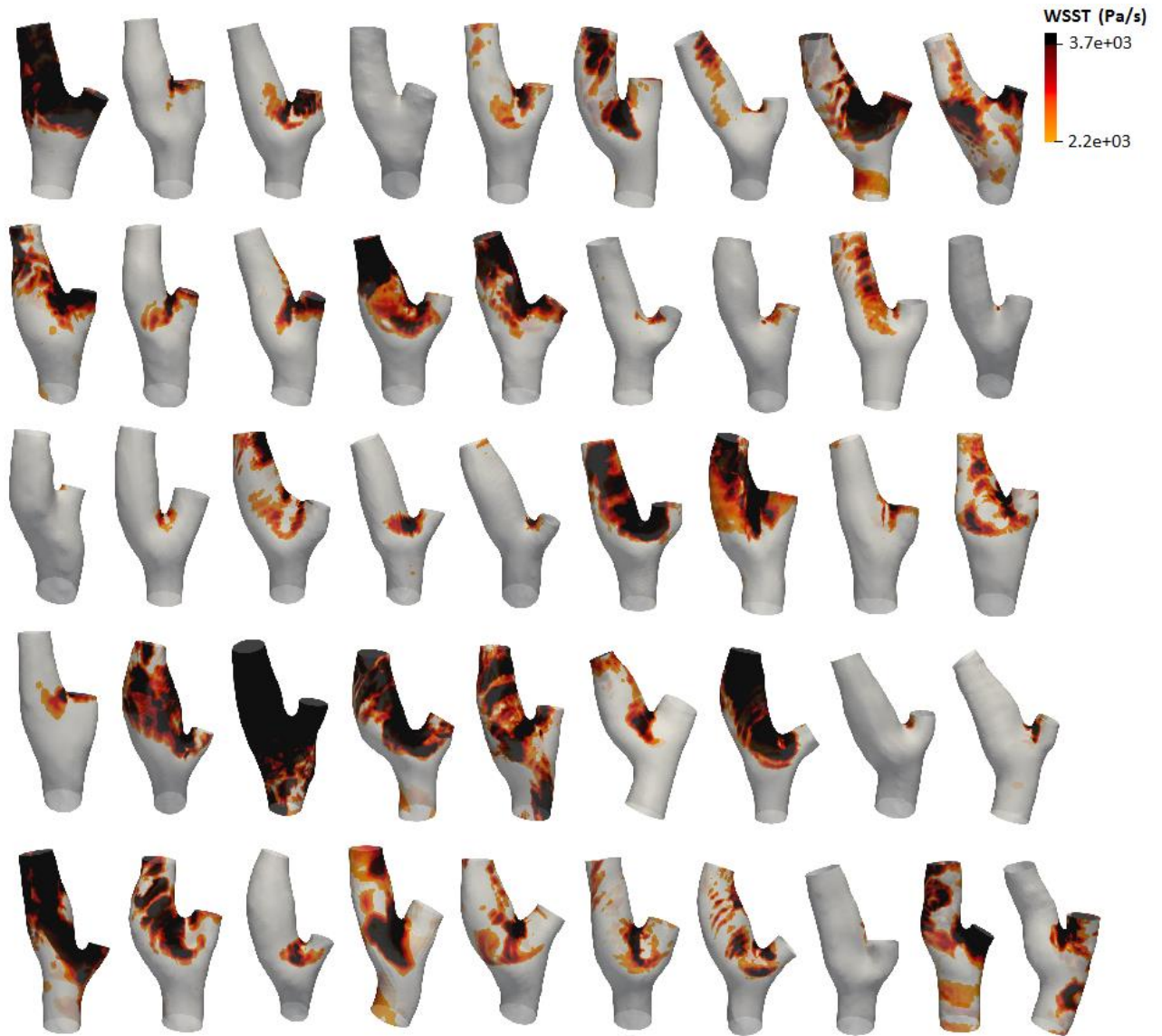


Figure 32. Exposure to high WSST values for the 46 carotid bifurcation models. The values reported in the legend correspond to 90<sup>th</sup> and 80<sup>th</sup> percentile values.

Lastly, the spatial distributions of the novel haemodynamic wall parameters based on wall shear stress divergence are depicted in Figures 33, 34 and 35. Regions exposed to low DivN values are subject to strong negative WSS divergence values on average, that correspond to a WSS field directed toward the inside, here referred as sink configuration. Such stress results in a compressive force on these portions of the wall.

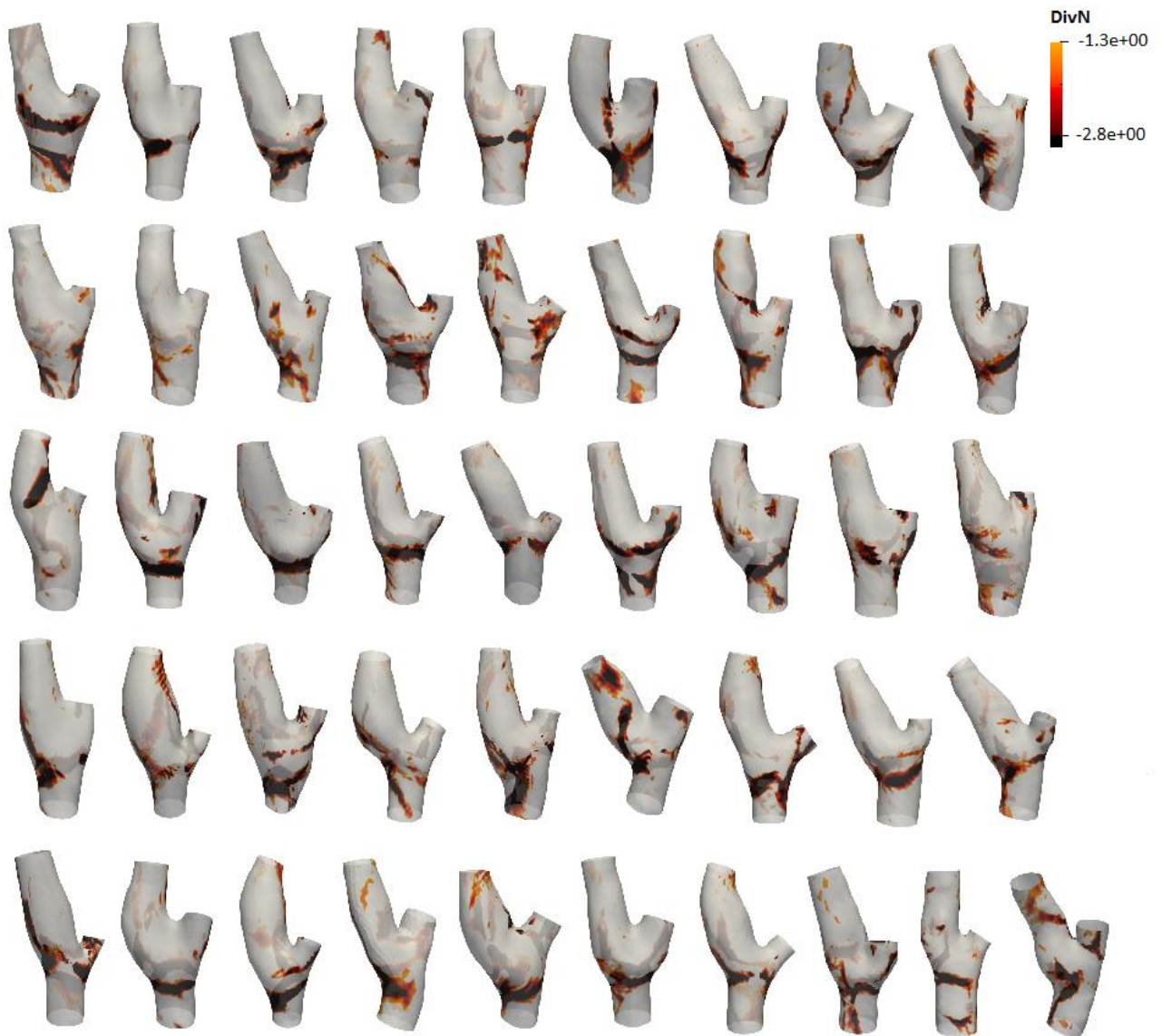


Figure 33. Exposure to low DivN for the 46 carotid bifurcation models. The values reported in the legend correspond to the 20<sup>th</sup> and the 10<sup>th</sup> percentile values of  $\overline{divWSS}$ .

On the contrary, high DivP zones on the vessel surface are exposed to wall shear stress that points outwards, assuming a source configuration and causing a stretching effect on these vessel regions.

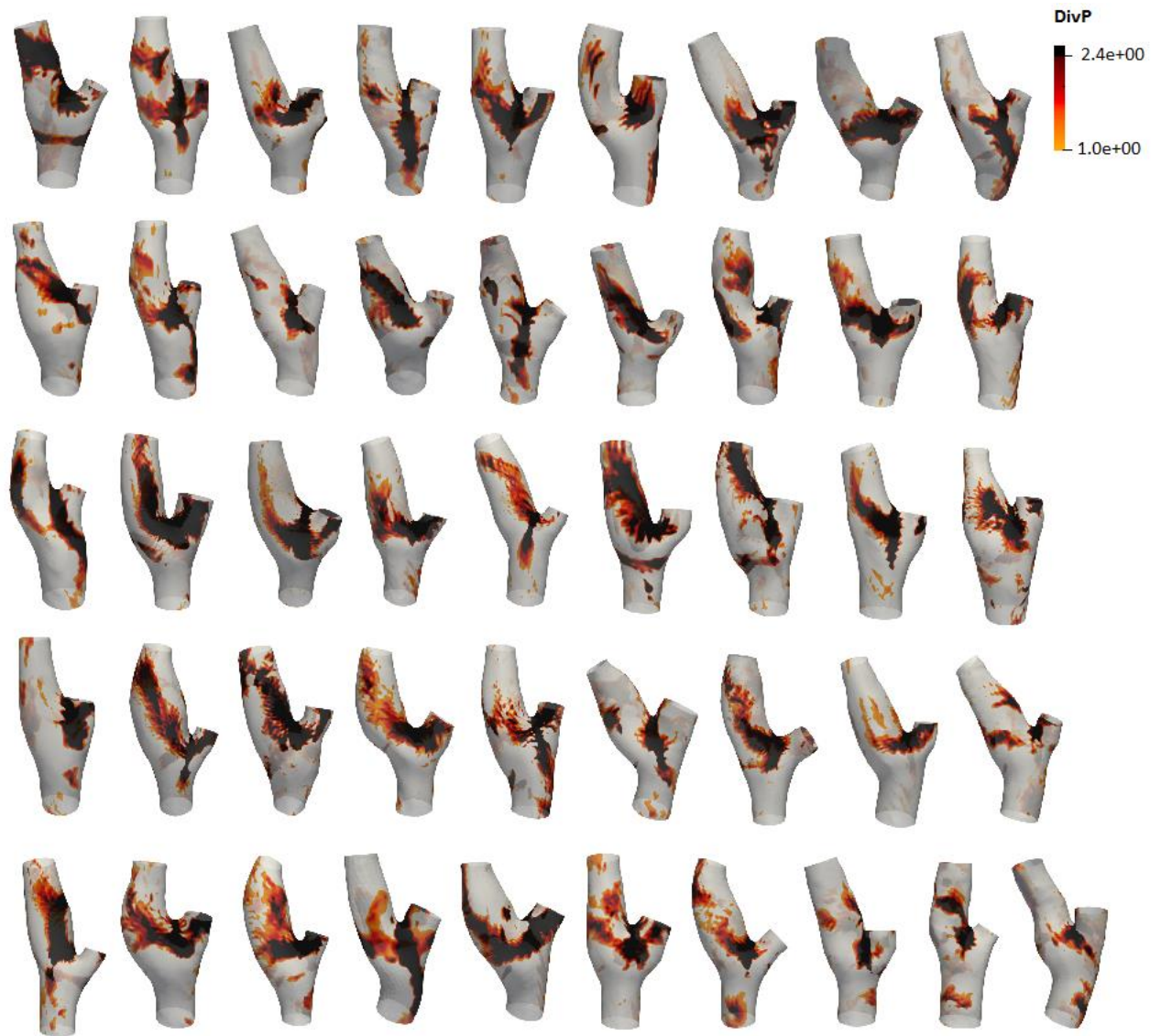


Figure 34. Exposure to high DivP for the 46 carotid bifurcation models. The values reported in the legend correspond to the 90<sup>th</sup> and the 80<sup>th</sup> percentile values of  $\overline{divWSS}$ .

ODI points out large directional changes of WSS between source and sink arrangements. Regions on the bifurcation walls characterized by high ODI values (Figure 35) are subject to alternative expansions and compressions of the endothelial layer during the cardiac cycle.

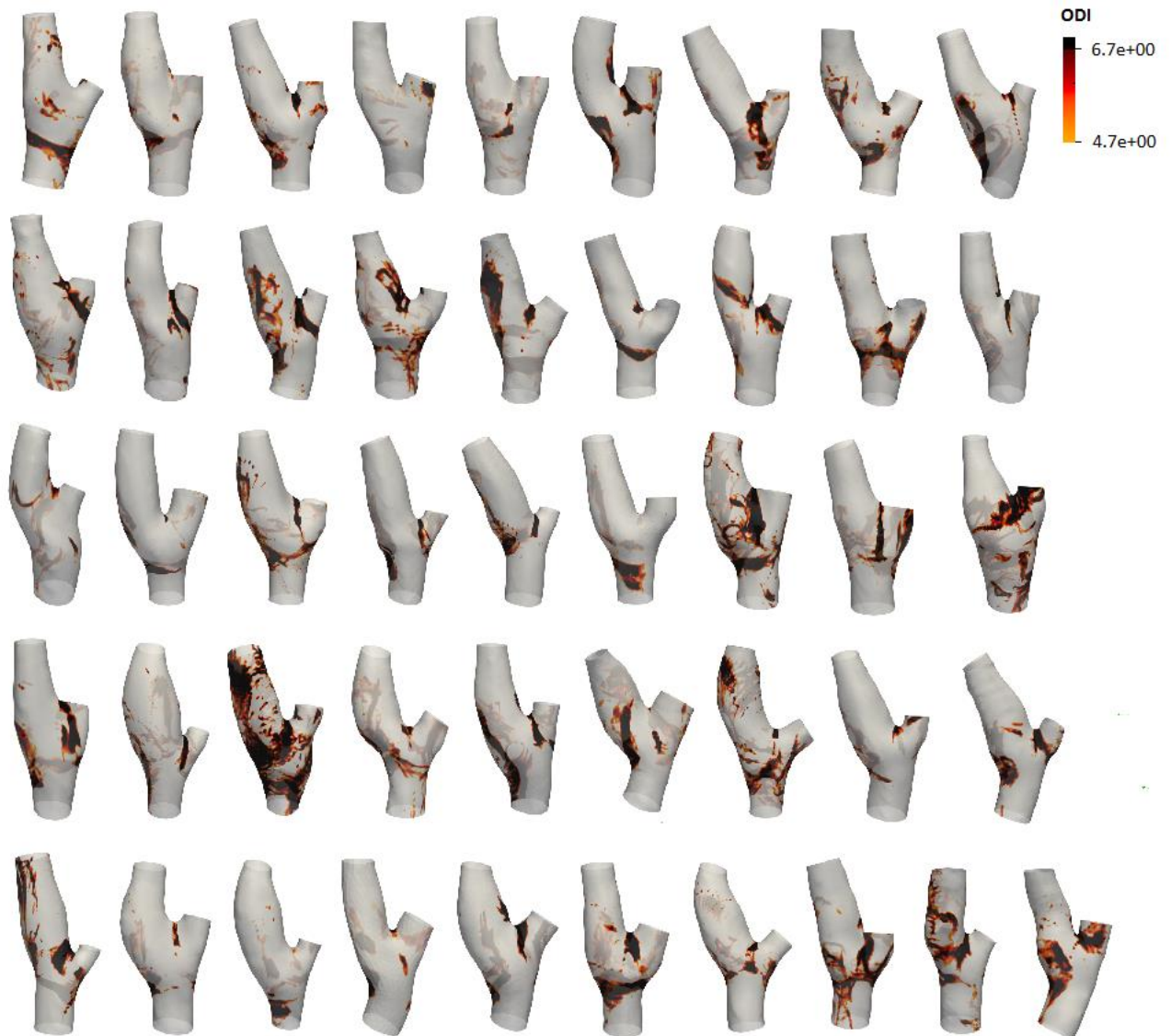


Figure 35. Exposure to high ODI for the 46 carotid bifurcation models. The values reported in the legend correspond to 90<sup>th</sup> and 80<sup>th</sup> percentile values.

On the maps in Figure 36 the surface areas on the vessel wall exposed to a large number of sign variations of  $divWSS$  during the cardiac cycle are visualized. Specifically, the coloured SAs correspond to the regions on the luminal surface of the carotid bifurcation models where the Counter takes a value greater than its 80<sup>th</sup> percentile value.

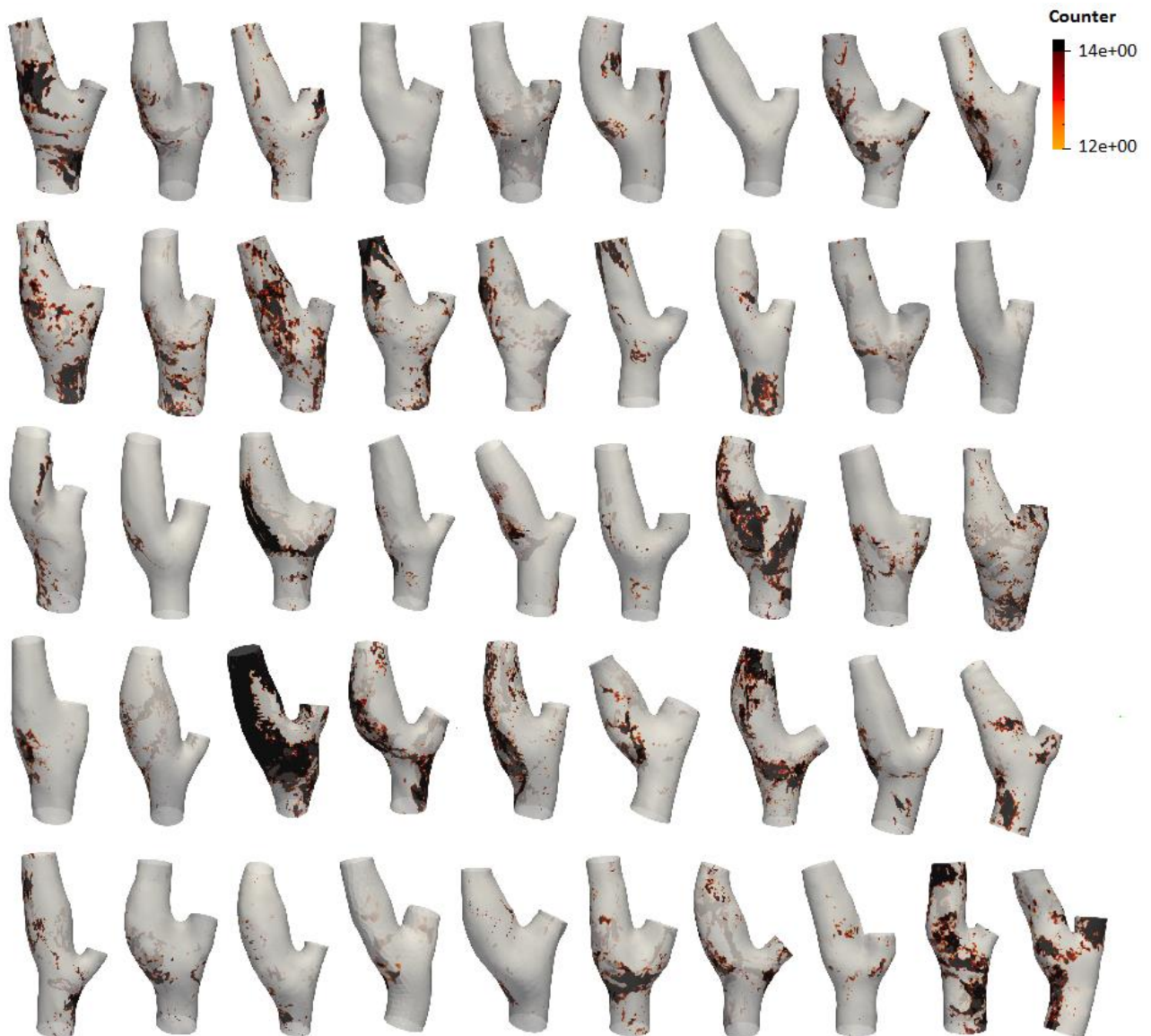


Figure 36. Exposure to high Counter values for the 46 carotid bifurcation models. The values reported in the legend correspond to 90<sup>th</sup> and 80<sup>th</sup> percentile values.

The results of the co-localization analysis are depicted through the similarity index distributions in terms of median (Me) and median absolute deviation (Mad). The similarity index was computed between each new WSS divergence-based descriptor and every pre-existing haemodynamic wall parameter, individually.

The distributions of similarity indices for DivN displayed in Figure 37 show that this parameter is moderately correlated with low TAWSS (Me=0.433), indicating that a WSS field pointing inwards on average during the overall cardiac cycle results in regions of blood stagnation. Surface areas exposed to low DivN are also moderately overlapped with high OSI regions. This not outstanding result suggests that DivN can capture uniaxial flux converging toward a specific region, but it supplies additional information as compared to OSI, concerning the directionality of WSS. A moderate co-localization can be also observed between DivN and RRT, being the latter defined as a combination of TAWSS and OSI able to measure the particles near-wall residence time. These results are consistent with the work carried out by Arzani et al. in abdominal aortic aneurysms, which demonstrated that negative WSS divergence could typify flow separation. This condition implies higher near-wall concentrations of chemical species and higher residence time, promoting atherogenic processes [Arzani et al. 2017].

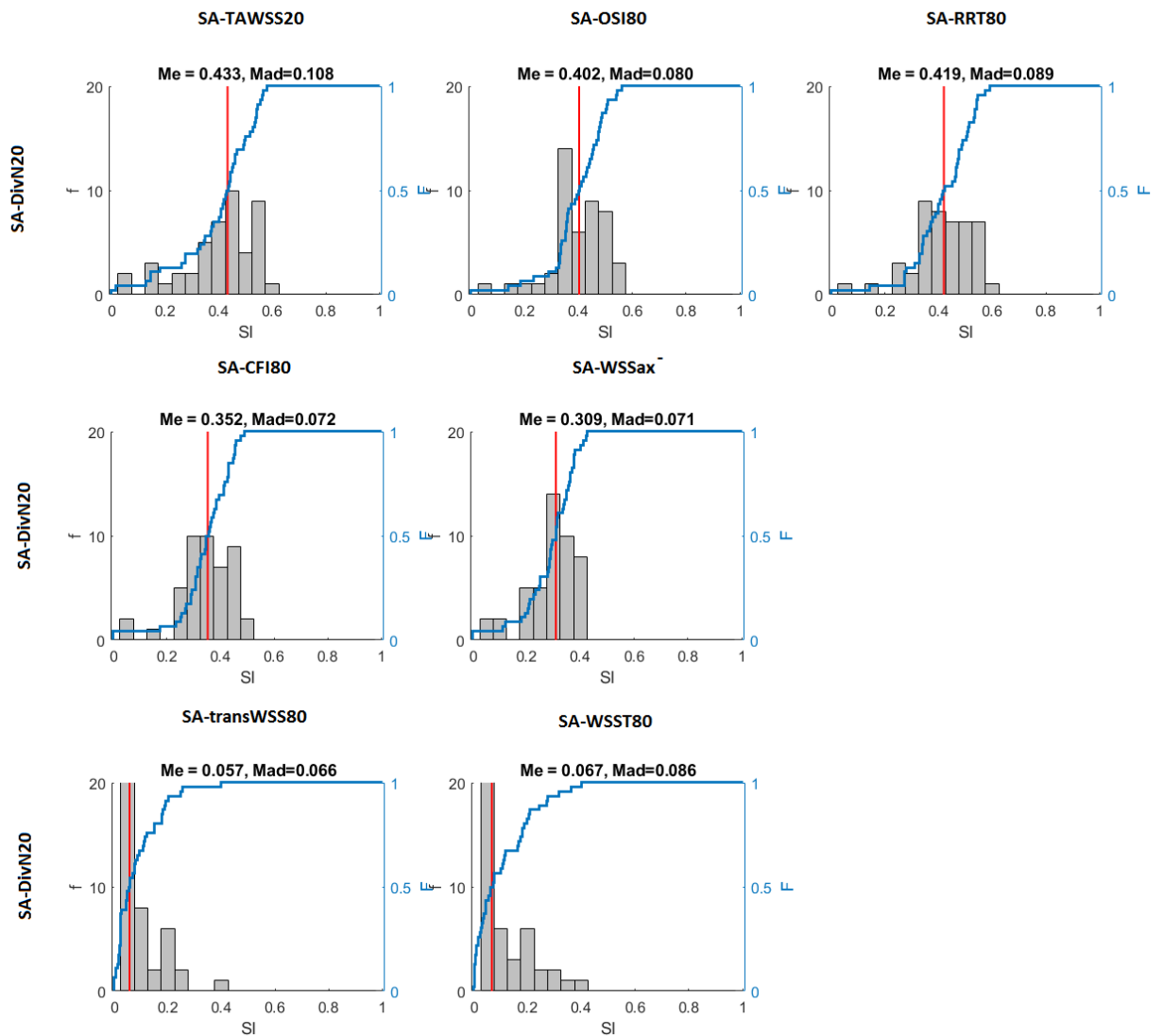


Figure 37. Distribution of SI values for the SA exposed to low DivN with the SA exposed to disturbed flow, as defined by the existing HWPs. Each bar of the histograms represents the number of cases with a certain range of SI, the blue line represents the cumulative distribution function. Me is the median, Mad is the median absolute deviation.

DivN weakly co-localizes with high CFI and negative  $WSS_{ax}$ , indicating that DivN can't capture flow reversal, and it is not correlated with transWSS and WSST. This implies that regions where the WSS component perpendicular to the mean flow direction is predominant and the WSST is high, as the bifurcation apex, are not characterized by converging WSS vectors.

On the contrary, the SAs exposed to high positive WSS divergence (Figure 38) are moderately co-localized with the regions where transWSS values are high (Me=0.403), highlighting bifurcation zones characterized by WSS that takes a source configuration. A weak co-localization can be observed between the SA exposed to high DivP values and the area where WSST is high, even though the data are highly dispersed (Mad=0.151). DivP does not show spatial overlapping with the other considered existing HWPs (Figure 38, first and second row), suggesting that the regions stressed by a source-arranged WSS field are typically concentrated around the flow divider and not at the bifurcation bulb, that is recognized as the most common atherosclerotic plaque formation site. So, positive WSSdiv values exemplify flow impingement at the carotid bifurcation, as stated by [Arzani *et al.* 2017].

The distributions of SI values for ODI (Figure 39) reveals a spatial overlapping between the SA exposed to high ODI, where the standard deviation of  $divWSS$  is high, and the area exposed to high OSI values. This co-localization, characterized by a median value of 0.568, is larger than that observed between DivN and OSI (Me=0.402) and it points out regions that experience large oscillations of uniaxial WSS between the source and sink configurations throughout the entire cardiac cycle. High ODI values are also moderately co-localized with high CFI, highlighting regions of flow reversal, with high RRT, pointing out high residence time regions, and low TAWSS values, albeit with substantial dispersion. The SAs exposed to both high ODI and low TAWSS are recirculation zones, where the WSS repeatedly changes its direction and the blood stagnates. The fact that ODI better co-localizes with OSI suggests that this new parameter could be employed in the detection of regions exposed to an oscillating WSS direction. From the absent co-localization of high ODI with high transWSS and high WSST, it emerges that the region that is mainly subject to fluctuations between tensile and compressive shear stress on the vessel wall is not the bifurcation apex, where high transWSS and high WSST values concentrate, but the carotid bulb, that is the most athero-prone region.

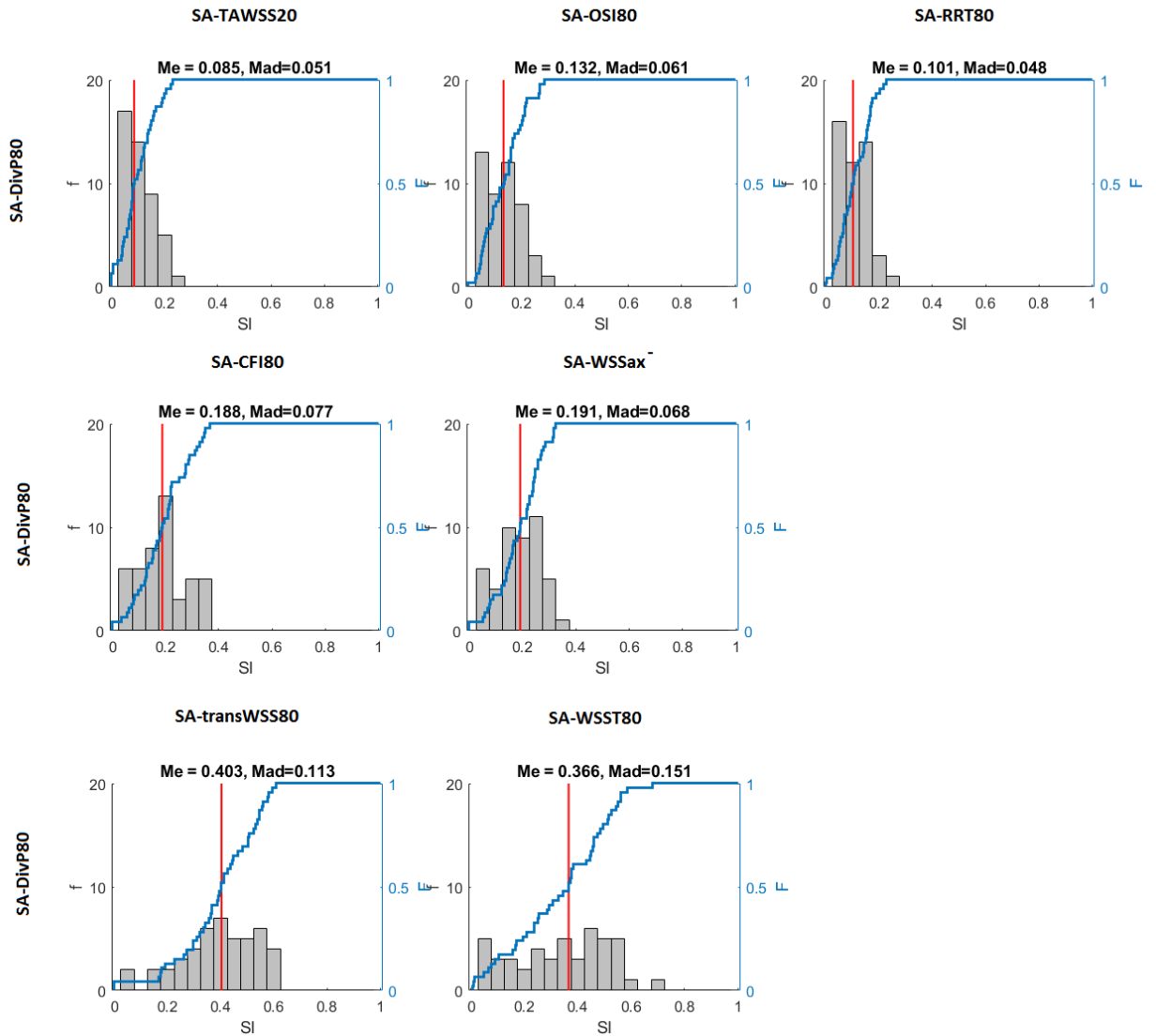


Figure 38. Distribution of SI values for the SA exposed to high DivP with the SA exposed to disturbed flow, as defined by the existing HWP. Each bar of the histograms represents the number of cases with a certain range of SI, the blue line represents the cumulative distribution function. Me is the median, Mad is the median absolute deviation.

The co-localization analysis was also performed to compare the distributions of the novel divergence-based haemodynamic parameters on the carotid bifurcation surfaces. The distributions of SI values for the SAs exposed to high ODI values with SAs that are subject to low DivN and high DivP values are shown in Figure 40. High ODI is moderately co-localized with low DivN ( $Me=0.441$ ) and it is not co-localized with high DivP ( $Me=0.138$ ). So, regions on the vessel wall that are subject to the lowest negative  $\overline{divWSS}$  values on average during the cardiac cycle are also characterized by a greater standard deviation, as compared to surface areas where  $\overline{divWSS}$  is high. This result suggests that flow separation regions, where  $\overline{divWSS}$  is negative, can be subject to highly variable blood flow and consequently to highly oscillating WSS direction between the diverging and converging arrangements. The SI value is mediocre because

ODI provides additional information in regard to DivN, concerning the variability of WSS direction. On the other hand, regions where the average *divWSS* is high have a lower standard deviation, presumably due to a steadier blood flow. Comparing the maps in Figure 35 to those in Figure 34, it can be observed that the surface areas exposed to ODI above its 80<sup>th</sup> percentile value are narrower than the SAs exposed to high DivP. So, only small areas on the region of the bifurcation apices are subject to large variations in *divWSS* value, even though *divWSS* value probably remains positive throughout the cardiac cycle.

The limitation that affects the interpretation of ODI is the fact that this parameter points out large oscillations of WSS direction between the source and sink configurations only if the distribution of *divWSS* values is nearly-normal around the zero value.

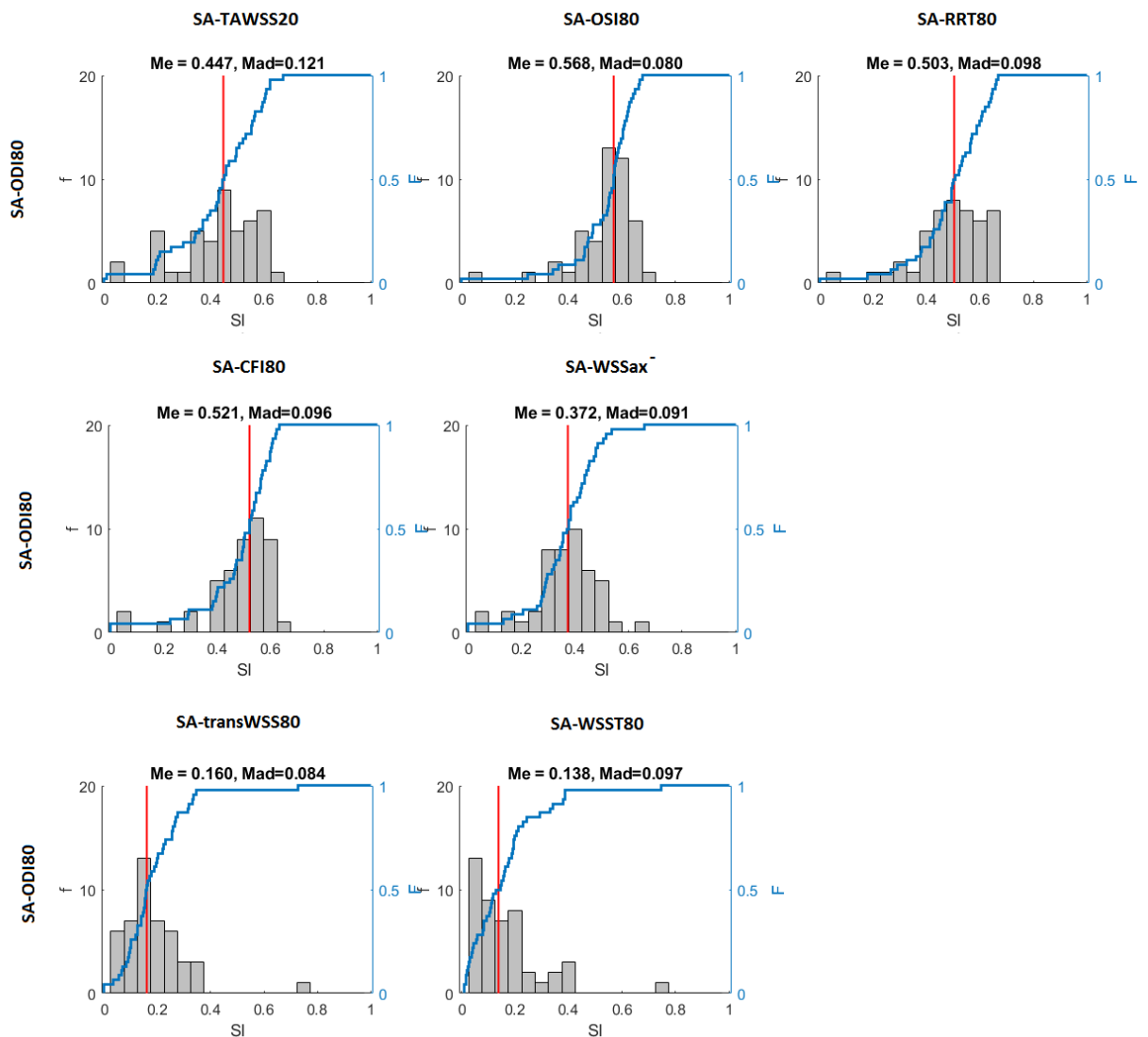


Figure 39. Distribution of SI values for the SA exposed to high ODI with the SA exposed to disturbed flow, as defined by the existing HWPs. Each bar of the histograms represents the number of cases with a certain range of SI, the blue line represents the cumulative distribution function. Me is the median, Mad is the median absolute deviation.

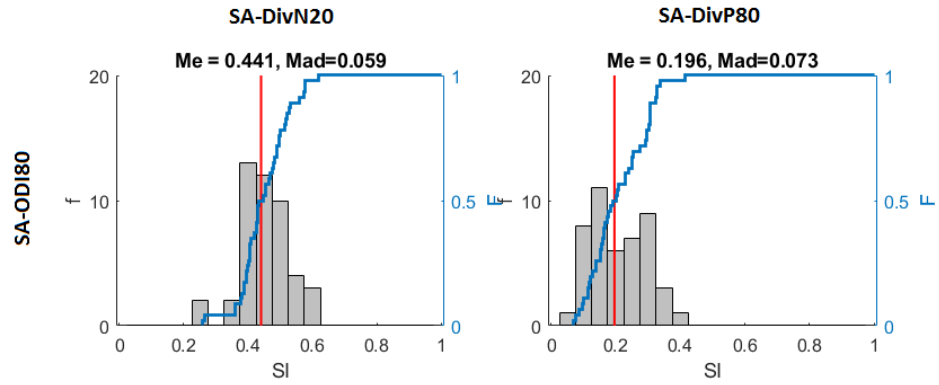


Figure 40. Distribution of SI values for the SA exposed to high ODI with the SA exposed to low DivN (left) and with the SA exposed to high DivP (right). Each bar of the histograms represents the number of cases with a certain range of SI, the blue line represents the cumulative distribution function. Me is the median, Mad is the median absolute deviation.

The co-localization analysis was also performed between SA exposed to a high number of *divWSS* consecutive sign changes, represented by high Counter values, and SA exposed to high ODI values (Figure 41).

ODI exhibited a weak co-localization with the Counter (Figure 41). This weak co-localization of SA exposed to high Counter values and SA exposed to high ODI can be explained by the fact that in the definition of the Counter the moduli of *divWSS* values were not taken into account. So, this Counter counts every sign change between two consecutive time steps regardless of the modulus change, so it counts small fluctuations of *divWSS* around the zero value as well. These small fluctuations, that correspond to low deviations from the uniformity of WSS vector field, are neglected when the 80<sup>th</sup> percentile value of ODI is computed.

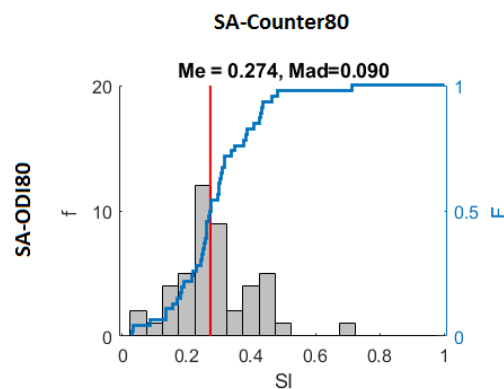


Figure 41. Distribution of SI values for the SA exposed to high Counter values with the SA exposed to high ODI. Each bar of the histogram represents the number of cases with a certain range of SI, the blue line represents the cumulative distribution function. Me is the median, Mad is the median absolute deviation.

SI values were then computed to quantify the spatial overlapping between the SA exposed to high Counter values and the SA exposed to disturbed flow, as defined by every established HWP that was considered so far. These distributions (Figure 42) follow the trend of ODI co-localization with the pre-existing HWPs, but to a lesser extent, reflecting the weak correlation observed between the Counter and ODI (Figure 41).

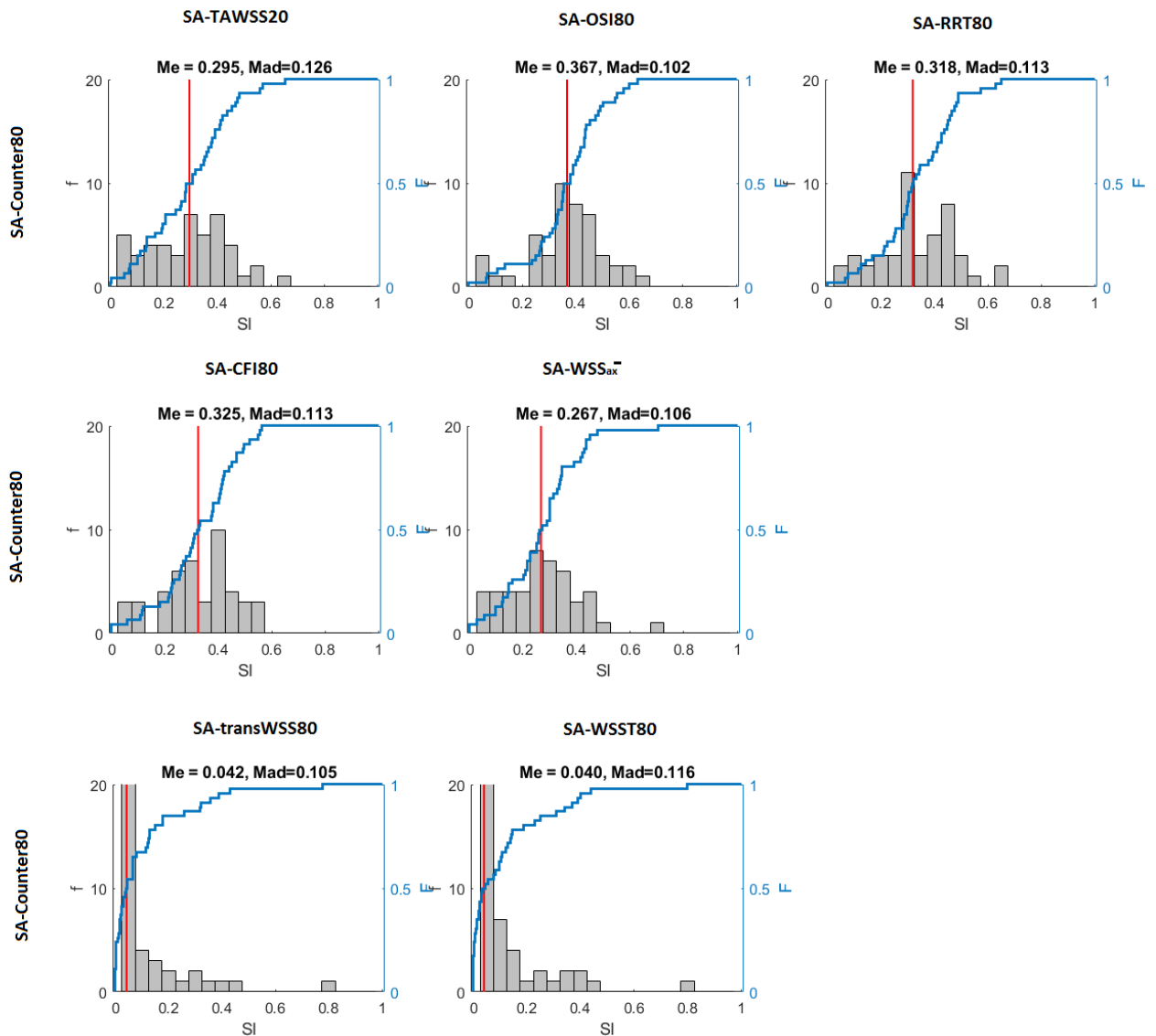


Figure 42. Distribution of SI values for the SA exposed to high Counter values with the SA exposed to disturbed flow, as defined by the existing HWPs. Each bar of the histogram represents the number of cases with a certain range of SI, the blue line represents the cumulative distribution function. Me is the median, Mad is the median absolute deviation.

To consider the sign changes of  $divWSS$  that occur during systole and during diastole separately, the cardiac cycle was divided into two parts. Considered the normal duration of cardiac phases, [10] for all the carotid bifurcation models the systolic phase

was arbitrarily considered to last from the first to the fortieth time step, while the following eighty time steps were considered to describe the diastolic phase. Then, two distinct counters, named CounterSys and CounterDia, were defined to count the number of transitions of *divWSS* between positive and negative values during the systole and the diastole, respectively. For both the counters, the 80<sup>th</sup> percentile value was taken as threshold value to visualize the distribution of high CounterSys and high CounterDia values on the surfaces of the models (Figure 43 and Figure 44, respectively) and to realize the co-localization analysis with the pre-existing HWPs.

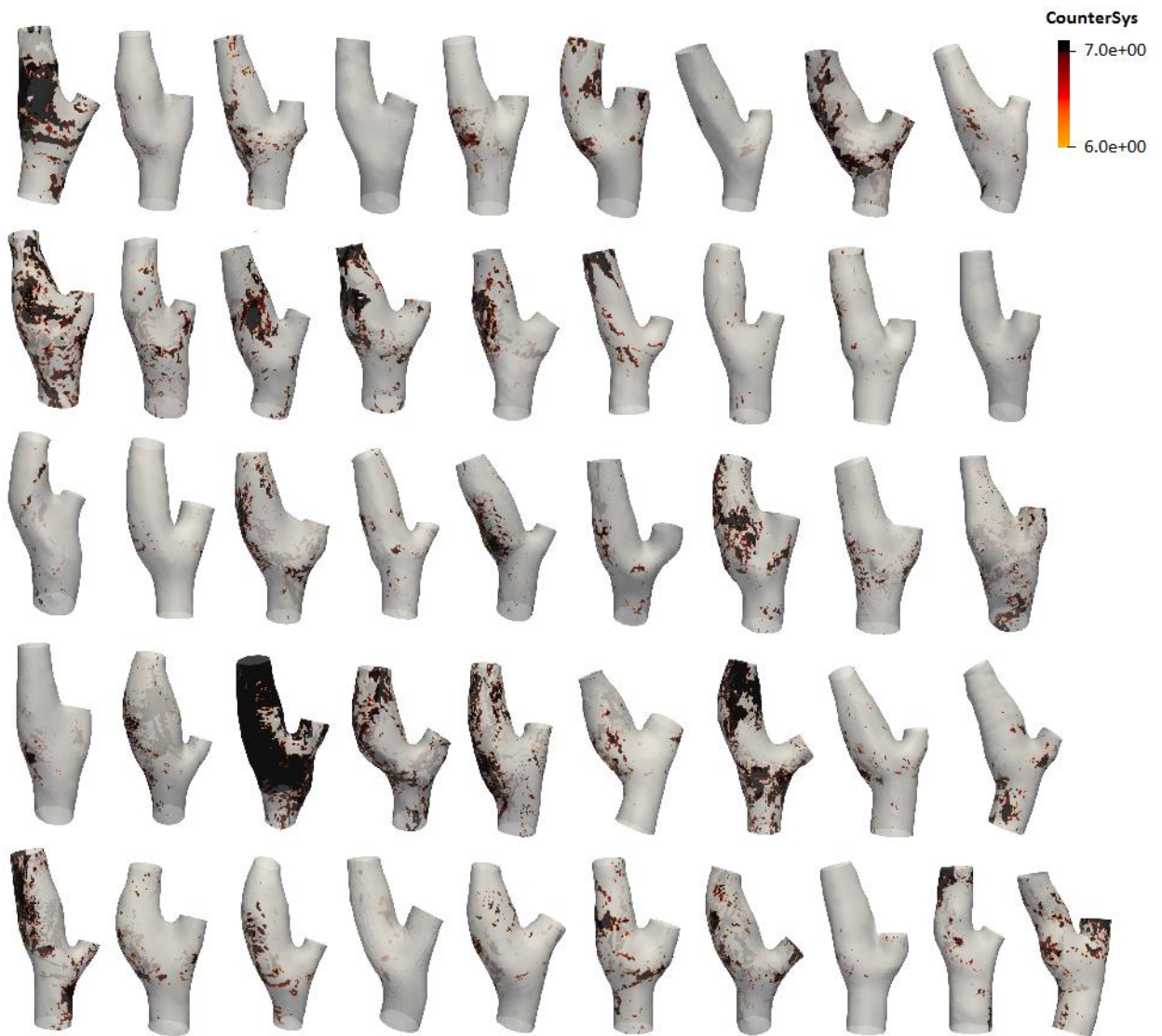


Figure 43. Exposure to high CounterSys values for the 46 carotid bifurcation models. The values reported in the legend correspond to 90th and 80th percentile values.

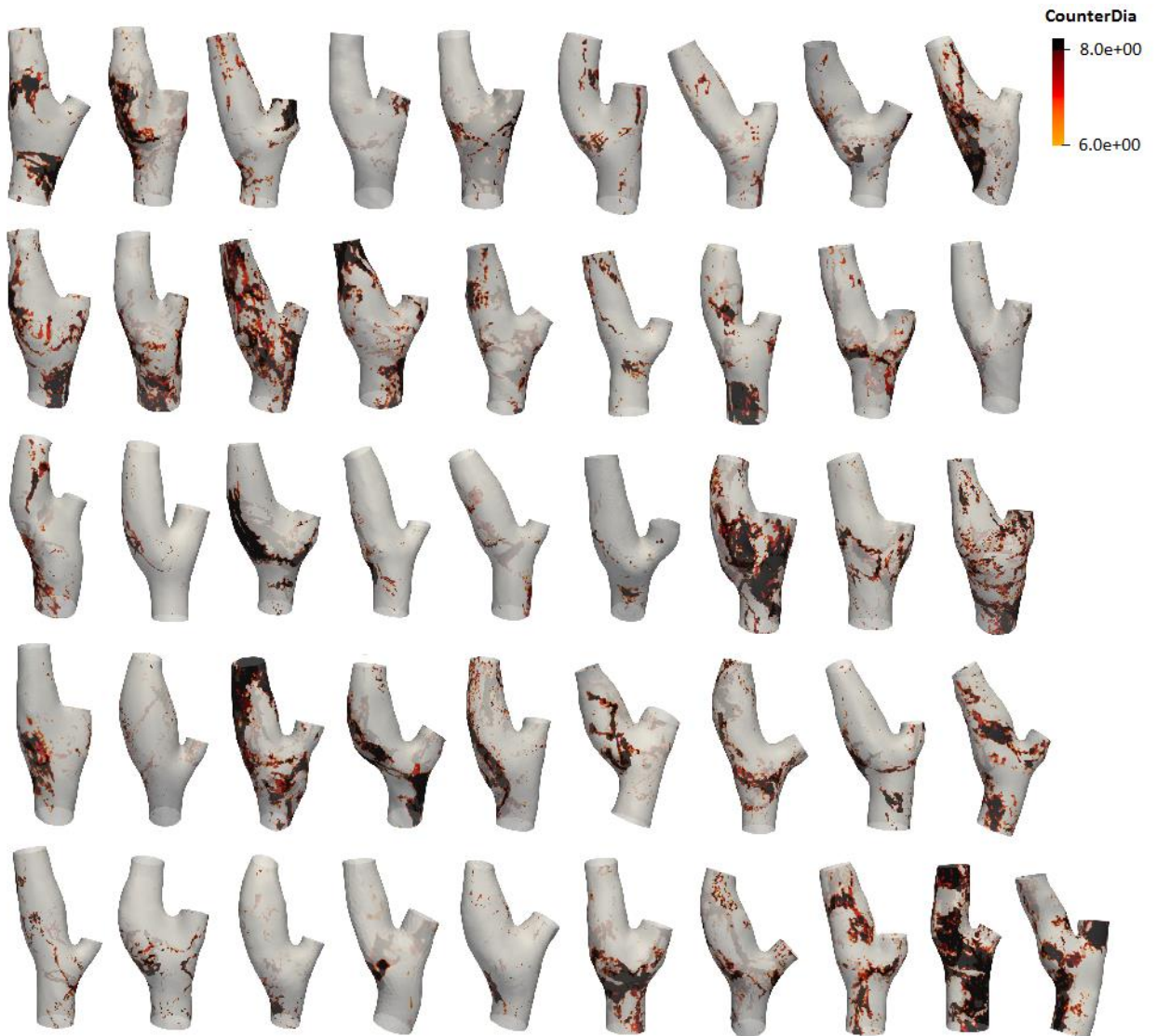


Figure 44. Exposure to high CounterDia values for the 46 carotid bifurcation models. The values reported in the legend correspond to 90th and 80th percentile values.

SAs exposed to high CounterSys values and SAs exposed to high CounterDia values do not co-localize, as illustrated by the SI distribution shown in Figure 45. So, the regions on the luminal surface that are affected by a shear stress that alternates between compressive and tensile vary depending on the cardiac phase. Considered the merged surfaces of all the forty-six cut models, CounterSys takes a median value of 3, whereas the median value of CounterDia is 2. Being the diastolic phase duration twice as much the systole duration, the latter is characterized by a greater number of sign changes of *divWSS*.

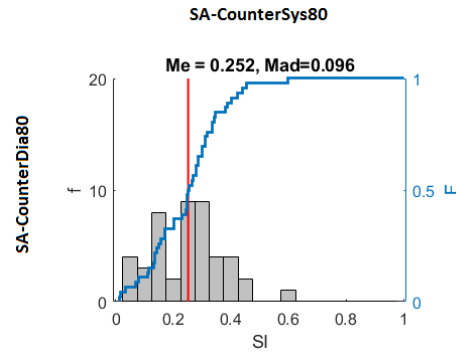


Figure 45. Distribution of SI values for the SA exposed to high CounterSys values with the SA exposed to high CounterDia values. Each bar of the histogram represents the number of cases with a certain range of SI, the blue line represents the cumulative distribution function. Me is the median, Mad is the median absolute deviation

The results of co-localization analysis of high CounterSys and high CounterDia with the considered established HWPs are shown in Figure 46 and 47, respectively.

The co-localization trends are comparable to the Counter co-localization with the pre-existing HWPs, albeit for CounterSys the median values of SI distributions are smaller than median values for Counter, whereas the median values for CounterDia are greater than those that refer to Counter. The most significant co-localization was observed between CounterDia and OSI. So, the number of sign changes of *divWSS* that occur during systole resulted to be more numerous, but less co-localized to the established HWPs than the number of sign changes counted during the diastolic phase.

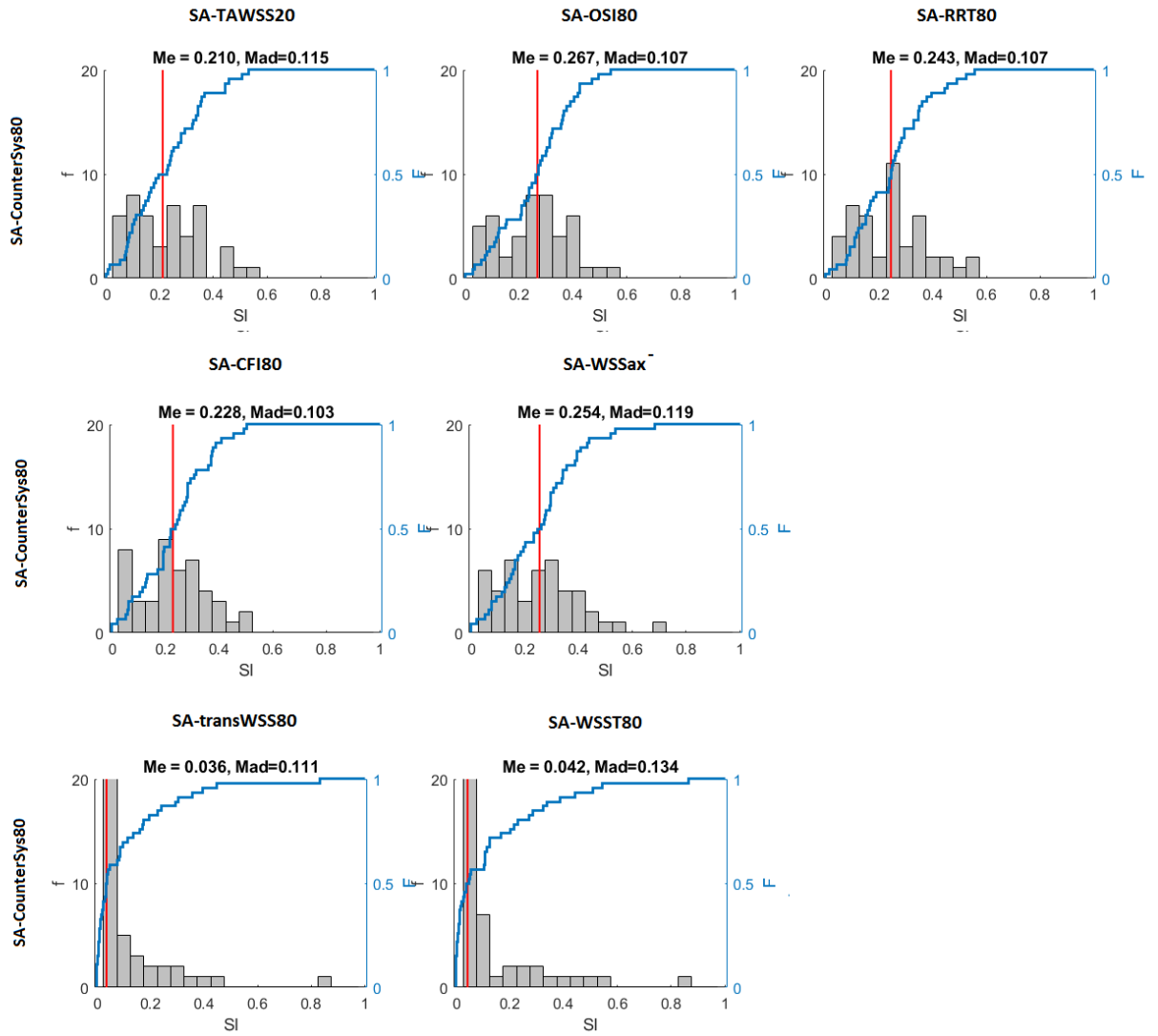


Figure 46. Distribution of SI values for the SA exposed to high CounterSys values with the SA exposed to disturbed flow, as defined by the existing HWPs. Each bar of the histogram represents the number of cases with a certain range of SI, the blue line represents the cumulative distribution function. Me is the median, Mad is the median absolute deviation.

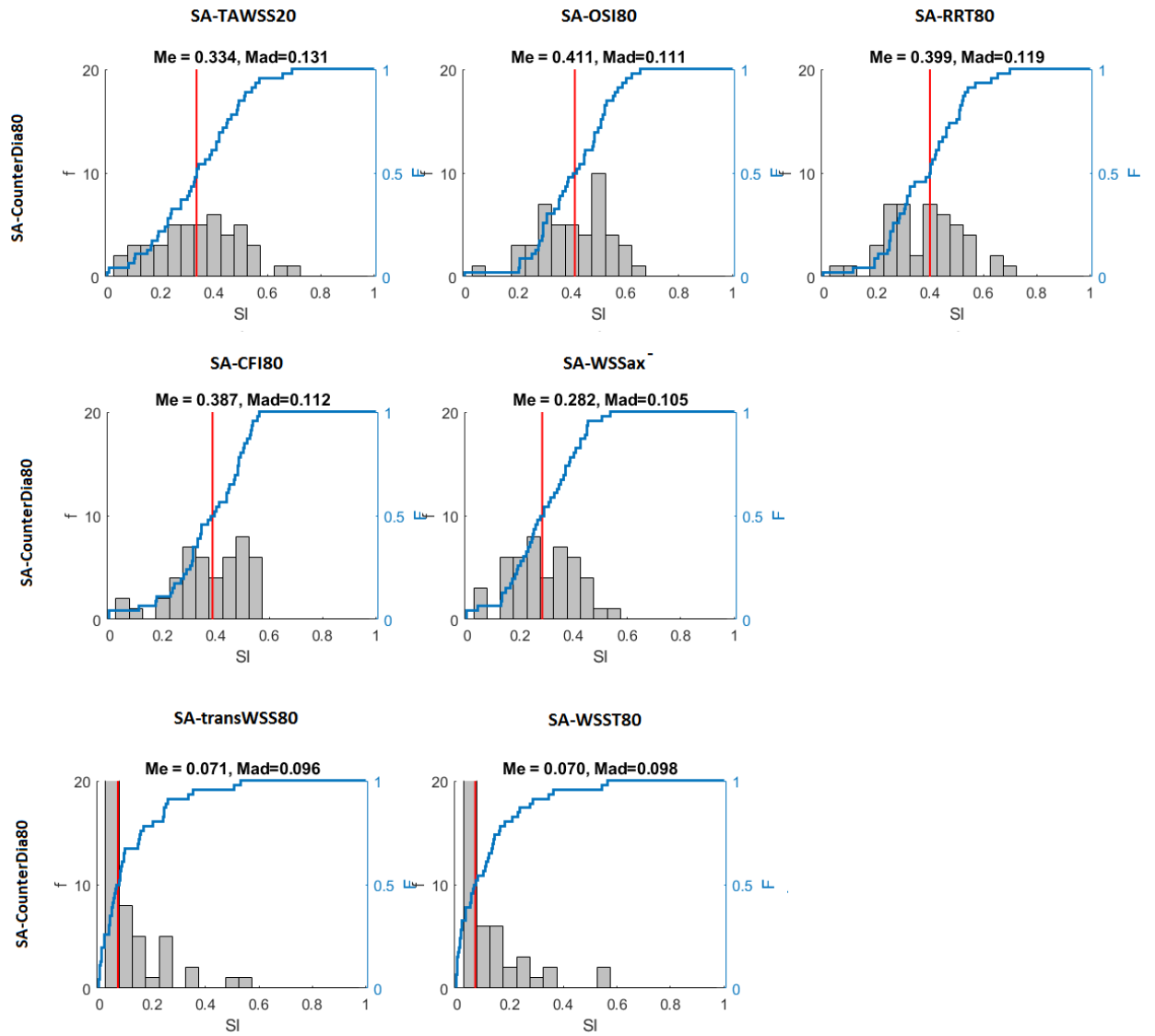


Figure 47. Distribution of SI values for the SA exposed to high CounterDia values with the SA exposed to disturbed flow, as defined by the existing HWPs. Each bar of the histogram represents the number of cases with a certain range of SI, the blue line represents the cumulative distribution function. Me is the median, Mad is the median absolute deviation.

## Chapter 6. Conclusions

Several hemodynamic wall parameters have been introduced to describe the role of disturbed blood flow in the initiation and progression of atherosclerosis in medium and large-sized arteries. The consensus theory recognizes low and oscillatory wall shear stress as localizing factors of vascular diseases. Recently, this prevailing theory has been questioned and conflicting findings encouraged the investigation of different aspects that correlates WSS features with disease. So, WSS temporal multidirectionality has recently been proposed as a pro-atherogenic factor.

Aim of this thesis was to introduce new hemodynamic wall parameters (HWPs) that can distinguish among tensile, compressive and uniform shear stresses acting on the endothelial cells. The direction of WSS could influence the morphology and the biology of endothelial cells, increasing the permeability to atherogenic particles under the endothelium and altering the balance between pro- and anti-atherosclerotic signals. However, none of the existing HWPs can capture the spatial directionality of WSS.

The haemodynamic wall parameters proposed in this work are based on the divergence of the normalized wall shear stress:

- Negative WSS Divergence (DivN);
- Positive WSS Divergence (DivP);
- Oscillatory WSS Divergence Index (ODI).

The divergence measures the tendency of the WSS field to converge toward or diverge from a point. More in detail, if the WSS vector field takes a sink arrangement, then the divergence of WSS is negative, whereas if the WSS takes a source configuration, its divergence assumes a positive value. So, DivN was defined as the temporal average of the divergence of normalized WSS in correspondence of the nodes of the surface mesh where it takes negative values, analogously DivP was defined as the temporal average of WSS divergence in the nodes where it takes positive values, and ODI was computed as the standard deviation of WSS divergence values taken throughout the cardiac cycle at each spatial position in the domain. DivN points out regions on the luminal surface that experience a sink-arranged WSS on average during the cardiac cycle, with a compressing effect on the endothelium. On the other hand, DivP identifies vessel wall regions exposed to a source-shaped WSS field, that results in a stretching of the vascular surface. ODI can capture the oscillatory behaviour of the shear stress applied on the endothelial layer, highlighting vessel wall regions exposed to large variations in WSS direction.

The divergence-based hemodynamic wall parameters were computed on the luminal surfaces of forty-six models of right carotid bifurcations acquired from

seemingly healthy people. A co-localization analysis of the novel descriptors with seven established HWPs was carried out in two steps. Initially, a visual examination of the surface areas on the carotid bifurcation regions exposed to wall descriptors above or below their respective threshold values was performed. Then, the spatial overlapping of the surface areas characterized by low DivN, high DivP and high ODI values individually with surface areas exposed to low TAWSS and  $WSS_{ax}$ , high OSI, RRT, CFI, transWSS and WSST was quantified through the evaluation of similarity indices. Low DivN showed to be moderately co-localized with low TAWSS, high RRT and high OSI, indicating that DivN can highlight bifurcation regions characterized by blood stagnation, high near-wall residence time of blood-borne particles, and converging uniaxial WSS, respectively. Low DivN regions, that are exposed to a compressive shear stress over the cardiac cycle, recognized as flow separation regions, were mainly concentrated around the bifurcation expansion. On the other hand, high DivP, that indicates flow impingement regions, typically concentrated at the bifurcation apex and moderately co-localized with high transWSS, pointing out multidirectional source-arranged WSS. ODI spatially overlapped to high OSI to a greater extent as compared to DivN, indicating its capability to highlight regions exposed to large oscillations of uniaxial WSS between the source and sink configurations. Moreover, high ODI moderately co-localized with high CFI, indicating flow reversal regions, with high RRT, highlighting high residence times near the vessel wall, and with low TAWSS, pointing out recirculation zones.

A counter was then introduced to verify the correlation of ODI with the number of consecutive sign changes of *divWSS* over the cardiac cycle. This counter did not co-localize with ODI, neither with the established HWPs, presumably because it does not consider the modulus of the divergence, so it counts even the small fluctuations of *divWSS* value around the zero value, that correspond to low deviations from the uniformity of WSS direction. Two distinct counters, corresponding to the systole and to the diastole respectively, were then defined to count the numbers of sign changes of *divWSS* during each cardiac phase. The number of sign changes of *divWSS* that occur during systole were more numerous, but less co-localized to the established HWPs than the number of sign changes counted during the diastolic phase.

The novel divergence-based descriptors are able to identify converging and diverging WSS vector fields. So, the advantage of DivP and DivN, as compared to OSI, is the capability to distinguish between tensile and compressive force applied on the endothelial layer. In addition, conversely to what transWSS can do, ODI can distinguish between reversing uniaxial flow and purely unidirectional flow.

In this work, in order to take into account the directionality of WSS only, neglecting the magnitude of WSS vectors, it was considered the divergence of the normalized WSS. Endothelial cells however respond to both magnitude and directional changes of WSS. So, to properly describe the impact of flow conditions on the biological response of endothelial cells, the divergence-based descriptors that

were introduced here can be better used in association with other hemodynamic parameters that evaluate WSS magnitude, as TAWSS, RRT or WSSG.

Moreover, there is a limitation in the use of ODI. This index actually correlates with sign changes of WSS divergence, and consequently to large oscillations between the source and sink stress configurations if the distribution of *divWSS* values taken during the cardiac cycle is roughly symmetrically-distributed around a mean value close to zero.

To assess the validity of the proposed divergence-based descriptors in atherosclerosis prediction, the potential correlation between the directional changes of WSS that the divergence-based HWPs can identify and the lesion appearance needs to be checked.

## Appendix

### A) Generation of the centerline and cut of bifurcation regions in VMTK software

```
vmtksurfacereader -ifile C:/wss0040.tec --pipe vmtkcenterlines --pipe
vmtkbranchextractor --pipe vmtkbranchclipper --pipe vmtkbifurcationsections -id
3 -i @vmtkbranchclipper.o -distancespheres 3 -sectionpointgroupid 0 -
sectionpointbifurcationgroupid 1 --pipe vmtkbifurcationsections -id 5 -i
@vmtkbranchclipper.o -distancespheres 5 -sectionpointgroupid 2 -
sectionpointbifurcationgroupid 1 --pipe vmtkbifurcationsections -id 2 -i
@vmtkbranchclipper.o -distancespheres 2 -sectionpointgroupid 3 -
sectionpointbifurcationgroupid 1 --pipe vmtkpointsplitextractor -i
@vmtkcenterlines.o -splitpoint @vmtkbifurcationsections-3.sectionpoint -
tolerance 1E-3 -gaplength 0.2 --pipe vmtkbranchclipper -i @vmtksurfacereader.o
-groupids 0 -insideout 1 --pipe vmtkpointsplitextractor -i @vmtkcenterlines.o -
splitpoint @vmtkbifurcationsections-5.sectionpoint -tolerance 1E-3 -gaplength
0.2 --pipe vmtkbranchclipper -groupids 0 --pipe vmtkpointsplitextractor -i
@vmtkcenterlines.o -splitpoint @vmtkbifurcationsections-2.sectionpoint -
tolerance 1E-3 -gaplength 0.2 --pipe vmtkbranchclipper -groupids 0 --pipe
vmtksurfacewriter -ofile C:/wss_cut.tec
```

### B) Projection of the HWPs onto the bifurcation regions in VMTK software

```
vmtksurfaceprojection -ifile C:/wss_cut.tec -rfile C:/RRT.tec -ofile C:/RRT_cut.tec
--pipe vmtksurfaceprojection -ifile C:/wss_cut.tec -rfile C:/tawss.tec -ofile
C:/tawss_cut.tec --pipe vmtksurfaceprojection -ifile C:/wss_cut.tec -rfile
C:/osi.tec -ofile C:/osi_cut.tec --pipe vmtksurfaceprojection -ifile C:/wss_cut.tec -
rfile C:/CFI_transWSS_WSSa.tec -ofile C:/CFI_transWSS_WSSa_cut.tec --pipe
vmtksurfaceprojection -ifile C:/wss_cut.tec -rfile C:/WSST.tec -ofile
C:/WSST_cut.tec --pipe vmtksurfaceprojection -ifile C:/wss_cut.tec -rfile
C:/meandivnorm.tec -ofile C:/meandivnorm_cut.tec
```

### C) Sensitivity Analysis

- VMTK

Exporting a .stl surface:

```
Vmtksurfacereader -ifile C:/wss040.tec --pipe vmtksurfacewriter -ofile C:/mesh.stl
```

▪ ANSYS ICEM CFD

Creating four million elements mesh:

File -> Import Geometry -> Faceted -> STL -> mesh.stl -> Apri -> Generate -> Done

Geometry -> Create/modify curve  -> Extract Curves from surfaces 

- Surface type: Faceted
- Angle for surfaces: 90
- Min number of segments: 1
- Which curve segments: Both

Select surfaces  -> Select -> Apply -> Ok

Geometry -> Create/modify Curve  -> Segment curve 

- Method: Segment by connectivity

Select curve  -> Select -> Apply -> Ok

Create/modify surface  -> Simple surface 

- Method: From curves

Select curve  -> Select curves one at a time -> Apply -> Ok

Parts -> Create part

Part: InletCCA -> Select entities ->  Select the inlet surface -> Apply -> Ok

Parts -> Create part

Part: OUTletECA -> Select entities  -> Select the outlet surface corresponding to ECA -> Apply -> Ok

Parts -> Create part

Part: OUTletICA -> Select entities  -> Select the outlet surface corresponding to ICA -> Apply -> Ok

Parts -> Mesh -> Rename -> Wall -> Done

Mesh -> Global mesh setup 

Global Mesh Size

Global Element Scale Factor

- Scale factor: 1.1e-5

Global Element Seed Size

- Max element: 2048

*Curvature/proximity based refinement*

- *Enabled*
- *Min size limit: 200*
- *Elements in gap: 1*
- *Refinement: 18*

*Apply -> Ok*

*Mesh -> Compute mesh* 

*Volume Mesh*

- *Mesh Type: Tetra/Mixed*

*Tetra/Mixed Mesh*

- *Mesh Method: Robust (Octree)*

*-> Compute*

*Output -> Select solver*  *->*

- *Output solver: ANSYS Fluent*
- *Common Structural Solver: ANSYS*

*-> Apply*

*Output -> Boundary conditions*  *-> Accept*

*Output -> Write input* 

- *Grid dimension: 3D*
- *Scaling: No*
- *Output file: "mesh4m" -> Done*

To create eight million elements mesh the *Global element scale factor* has been changed to  $8.7e-6$  and the *Output file name* to "*mesh8m*".

#### ▪ ANSYS FLUENT

- *Dimension: 3D*
- *Options: Double precision*
- *Processing Options: Serial -> Ok*

*File -> Read -> Mesh -> Select "mesh4m.msh" (or "mesh8m.msh") file -> Ok*

*Display -> Mesh*

*Options: Edges*

*Edge Type: All*

*Surfaces:*

- *inletCCA*
- *outletECA*
- *outletICA*
- *wall*

*-> Display -> Close*

*Solution Setup*

- *General*

*Mesh -> Scale ->*

- *View length unit in: m*
- *Scaling*

*Specify scaling factor*

*Scaling Factors:*

*X =0.01*

*Y =0.01*

*Z =0.01*

*-> Scale -> Close*

*Mesh -> Check*

*Solver*

- *Type: Pressure-based*
- *Velocity Formulation: Absolute*
- *Time: Steady*

- *Models -> Viscous-Laminar*

- *Materials -> Fluid -> Create/edit*

- *Name: Blood*
- *Density: constant*  
*1060 kg/m<sup>3</sup>*
- *Viscosity: constant*  
*0.0035 kg/m\*s*

*Change/create -> Close*

- *Cell zone Conditions -> Type: Fluid -> Edit -> Zone Name: Blood -> Ok*

- *Boundary condition*

- *InletCCA*  
*Type: velocity-inlet*

-> Edit

*Momentum*

*Velocity Specification Method: Magnitude, Normal to Boundary*

*Reference Frame: Absolute*

*Velocity magnitude: 0.26 m/s*

-> Ok

- *Int\_Fluid*

*Type: Interior*

- *OutletECA*

*Type: pressure Outlet*

*Momentum*

*Gauge Pressure: 0 Pa*

*Backflow Direction Specification Method: Normal to Boundary*

-> Ok

- *OutletICA*

*Type: pressure Outlet*

*Momentum*

*Gauge Pressure: 0 Pa*

*Backflow Direction Specification Method: Normal to Boundary*

-> Ok

- *Wall*

*Type: Wall*

## *Solution*

- *Solution Methods*

*Pressure-Velocity Coupling*

*Scheme: SIMPLE*

*Spatial Discretization*

*Gradient: Least Squares Cell Based*

*Pressure: Second Order*

*Momentum: Second Order Upwind*

- *Monitors*

*Residuals, Statistic and Force Monitors*

*Residuals-Print, Plot -> Edit*

*Residual*

- *continuity: 0.0001*
- *x-velocity: 0.0001*
- *y-velocity: 0.0001*
- *z-velocity: 0.0001*

*Convergence Criterion: absolute*

*-> Ok*

- *Solution Initialization*  
*Initialization Methods: Standard Initialization*  
*Reference Frame: Relative to Cell Zone*  
*Initial Values:*  
*Gauge Pressure: 0 Pa*  
*X Velocity: 0 m/s*  
*Y Velocity: 0 m/s*  
*Z Velocity: 0 m/s*  
*-> Initialize*
- *Run Calculation -> Check case*  
*Number of iterations: 3000*  
*-> Calculate*

## References

- **Arzani A. and Shadden S. C.** Characterizations and Correlations of Wall Shear Stress in Aneurysmal Flow. *Journal of Biomechanical Engineering*, 2016.
- **Arzani A., Gambaruto A. M., Chen G., Shadden S. C.** Wall shear stress exposure time: a Lagrangian measure of near-wall stagnation and concentration in cardiovascular flow. *Biomech Model Mechanobiol*, 2017.
- **Augst A. D., Ariff B., Thom S. A. G. McG., Xu X. Y., Hughes A. D.,** Analysis of complex flow and the relationship between blood pressure, wall shear stress, and intima-media thickness in the human carotid artery. *Am J Physiol Heart Circ Physiol*, 2007.
- **Caruso M. V., Serra R., Perri P., Buffone G., Calì F. G., De Franciscis S., Fragomeni F.,** A computational evaluation of sedentary lifestyle effects on carotid hemodynamics and atherosclerotic events incidence. *Acta Bioeng Biomech.*, 2017.
- **Chatzizisis Y. S., Coskun A. U., Jonas M., Edelman E.R., Feldman C. L., Stone P. H.,** Role of Endothelial Shear Stress in the natural history of coronary atherosclerosis and vascular remodeling. *Journal of American College of Cardiology*, 2007.
- **Chien S.,** Effects of Disturbed Flow on Endothelial Cells. *Ann Biomed Eng.* 2008.
- **De Goes F., Desbrun M., Tong Y.,** Vector field processing on triangle meshes. *ACM SIGGRAPH Asia*, 2015.
- **Dolan J. M., Kolega J., Meng H.,** High Wall Shear Stress and Spatial Gradients in Vascular Pathology: A Review. *Ann Biomed Eng.*, 2013.
- **Friedman M. H., Bargeron C. B., Deters O. J., Hutchins G. M., Mark F. F.,** Correlation between wall shear and intimal thickness at a coronary artery branch. *Atherosclerosis*, 1987.
- **Gallo D., Isu G., Massai D., Pennella F., Deriu M. A., Ponzini R., Bignardi C., Audenino A. Rizzo G., Morbiducci U.,** A survey of quantitative descriptors of arterial flows. *Biomedical Engineering*, 2014.
- **Gallo D., Steinman D. A., Morbiducci U.,** An insight into the mechanistic role of the common carotid artery on the hemodynamics at the carotid bifurcation. *Annals of Biomedical Engineering*, 2015.
- **Gallo D., Steinman D. A., Morbiducci U.,** Insights into the co-localization of magnitude-based versus direction-based indicators of disturbed shear at the carotid bifurcation. *Journal of Biomechanics*, 2016.
- **Gelfand B. D., Epstein F. H., Blackman B. R.,** Spatial and Spectral Heterogeneity of Time-Varying Shear Stress Profiles in the Carotid Bifurcation by Phase-Contrast MRI. *Journal of magnetic resonance imaging*, 2006.
- **Giddens D. P., Zarins C. K., Glagov S.,** The Role of Fluid Mechanics in the Localization and Detection of Atherosclerosis. *J Biomech Eng*, 1993.
- **Glagov S., Zarins C., Giddens D. P., Ku D. N.,** Hemodynamics and Atherosclerosis. Insights and Perspectives gained from studies of human arteries. *Arch Pathol Lab Med*, 1988.

- **Himburg H. A. and Friedman M. H.**, Correspondence of Low Mean Shear and High Harmonic Content in the Porcine Iliac Arteries. *J. Biomech Eng*, 2006.
- **Hoi Y., Wasserman B. A., Lakatta E. G., Steinman D. A.**, Effect of common carotid artery inlet length on normal carotid bifurcation hemodynamics. *Journal of biomechanical engineering*, 2010.
- **Hoi Y., Zhou Y. Q., Zhang X., Henkelman R. M., Steinman D. A.**, Correlation between local hemodynamics and lesion distribution in a novel aortic regurgitation murine model of atherosclerosis. *Annals of Biomedical Engineering*, 2011.
- **Hyun S., Kleinstreuer C., Archie J. P.**, Computational analysis of effects of external carotid artery flow and occlusion on adverse carotid bifurcation hemodynamics. *The Journal of Vascular Surgery*, 2002.
- **Ku D. N., Giddens D. P., Zarins C. K., Glagov S.**, Pulsatile Flow and Atherosclerosis in the Human Carotid Bifurcation. *Arteriosclerosis*, 1985.
- **Lee S. W., Antiga L., Steinman D. A.**, Correlations among indicators of disturbed flow at the normal carotid bifurcation. *J Biomech Eng*, 2009.
- **Malek A. M., Alper S. L., Izumo S.**, Hemodynamic shear stress and its role in atherosclerosis. *JAMA*, 1999.
- **Marshall I., Papathanasopoulou P., Wartolowska K.**, Carotid flow rates and flow division at the bifurcation in healthy volunteers. *Physiol. Meas.*, 2004.
- **Mohamied Y., Rowland E. M., Bailey E. L., Sherwin S. J., Schwartz M. A., Weinberg P. D.**, Change of direction in the biomechanics of atherosclerosis. *Annals of Biomedical Engineering*, 2015.
- **Mohamied Y., Sherwin S. J., Weinberg P. D.**, Understanding the fluid mechanics behind transverse wall shear stress. *Journal of Biomechanics*, 2017.
- **Moore J. E. Jr, Xu C., Glagov S., Zarins C. K., Ku D. N.**, Fluid wall shear stress measurements in a model of the human abdominal aorta: oscillatory behavior and relationship to atherosclerosis. *Atherosclerosis*, 1994.
- **Morbiducci U., Gallo D., Cristofanelli S., Ponzini R., Deeri M. A., Rizzo G., Steinman D. A.**, A rational approach to defining principal axes of multidirectional wall shear stress in realistic vascular geometries, with application to the study of the influence of helical flow on wall shear stress directionality in aorta. *Journal of Biomechanics*, 2015.
- **Papaioannou T. G., Stefanadis C.**, Vascular Wall Shear Stress: Basic Principles and Methods. *Hellenic J Cardiol*, 2005.
- **Peiffer V., Sherwin S. J., Weinberg P. D.**, Does low and oscillatory wall shear stress correlate spatially with early atherosclerosis? A systematic review. *Cardiovascular Research*, 2013a.
- **Peiffer V., Sherwin S.J., Weinberg P.D.**, Computation in the rabbit aorta of a new metric – the transverse wall shear stress – to quantify the multidirectional character of disturbed blood flow. *Journal of Biomechanics*, 2013b.
- **Pinto S. I. S., Campos J. B. L. M.**, Numerical study of wall shear stress-based descriptors in the human left coronary artery. *Computer Methods in Biomechanics and Biomedical Engineering*, 2016.

- **Saenz C.**, Discrete differential geometry. CS 468 (Spring 2013) Lecture 14, 2013.
- **Secomb T. W.**, Hemodynamics. *Compr Physiol.*, 2017.
- **Shaaban A. M., Duerinckx A.**, Wall Shear Stress and early atherosclerosis: a review. *AJR*, 2000.
- **Sousa L. C., Castro C. F., António C. C., Santos A. M. F., dos Santos R. M., Castro P. M. A. C., Azevedo E., Tavares J. M. R. S.** Toward hemodynamic diagnosis of carotid artery stenosis based on ultrasound image data and computational modeling. *Med Biol Eng Comput*, 2014.
- **Van Wyk S., Wittberg L. P., Fuchs L.** Atherosclerotic indicators for blood-like fluids in 90-degree arterial-like bifurcations. *Computers in Biology and Medicine*, 2014.
- **Wasilewski J., Mirotka K., Kiljanski T.**, Biomechanical aspects of atherosclerosis. 2013.
- **White C. R., Haidekker M., Bao X., Frangos J. A.** Temporal Gradients in Shear, but not Spatial Gradients, stimulate Endothelial Cell Proliferation. *Circulation*, 2001.
- **Zarins C. K., Giddens D. P., Bharadvaj B. K., Sottiurai V. S., Mabon R. F., Glagov S.**, Carotid bifurcation atherosclerosis. Quantitative correlation of plaque localization with flow velocity profiles and wall shear stress. *Circ Res.*, 1983.
- **Zhang Y., Takao H., Murayama Y., Qian Y.** Propose a wall shear stress divergence to estimate the risks of intracranial aneurysm rupture. *The scientific world journal*, 2013.

[1] <https://www.britannica.com/science/arteriosclerosis>

[2] <https://courses.lumenlearning.com/ap2/chapter/structure-and-function-of-blood-vessels/>

[3] <http://www.heart.org>

[4] <http://www.strokeassociation.org>

[5] <https://www.khanacademy.org/math/multivariable-calculus/multivariable-derivatives/divergence-and-curl-articles/a/divergence>

[6] [https://mathinsight.org/divergence\\_idea](https://mathinsight.org/divergence_idea)

[7] <https://en.wikipedia.org/wiki/Divergence>

[8] [https://en.wikipedia.org/wiki/Common\\_carotid\\_artery](https://en.wikipedia.org/wiki/Common_carotid_artery)

[9] <https://www.webmd.com/heart/picture-of-the-carotid-artery#1>

[10] <https://courses.lumenlearning.com/suny-ap2/chapter/cardiac-cycle/>

## Figure references

- *Figure 1.* <https://humananatomyclass.co/which-body-part-belongs-to-the-circulatory-system/>
- *Figure 2.* <http://biology4alevel.blogspot.it/2014/11/43-circulatory-system-blood-vessels.html>

- Figure 3.  
<https://www.memorangapp.com/flashcards/158397/%5BAnatomy%5D+Fundamentals+of+Medicine/>
- Figure 4. <https://healthjade.com/ischemic-heart-disease/>
- Figure 5. <https://healthiack.com/encyclopedia/pictures-of-carotid-arteries>
- Figure 6.  
[https://stuff.mit.edu/afs/athena/course/10/10.301/www2002/movies\\_for\\_assignment\\_1.html](https://stuff.mit.edu/afs/athena/course/10/10.301/www2002/movies_for_assignment_1.html)
- Figures 8, 9, 10, 11, 14. Secomb T. W. Hemodynamics. *Compr Physol*. 2017
- Figure 12. <http://cultua.info/carotid-artery/>
- Figure 13. <http://www.ctialatest.org/carotid/carotid-bulb-anatomy>
- Figure 15. Glagov S., Zarins C., Giddens D. P., Ku D. N., Hemodynamics and Atherosclerosis. Insights and Perspectives gained from studies of human arteries. *Arch Pathol Lab Med*, 1988.
- Figure 16. <https://www.quora.com/What-is-curl-and-divergence-of-a-vector-field>